POLITECNICO
MILANO 1863

SCUOLA DI INGEGNERIA INDUSTRIALE
E DELL'INFORMAZIONE

Thermo-mechanical properties and microstructural evolution of thin films for nuclear applications

Tesi di Laurea Magistrale in
Nuclear Engineering - Ingegneria Nucleare

Author: **Luca Castronuovo**

Student ID: 953506
Advisor: Prof. Marco Beghi
Academic Year: 2022-23

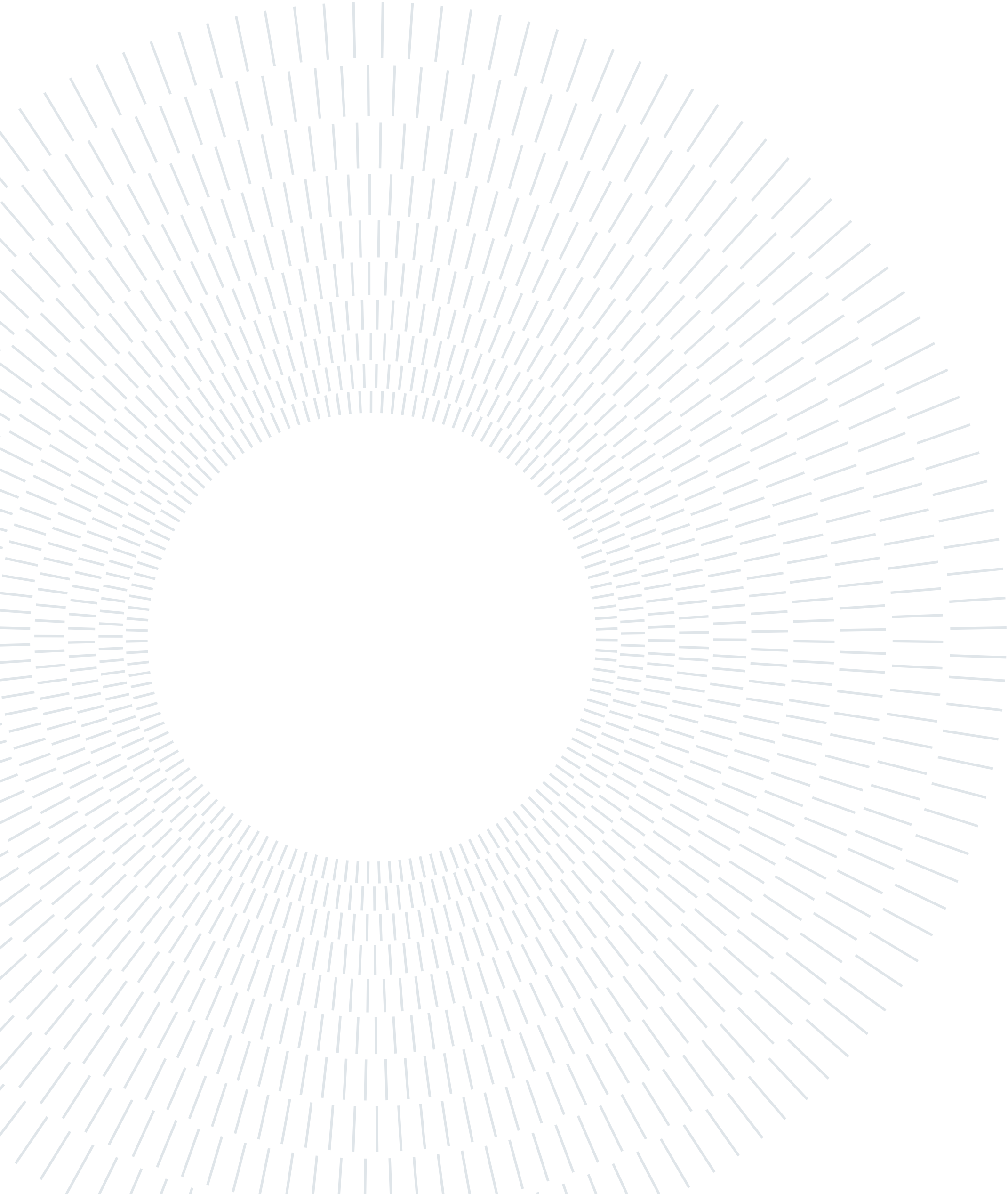

Abstract

In recent decades, thin films have assumed a crucial role in a wide range of applications, from energy to construction and metallurgy. Their versatility and ability to improve substrate properties without altering their thickness make them instrumental in multiple contexts.

Thermo-mechanical characterization of thin films is of particular importance when they are used in extremely aggressive environments, such as nuclear reactor cores. Phenomena such as embrittlement due to irradiation or corrosion caused by contact with liquid metals can make it impractical to use conventional materials in reactor components. One possible solution is the use of thin films as coatings to improve their durability.

The goal is to understand which materials are most resilient to these conditions and, at the same time, to analyze the transformations undergone by film and substrate. We are interested in the response to stresses, changes in microstructure, and adhesion. Thermal stresses caused by the different thermal expansion of film and substrate, as well as crystallization resulting from extreme events or prolonged use, can lead to failure of films, render them unusable or, on the contrary, improve their characteristics. To address this challenge, we chose to use Brillouin spectroscopy, which relies on acoustic wave analysis of films to determine their elastic properties. In addition, we employed the substrate curvature technique, which allows us to evaluate the stresses in the film and its coefficient of thermal expansion. The adoption of such techniques becomes necessary because traditional methodologies for characterizing *bulk* materials cannot be applied. The values of the thermal expansion and stiffness coefficients of the films often differ from those of the bulk material, either because of the presence of a substrate, which greatly changes the characteristics of the material of interest, or because of the small size of the crystalline grains. Samples of tungsten (W), aluminum (Al) and tungsten nitride, both in crystalline and nanocrystalline or amorphous forms, were examined, with a particular interest in their suitability in fusion reactors or fourth-generation fission reactors, the subject of current studies. A trend of increasing stiffness of the films as the crystallinity of the specimens increased was found to be in agreement with reports in the scientific literature. To evaluate the coefficient of thermal expansion (CTE), the samples were heated and the curvature was measured by deflection of laser beams. CTE values for nanocrystalline films deposited by the HiPIMS technique are found to be similar to those of bulk material due to their extreme compactness and high residual stresses that tend to minimize the average interatomic distance. In contrast, amorphous films deposited with the PLD technique exhibit higher CTE values, attributable to the high percentage of void in them. Through the substrate bending technique, phenomena such as plastic creep, densification and formation of "hillocks" were observed. These were further confirmed by scanning electron microscope (SEM) analysis. The microstructural instability found in these samples may be a limitation for practical use in certain applications.

Abstract in lingua italiana

Negli ultimi decenni, i film sottili hanno assunto un ruolo cruciale in un vasto spettro di applicazioni, dall'ambito energetico a quello edilizio e metallurgico. La loro versatilità e la capacità di migliorare le proprietà del substrato senza alterarne lo spessore li rendono strumentali in molteplici contesti.

La caratterizzazione termo-meccanica dei film sottili è di particolare importanza quando vengono impiegati in ambienti estremamente aggressivi, come i noccioli dei reattori nucleari. Fenomeni come l'infragilimento dovuto all'irraggiamento o la corrosione provocata dal contatto con metalli liquidi possono rendere impraticabile l'uso di materiali convenzionali nelle componenti dei reattori. Una soluzione possibile è l'utilizzo di film sottili come rivestimento per migliorare la loro durabilità.

L'obiettivo è comprendere quali materiali siano più resilienti a queste condizioni e, contemporaneamente, analizzare le trasformazioni subite da film e substrato. Ci si interessa alla risposta agli sforzi, alle variazioni nella microstruttura e all'adesione. Sforzi termici causati dalla diversa espansione termica di film e substrato, così come la cristallizzazione derivante da eventi estremi o dall'uso prolungato, possono portare al fallimento dei film, renderli inutilizzabili o, al contrario, migliorare le loro caratteristiche.

Per affrontare questa sfida, abbiamo scelto di utilizzare la spettroscopia Brillouin, che si basa sull'analisi delle onde acustiche dei film per determinarne le proprietà elastiche. Inoltre, abbiamo impiegato la tecnica di curvatura del substrato, che consente di valutare gli sforzi nel film e il suo coefficiente di espansione termica. L'adozione di tali tecniche diventa necessaria poiché le metodologie tradizionali per la caratterizzazione dei materiali di *bulk* non possono essere applicate. I valori dei coefficienti di espansione termica e di rigidezza dei film spesso differiscono da quelli del materiale di massa, sia a causa della presenza di un substrato che modifica notevolmente le caratteristiche del materiale d'interesse, sia a causa delle ridotte dimensioni dei grani cristallini. Sono stati esaminati campioni di tungsteno (W), alluminio (Al) e nitruro di tungsteno, sia in forma cristallina che nanocristallina o amorfa, con un particolare interesse per la loro idoneità nei reattori a fusione o reattori a fissione di quarta generazione, oggetto di attuali studi.

È emerso un trend di aumento della rigidezza dei film all'aumentare della cristallinità dei campioni, in accordo con quanto riportato nella letteratura scientifica. Per valutare il coefficiente di espansione termica (CTE), i campioni sono stati riscaldati e la curvatura è stata misurata attraverso la deviazione di fasci laser. I valori di CTE per i film nanocristallini depositati con la tecnica HiPIMS risultano simili a quelli del materiale di massa, grazie alla loro estrema compattezza e agli elevati sforzi residui che tendono a minimizzare la distanza media interatomica. Al contrario, i film amorfi depositati con la tecnica PLD presentano valori più elevati di CTE, attribuibili all'alta percentuale di vuoto in essi presente. Attraverso la tecnica di curvatura del substrato, si sono osservati fenomeni come lo scorrimento plastico, la densificazione e la formazione di "hillocks". Questi sono stati ulteriormente confermati dall'analisi al microscopio elettronico a scansione (SEM). L'instabilità microstrutturale riscontrata in questi campioni può costituire un limite all'utilizzo pratico in determinate applicazioni.

Contents

Abstract **i**

Abstract in lingua italiana **iii**

Contents **v**

Introduction **1**

1 Thin Film **5**

1.1 Mechanical Behavior of a Thin Film on a Substrate 5

1.2 Microstructure and Mechanical Properties 10

1.2.1 Deposition techniques 10

1.2.2 Thin Films' Microstructure 11

1.2.3 Residual stresses 13

1.2.4 Mechanical properties 14

2 Nuclear Materials **19**

2.1 GEN IV reactors: LFR 19

2.1.1 Technological challenges in LFR structural materials 21

2.2 Fusion reactors 22

2.2.1 Tokamak reactor 22

2.2.2 Plasma Facing Materials 24

2.2.3 Candidate materials and coatings for PMCs 26

3 Thermo-mechanical Characterization of TF **29**

3.1 Introduction 29

3.2 BLS spectroscopy 30

3.2.1 Bulk and Surface Elastic Waves in a solid 31

3.2.2 Acoustic modes in a supported thin film 36

3.2.3 Light interaction with acoustic modes 37

- 3.3 Wafer Curvature Technique 41
  - 3.3.1 CTE determination 44
  - 3.3.2 Residual stresses 45

4 Methodology and Experimental Setup 47

- 4.1 Brillouin Spectroscopy Experimental Setup 47
  - 4.1.1 Laser and Optical Path 47
  - 4.1.2 Fabry-Perot interferometer 48
  - 4.1.3 Measurement Error 51
- 4.2 Stoney's experimental setup 53
  - 4.2.1 Laser and Optical Path 53
  - 4.2.2 CMOS 54
  - 4.2.3 Vacuum Chamber, Power Supply, Heater and Thermocouples 55
  - 4.2.4 Acquisition and Elaboration Software 55
  - 4.2.5 Sensitivity Analysis and Measurement Errors 56

5 Results and Discussion 61

- 5.1 System optimization and Measurement procedure 61
  - 5.1.1 Introduction 61
  - 5.1.2 Wafer Curvature Technique optimization 61
  - 5.1.3 Measurement Procedure 65
- 5.2 Samples 67
- 5.3 Experimental results 67
  - 5.3.1 Aluminum 67
  - 5.3.2 Nanocrystalline Tungsten 76
  - 5.3.3 Amorphous Tungsten 79
  - 5.3.4 Tungsten Nitride 79
  - 5.3.5 Yttrium Oxide 84

6 Conclusions and future developments 87

A Appendix A 91

- A.1 Irradiation effects 91
  - A.1.1 Candidate materials and coatings for LFR 99

A Appendix B 101

- A.1 Frame comparison and Centroids time-behaviour 101
- A.2 Residual Stresses determination 108

Bibliography **113**

List of Figures **119**

List of Tables **125**

Acknowledgements **127**

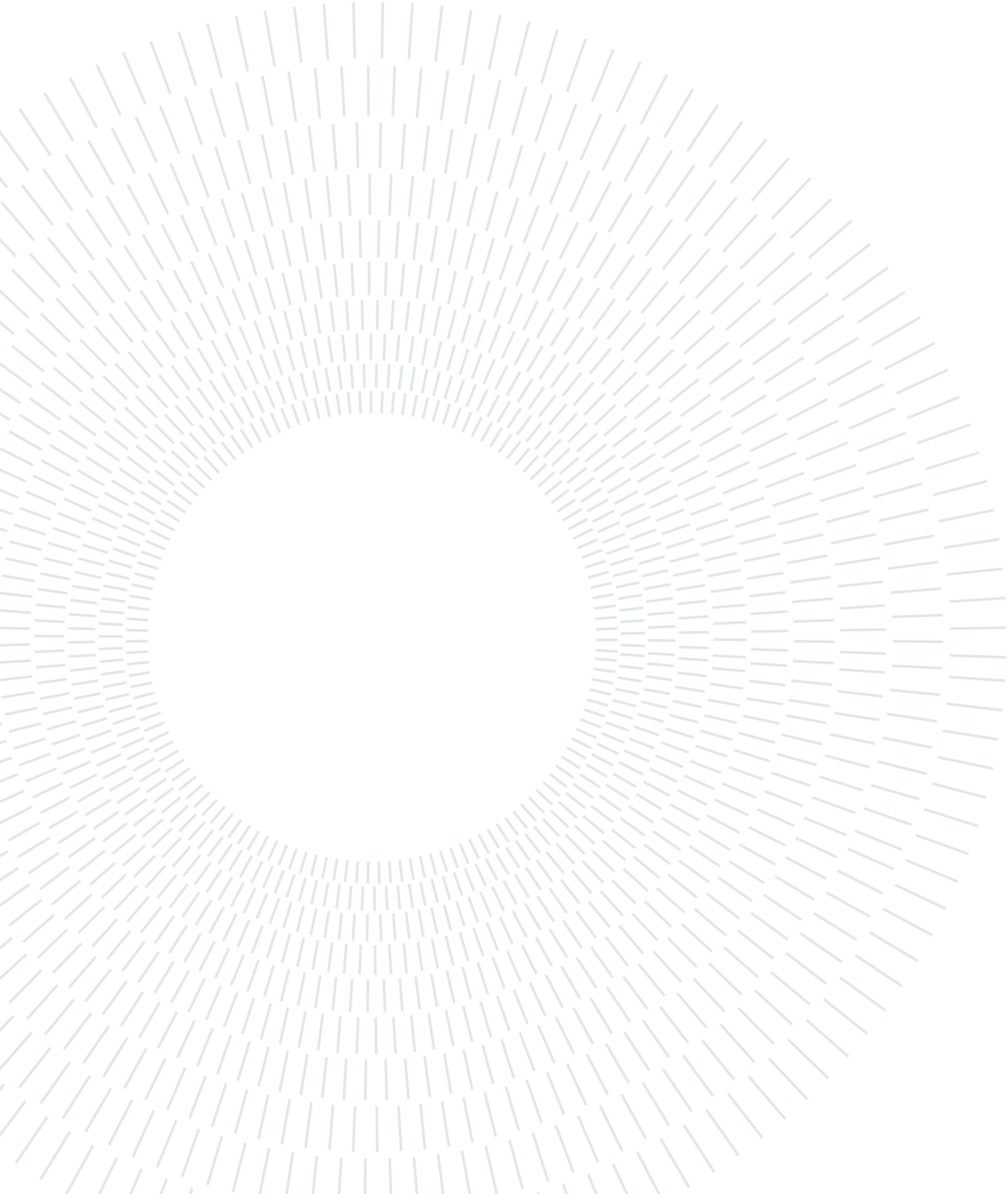

Introduction

This thesis centers on the thermomechanical characterization of thin films using Brillouin spectroscopy to determine their elastic properties and the beam deflection technique to assess the stresses that arise in the film during thermal cycles, along with its coefficient of thermal expansion. Special emphasis will be placed on thin coatings designed for nuclear applications. In this introduction, we aim to elucidate the nature of thin films, outline their typical applications, justify our focus on nuclear applications, and underscore the significance of developing precise methods for determining their properties.

To begin with, let's define what a 'thin film' is: it is a structure composed of metallic, ceramic, polymeric, or composite materials, with a thickness ranging from a single atomic layer (monolayer) to a few micrometers, and lateral dimensions several orders of magnitude larger[1]; the thicknesses of interest in our study are typically less than 1 µm. These films are commonly deposited on a bulk material substrate or are formed through reactions involving the substrate. The adhesion between the coating and substrate, defined as the work required to detach two adhering interfaces, stands out as a critical parameter influencing the durability and long-term performance of protective coatings. This adhesion can result from chemical bonds (covalent, ionic, hydrogen, van der Waals) or mechanical bonding, which is associated with substrate surface roughness and porosity.

In recent years, there has been a growing focus on the properties of thin films due to their pivotal role in a wide range of modern applications.

Given that many physical interactions occur at the surface level, the type of surface an object possesses can render it either highly useful or entirely impractical. Nanostructured coatings, for instance, can significantly increase an object's surface area, thereby enhancing the number of interaction sites and modifying properties such as surface wettability. Moreover, thin films have the capability to enhance or alter various properties of the substrate material, including optical, thermal, magnetic, electrical, and mechanical characteristics, while also providing protection against wear and corrosion [2]. The historical roots of thin coatings trace back to ancient Egypt, with the first documented production dating over 5000 years ago [1]. This early production involved laminating gold into thin films with thicknesses below 1 µm, primarily for aesthetic purposes.

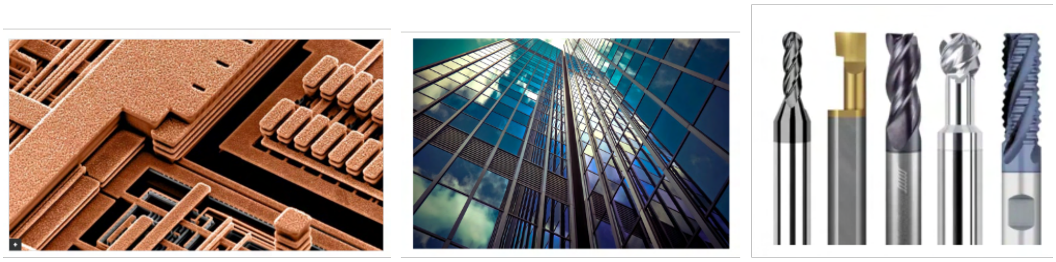

Figure 1: From the left: copper interconnect metallization in a transistor (SEM view after etching) , architectural glass coatings, coated cutting tools[1]

Only in recent decades, however, the industrial application and the development of this technology has reached worldwide several yields.

There are many other uses of this technology, ranging from semiconductor devices (displays, LED, lasers, biosensors, photodetectors), radiofrequency devices (thin film resistor), optical coatings (such us interference applications, for lens and mirrors), thin film battery (used, for example, in ultra-thin laptop or for implantable medical devices)[3], anti-corrosion, anti-scratch, anti-reflective, anti-ultraviolet coatings, and so on.

In Figure 1 1three possible applications are shown: a chip for microprocessors with copper interconnects obtained by chemical etching from a Cu thin film; architectural glass coatings, i.e., transparent layers deposited on the surfaces of glass panels to improve their thermal or optical properties, for example minimizing the amount of UV and IR light that can pass through; WC cutting tools coated with TiCN or AlTiN, in order to provide a thermal barrier between the tool and workpiece, improve tool lubricity and increase tool wear resistance.

Thin films also play a key role in the 2nd and 3rd generations' solar cells production, for which use of amorphous silicon thin film, or, more recently, indium gallium selenide (CIGS) and cadmium telluride (CdTe) is preferred, thanks to their production scalability, increased conversion coefficient and high absorption coefficient, that can reduce cost and material. In 2023, single-junction thin film GaAs solar cells reached a 29.1% efficiency and 47.6% with multi-junction concentrator technology[4]. Moreover, their flexibility makes them suitable for building integrated photovoltaics (BIPV).

The energy applications of thin films extend beyond the photovoltaic industry to include the solid-state batteries sector, such as thin-film lithium-ion batteries, as well as the nuclear industry.

Electricity plays a central role in various aspects of contemporary life within modern societies, and its significance is expected to grow further.

This expansionis particularly evident in the domains of transportation and heating, driven

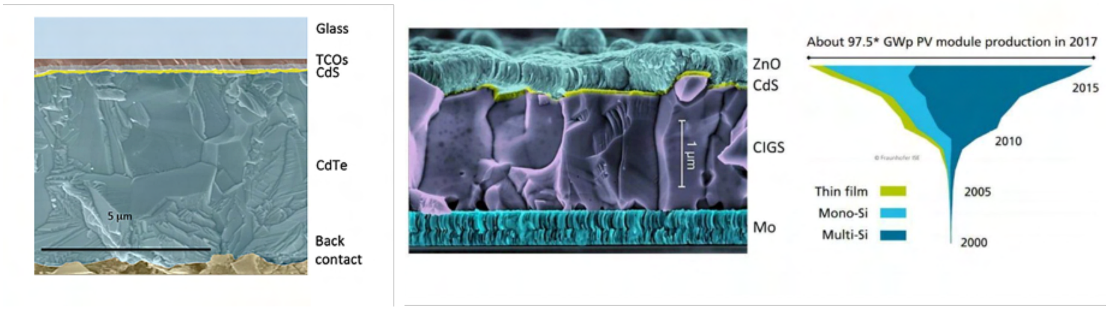

(a) (b)

Figure 2: Examples of PV application of thin films (a) and world production of different types of PV (b). Fig.taken from [2]

by advancements like electric vehicles and heat pumps. Presently, power generation stands as the primary contributor to global carbon dioxide (CO2) emissions. However, it paradoxically leads the charge in the shift towards achieving net-zero emissions. This transformation is fueled by the rapid adoption of renewable sources such as solar and wind power.

Simultaneously, the ongoing global energy crisis has thrust issues of electricity security and affordability to the forefront of political discussions in numerous countries[5].

The continuous increase in global electricity demand is due to the emerging and developing economies' growth and the progressive electrification of the energy-intensive sectors. According to IEA (Fig.3, [5]), in the next years more then 50% of the world electricity demand is set to come from China, India and Southeast Asia.

The current energy crisis has sparked a renewed focus on the potential of nuclear power to enhance energy security and decrease the carbon dioxide intensity associated with power generation: The anticipated growth rate for nuclear output is projected at 3.6% annually, primarily attributed to the escalation in Asia Pacific, coupled with the restoration of normal generation levels in France. By 2050, China alone will install an additional 500 GW of nuclear power, tenfold the current output (2023) of 57 GW[6]. Since the demand in the electricity market is almost inelastic, it is necessary for governments to intervene on the supply, trying to contribute to the development of new technologies that can provide a lower LCOE (levelized cost of electricity) and the optimal mix that can minimize the final energy price.

Several nuclear technologies' aim is to contribute to these scopes, both by increasing the efficiency respect to the traditional nuclear power plants and by widening and improving the carbon-free energetic mixes.

The reduction of the amount of high-level waste plays also a key role from the side of

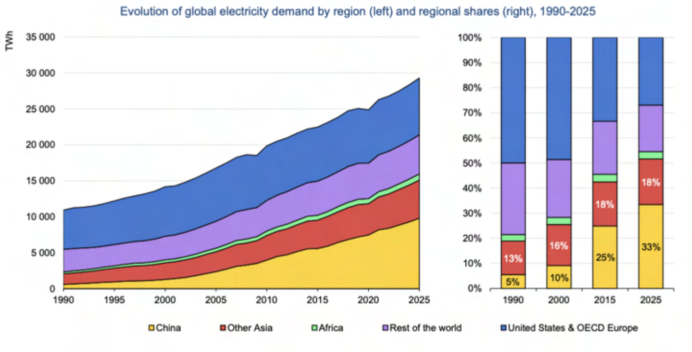

Figure 3: World energy consumption trend, Fig.taken from [5]

the social acceptance of nuclear technologies: Gen.IV nuclear power plants and fusion reactors offer great perspectives in this sense.

Several technological challenges and obstacles in these technologies, such as the extreme thermal loads and the huge neutron flux suggest the use of coatings in the form of thin film that can expand operational life, increasing the resistance of the most critical components to particle bombardment, irradiation embrittlement and high thermal loads [7].

Understanding the thermomechanical properties of thin films is crucial for selecting optimal coating materials, deposition techniques, and their parameters. However, characterizing thin films requires distinct methodologies and techniques compared to their bulk material counterparts. Due to their small dimensions, the influence of the substrate, and the not fully understood relationship between nanoscale structure and material properties, investigating the mechanical behavior of coatings poses a significant challenge[8].

In this work will focus on the applications of thin film on Generation IV technologies' components (in particular on Lead Fast Reactor) and on First Wall in Tokamak fusion reactors.

1 | Thin Film

In this chapter, a simplified model for the thin film mechanic behavior will be proposed; moreover, without entering into details of the deposition techniques used in this work, a qualitative correlation between the parameters involved and the final microstructure of thin films, and the influence of microstructure on their thermo-mechanical properties will be addressed.

1.1. Mechanical Behavior of a Thin Film on a Substrate

An analysis of the behavior of thin films, conducted under the following assumptions, is presented in the following:

- film has a uniform thickness and it is perfectly adherent to the substrate.
- deformations of film and substrate are in the linear-elastic domain; we can describe the stress-deformation constitutive relation using the Hooke Law. We'll see in section **1.2** how the model has to be modified if this condition is no longer true.
- The film and substrate are isotropic, at least in the plane of the substrate.
- Film thickness t_f is orders of magnitude lower then the substrate thickness t_s ($t_f << t_s$), so strain in the film can be approximated as uniform.
- Considering, for example, the situation of a thermal stress developed in the system due to the difference in thermal expansion coefficients between film and substrate, we assume a **pure biaxial state of stress**. According to the frame of reference of **Fig. 1.1**

$$\sigma_{xx} = \sigma_{zz} = \sigma_{biaxial} = E'\epsilon \tag{1.1}$$

$$E' = \frac{E}{1-\nu} \tag{1.2}$$

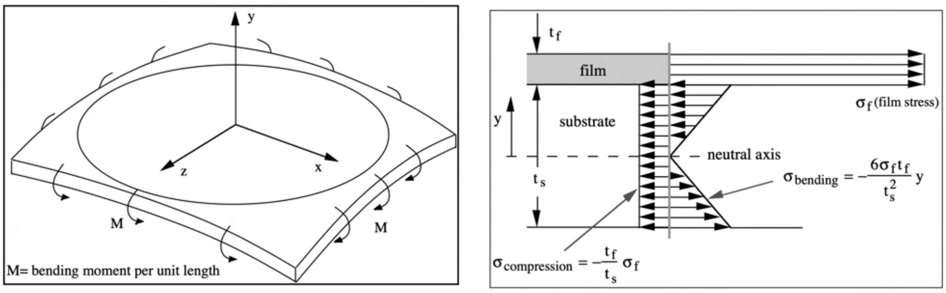
y
z
x
M
M
M= bending moment per unit length
t_f
film
substrate
y
t_s
neutral axis
σ_f (film stress)
$\sigma_{bending} = -\frac{6\sigma_f t_f}{t_s^2} y$
$\sigma_{compression} = -\frac{t_f}{t_s}\sigma_f$

Figure 1.1: On the left: biaxial stress induces a bending moment in the substrate; on the right: variation of biaxial stresses in the y-directions[9]

With E the Young's modulus, ν the Poisson's ratio and E' the biaxial elastic modulus. Every component of the stress tensor different from σ_{xx} and σ_{zz} is null. This approximation is valid if we consider a region far from the film's edges.

- Presence of native oxide layers on film's surface is neglected.

To better visualize the effect of a change in the film's dimensions, we can consider an initial stress-free situation (**Fig. 1.2**); then the film is detached from the substrate, its dimensions are allowed to change due to thermal expansion, densification, phase transformations or some other microstructural changes; in order to return to substrate's dimensions, a force has to be applied to the film. Finally, reattaching film to the substrate and removing external forces, relaxation leads to substrate curvature[10]. Lets call F the force per unit length in the film and σ_f the biaxial tension stress in the film, their relation is:

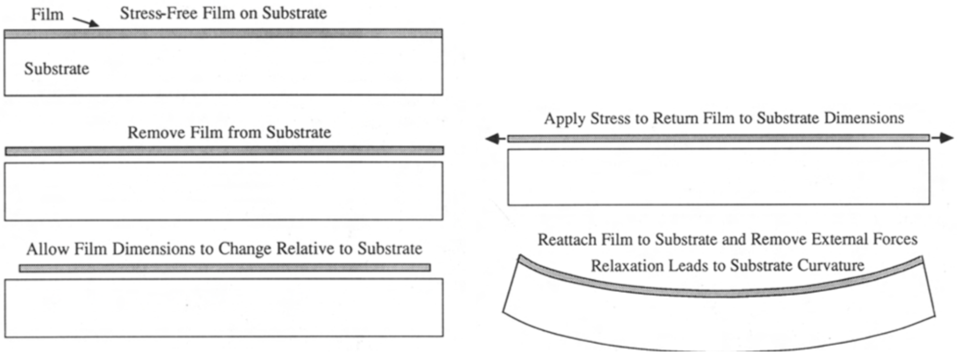
Film
Stress-Free Film on Substrate
Substrate
Remove Film from Substrate
Allow Film Dimensions to Change Relative to Substrate
Apply Stress to Return Film to Substrate Dimensions
Reattach Film to Substrate and Remove External Forces
Relaxation Leads to Substrate Curvature

Figure 1.2: Relation between axial stress in a thin film and the associated substrate bending. Figure from [10]

$$F = \sigma_f t_f \tag{1.3}$$

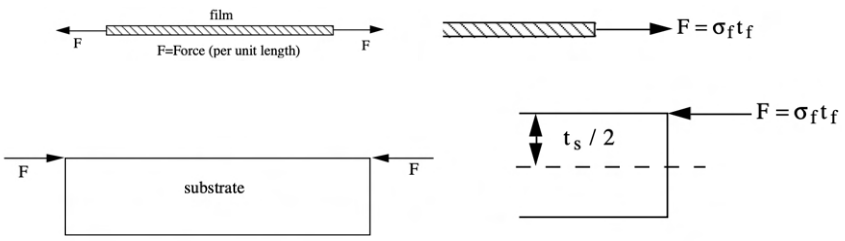

Figure 1.3: Forces acting on the film and substrate. Fig. from [10]

The force F, transmitted to the substrate, produce a bending. The bending moment per unit length associated is:

$$M = -\sigma_f t_f \frac{t_s}{2} \tag{1.4}$$

Let's divide the thin film and the substrate, and analyze the two separately (**Fig. 1.3**). Both in the film and in the substrate, stresses are biaxial, but it is convenient to distinguish the stresses associated with biaxial compression and biaxial bending in the substrate:

$$\sigma_{xx} = \sigma_{zz} = \sigma_{compression} + \sigma_{bending} \tag{1.5}$$

As shown in (**Fig. 1.1**) $\sigma_{bending}$ varies linearly with y-axis (pure bending):

$$\sigma_{bending} = \alpha y \tag{1.6}$$

with constant α. The moment M per unit length is given by:

$$M = \int_{-t_s/2}^{t_s/2} \sigma_b y \, dy \tag{1.7}$$

Combining Equation (1.6) and Equation (1.7) we can obtain a relation between M and $\sigma_{bending}$:

$$\sigma_{bending} = \frac{12M}{t_s^3} y \tag{1.8}$$

Then, combining Equation (1.4) and Equation (1.8):

$$\sigma_{bending} = -\frac{6\sigma_f t_f}{t_s^2} y \tag{1.9}$$

The compression component is given by:

$$\sigma_{compression} = -\frac{F}{t_s} = -\frac{t_f}{t_s} \sigma_f \tag{1.10}$$

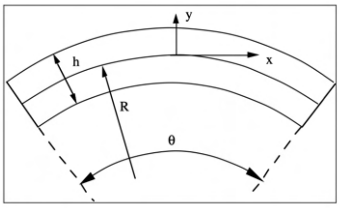

Figure 1.4: Curvature geometryFig. from [10]

Finally, combining Equation (1.5), (1.9) and (1.10) an expression for the total biaxial stress in the substrate as a function of y can be obtained. The value of the stress in substrate at interface is given by:

$$\sigma_{xx}(y = \frac{t_s}{2}) = -\frac{t_f}{t_s}\sigma_f - \frac{3t_f}{t_s}\sigma_f = -\frac{4t_f}{t_s}\sigma_f \tag{1.11}$$

It should be noted that, for typical geometries $t_f \approx 1\mu m$ and $t_s \approx 500\mu m$, substrate stress is about 100 times smaller than the film stress. So, far from the edges, the stresses in the substrate are small, compared to those in the film. Near the film edges, this is not true anymore: shear stresses(σ_{xy}) and normal stresses (σ_{yy}) develop at interface within a distance of few film thicknesses from the edges [10].

The presence of a passivation layer on the film surface does not strongly modify the stress state in the film beneath, since the ratio between its thickness and the film's one is similar to the ratio between the film and the substrate.

If the biaxial elastic modulus of the substrate is isotropic in its plane (orthotropic), then the film/substrate composite adopts the shape of a spherical shell [10]. Referring to **Fig. 1.4**, the deformation component ϵ_{xx} can be related to the curvature radius R through the equation:

$$\epsilon_{xx}(y) = \frac{(R+y)\theta - R\theta}{R\theta} = \frac{y}{R} \tag{1.12}$$

And, from the Hooke's Law and the approximation of pure biaxial stress:

$$\epsilon_{xx} = \frac{1}{E_s}(\sigma_{xx} - \nu(\sigma_{yy} + \sigma_{zz})) = \frac{1-\nu_s}{E_s}\sigma_{xx} \tag{1.13}$$

Because the film is, to good approximation, very thin compared to the substrate, the flexural rigidity of the film/substrate composite is the same as that for the substrate alone; therefore we have used substrate's Young's modulus and Poisson's ratio in our analysis, respectively E_s and ν_s.

Curvature is due to bending, so we use equation (1.9) for σ_{xx}. Combining that formula with (1.12) and (1.13), we obtain:

$$\epsilon_{xx}(y) = \frac{1-\nu_s}{E_s}\frac{6\sigma_f t_f}{t_s^2}y = \frac{y}{R} \tag{1.14}$$

Then, the curvature $\kappa = \frac{1}{R}$ is given by:

$$\kappa = \frac{1-\nu_s}{E_s}\frac{6\sigma_f t_f}{t_s^2} \tag{1.15}$$

The equation (1.15) is called **Stoney Relation**; it is of great importance since it allows us to calculate the stress in the film, if we are able measure the curvature. It is interesting to note that the result does not depend on the elastic properties of the film.

The stress in the film can be due to a film/substrate mismatch; if a difference in thermal expansion between film and substrate exists, the misfit strain is given by:

$$\epsilon_{misfit} = (\alpha_f - \alpha_s)(T - T_0) \tag{1.16}$$

Being α_f and α_s the linear coefficient of thermal expansion of the film and the substrate and $T - T_0$ the temperature jump, from a reference state in which strains are null. Referring again to **Fig. 1.2**, once the film is "reattached" to the substrate, both film and substrate deform elastically. Due to continuity and perfect adhesion, the condition below has to be true:

$$\epsilon_{misfit} + \epsilon_f^{elastic} = \epsilon_s^{elastic}(y = \frac{t_s}{2}) \tag{1.17}$$

We express the elastic strains as functions of σ_f using equations (1.11) and (1.13)

$$\epsilon_f^{elastic} = \frac{1-\nu_f}{E_f}\sigma_f; \qquad \epsilon_s^{elastic}(y = \frac{t_s}{2}) = -\frac{1-\nu_s}{E_s}(4\frac{t_f}{t_s}\sigma_f) \tag{1.18}$$

Combining equation (1.17) and (1.18), we obtain an expression for σ_f:

$$\sigma_f = -\frac{\epsilon_{misfit}}{[(\frac{1-\nu_f}{E_f}) + (\frac{1-\nu_s}{E_s})(\frac{4t_f}{t_s})]} \tag{1.19}$$

Because the substrate is much thicker than the film we can approximate this formula:

$$\sigma_f = -(\frac{E_f}{1-\nu_f})\epsilon_{misfit} = (\frac{E_f}{1-\nu_f})(\alpha_s - \alpha_f)(T - T_0) \tag{1.20}$$

As we will see in **Chapter 2** this relation permits to calculate the linear thermal expansion coefficient of the film, knowing the elastic properties of the film and the substrate, as well as the curvature-temperature relation.

This analysis is a good basis for later conducting analyses in more general cases where one or more of these assumptions are relaxed.

1.2. Microstructure and Mechanical Properties

Understanding how the microstructure of thin films influences their stiffness, strength, wear resistance or other properties is crucial

1.2.1. Deposition techniques

In this work two deposition techniques has been exploited at NanoLab@Polimi: **HiPIMS**(High Power Impulse Magnetron Sputtering) and **PLD** (Pulsed Laser Deposition), both belonging to the category of Physic Vapour Deposition techniques. It means that the material to be deposited enters in a condensed physical state in the reaction chamber, then it is evaporated and re-condensed as a thin film on a substrate.

In PLD, the film's material is vaporized from the target through an high-power pulsed laser beam; it forms a plasma plume that hit the substrate material. The deposition can occur in ultra-high vacuum or in presence of a background gas (such as oxygen or helium). The background gas pressure, the substrate temperature, the atomic mass of the target and many other parameters influence the final microstructure, such as the crystallinity, the mean grain's size, porosity or defects.

Sputtering techniques involves the action of accelerated gas ions (generally argon); impinging on the target thanks to a DC bias, they cause surface's atoms of the target to be sputtered. The sputtered atoms travel to the substrate, where they deposit onto the growing film.

HiPIMS makes use of remarkably high power densities, typically on the order of kW/cm^2, delivered in brief pulses lasting tens of microseconds with a low duty cycle (on/off time ratio) of less than 10%. What sets **HiPIMS** apart are its exceptional characteristics, including a significant level of ionization of the sputtered metal and a rapid molecular gas dissociation, resulting in the deposition of films with **exceptionally high density**[11].An increased ratio of hardness to Young's modulus compared to conventional PVD coatings is observed, thus a higher wear resistance[8].

With PLD, the microstructure can be tuned more accurately and the residual stresses are generally lower, but the final film thickness is less uniform than that achieved with

HiPIMS.

Substrate Bias and time delay in HiPIMS

HiPIMS belongs to this category; it utilizes negative voltage pulses applied to the target, that are typically 10 to 100 μ s in duration and have a low duty cycle to sputter the cathode target. This voltage setup enables operation at cathode target peak power densities ranging from 0.5 to 10 kW/cm^2, which is typically two orders of magnitude higher than the time-averaged values[12]. A negative voltage **bias** can be applied to the substrate, too, to improve thin film microstructure. The pulse duration of substrate bias can be equal to the target's one, and it can be shifted in time, by a quantity called **time delay** τ. Without entering into details, we can say that a time delay exists, the plasma still present in the chamber is more likely attracted on the substrate, causing a higher Ar^{++} incorporation in the film, resulting in a slightly lower density and cristallinity and higher residual stresses[12]. In this work, several W and WN samples, deposited under the same conditions, but with different time-delay, will be analyzed.

1.2.2. Thin Films' Microstructure

Owing to the non-equilibrium characteristics inherent in all vapor deposition methods, the ensuing properties and microstructure of thin films and interfaces typically exhibit a high degree of dependency on various deposition parameters. These parameters encompass deposition rate, temperature, gas pressure, impurities, substrate bias, and ion bombardment[13].

The processes of nucleation and growth on the substrate determine the crystallinity and the microstructure of the resultant films[14]: the lower is the film thickness, the higher is the importance of nucleation in determining the microstructure[15].

If, during deposition, certain conditions exist, the film growths as a single crystal: the substrate has to be a single crystal, it has be clean enough in order to avoid secondary nucleation and its temperature has to be high enough to give high mobility of growth species. A sufficiently low impinging rate can give time for surface diffusion and structural relaxation. If these conditions don't exist, the structure can be polycrystalline or amorphous[15].

A simplistic representation of expected film microstructure trends versus deposition parameters is called structure zone diagram (SZD)[16].

Figure 1.5 illustrates, in a preliminary approximation, how film growth varies by manipulating parameters in a PVD technique: both temperature and energy of the impinging particles play a fundamental role, as well as target current, voltage, pressure and sub-

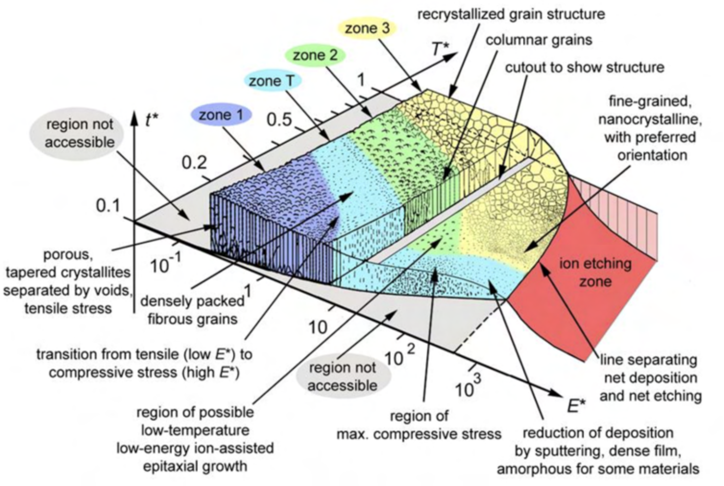
recrystallized grain structure
zone 3
columnar grains
zone 2
T^*
cutout to show structure
zone T
1
fine-grained, nanocrystalline, with preferred orientation
region not accessible
t^*
zone 1
0.5
0.2
0.1
porous, tapered crystallites separated by voids, tensile stress
10^{-1}
densely packed fibrous grains
1
ion etching zone
10
transition from tensile (low E^*) to compressive stress (high E^*)
region not accessible
10^2
line separating net deposition and net etching
10^3
E^*
region of possible low-temperature low-energy ion-assisted epitaxial growth
region of max. compressive stress
reduction of deposition by sputtering, dense film, amorphous for some materials

Figure 1.5: Structure Zone Diagram. The evolution of film's structure as a function of the generalized T(i.e., the homologous T, T_m, plus a characteristic temperature of a heated region affecting the rearrangement of N moved atoms) and normalized energy E of the impinging particles. Fig.from [16]

strate distance from target. Varying these parameters, the mobility of the atoms on the substrate surface, as well as the processes of defect generation and annihilation are modified; the structure can thus be amorphous and porous, fine-grained, fibrous, columnar and ultimately dense and with large grains.

If the film does not wet its substrate, the system tends to minimize its energy, promoting the nucleation of islands. Growing, they can coalesce and impinge upon each other[17], covering entirely the substrate and forming a continuous film with a polycrystalline structure[14]. The migration of grain boundaries after the impingement can lead to grain growth; as the size of the grains become comparable with the film, the surface energy of the grains' boundary becomes comparable with the energy of the free surface: this can prevent further growth of grains through the pinning of boundaries by surface grooving[17].

The atomic mass and the melting temperature T_m of the film's material are important in the final microstructure's determination; at low T, higher is the T_m and the atomic mass, lower is the atom's mobility, therefore there will be a higher tendency to form small and equiaxed grains, or an amorphous structure.

Usually, the grain size perpendicular to the film's plane closely matches the film's thickness. However, the grain sizes within the film's plane can vary significantly; generally, they are smaller for refractory materials and larger for FCC metals.

1.2.3. Residual stresses

Grain growth in polycrystalline films affects stress state and mechanical properties and at the same time is affected by them[18]. We can describe mainly several sources of biaxial strain related to the growth of polycrystalline thin films: intrinsic, extrinsic, densification-associated and deposition's parameters-dependent.

The intrinsic stresses are due to two contributions; the first is the coalescence of the islands: they deform in order to replace the free surfaces grain boundaries; the second is related to the difference in film and substrate lattice parameters, called epitaxial misfit. The formation of a continuous film leads to an elastic strain required to overcome the lattice mismatch, given by:

$$\epsilon_{em} = \frac{a_f - a_s}{a_f} \tag{1.21}$$

With a_f and a_s the lattice parameters of the film and the substrate, respectively. Both compressive and tensile stresses[19] can be generated. The order of magnitude is 1 GPa for sputter-deposited thin films.

The extrinsic stresses are linked to the difference in thermal expansion coefficient between the surface and the substrate. The resulting strain is described by the formula:

$$\epsilon_{th} = \int_{T_o}^{T} (\alpha_s - \alpha_f) dT \tag{1.22}$$

Where T_0 is initial temperature, T the actual temperature, and α_s and α_f the linear thermal expansion coefficients of the substrate and the film.

The last source of strain is described by the **densification** phenomenon: the increase of average size of grains leads to reduction of the energy associated with grain boundaries and redistribution of free volume in the film. This can promote a tensile stress, with the magnitude increasing sharply as the initial grain size increases, and a volume variation.

Being Δa the excess free volume per unit area of grain boundaries (compared to single crystal material) ($\sim$ 1A for FCC materials), and d and d_0 the final and initial grain dimensions, the strain related to densification is [18]:

$$\epsilon_d = \Delta a(\frac{1}{d} - \frac{1}{d_0}) \tag{1.23}$$

In a state of biaxial strain, the amount of energy density associated is different from grain to grain, depending on the specific orientation; in order to reduce this energy and relax the strain (stress relief mechanism), a grain-orientation specific driven force promotes the growth of grains with low biaxial moduli (the so-called **abnormal growth**), developing

a texture in the polycrystal.
The equilibrium between the strain energy density due to densification and the decrease of the surface energy associated with the coalescence of grains determines the final microstructure of the film.
For amorphous thin films, the increasing rate of tensile stress due to densification is proportional to the crystallization rate, hence to the annealing temperature. A typical “S” shape of the internal stress variation in time suggests a nucleation and growth mechanism of crystals[20].
There are sources of residual stresses related to the parameters involved in the deposition techniques. During deposition with sputtering techniques, Ar ions impinging on the target surface are neutralized and reflected; reached the film surface, they can be incorporated during film’s grow, dilating the material near the surface; the atomic collision process can also produce micro-plastic deformations, entirely similar to a conventional "peening" effect[21]. The result is a **compressive** residual stress.
Let’s consider a head-on elastic collision: if an Ar atom with an initial kinetic energy E_0 and mass m_{Ar} collide with a target atom m_t, the argon’s energy after the collision is given by:

$$E_{Ar} = E_0 (\frac{m_t - m_{Ar}}{m_t + m_{Ar}})^2 \tag{1.24}$$

Thus, if the target atom has a mass similar to Ar (i.e., 40 a.u.), the Ar energy tend to 0. After impinging on the target, Ar can impinge on the growing film. Higher is the target’s mass, higher is the Ar energy with which it impinges on the growing film; the compressive stresses tend to be more pronounced in target materials with higher atomic masses. If the **Ar pressure** is **low**, neutral argon atoms that are reflected from the target experience minimal collisions with other gas atoms as they travel toward the growing film. As a result, a significant number of energetic argon atoms reach the growing film, inducing high compressive stresses through a process known as "atomic peening". If the **Ar pressure** is **high** enough, numerous collisions within the gas hinder energetic argon atoms from reaching the growing film, thus causing natural processes that lead to tension (densification effect).

1.2.4. Mechanical properties

- **TF strength**: The yield stress of a polycrystalline film depends inversely on the average size of the grains, due to the well-known Hall-Petch strengthening, and the thickness of the film itself, due to the so-called dislocation relaxation mechanism: dislocation loops pinned at the film-substrate and film-native oxide interfaces nu-

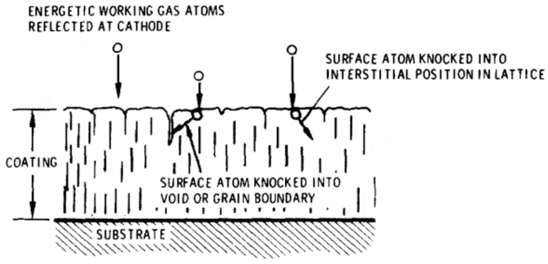
ENERGETIC WORKING GAS ATOMS
REFLECTED AT CATHODE
SURFACE ATOM KNOCKED INTO
INTERSTITIAL POSITION IN LATTICE
COATING
SURFACE ATOM KNOCKED INTO
VOID OR GRAIN BOUNDARY
SUBSTRATE

Figure 1.6: Interaction between working gas atoms and growing film. Fig.from[11]

cleate at grain boundaries, and they propagate through the grains[22]. Lower the thickness, higher the stress required to drive these dislocation loops[10]. Venkatraman and Bravman (1992) obtained a yield strength of 350 MPa in a 300 nm film of pure Al on Si substrates, which is almost fifty times the bulk material's one. For a film of pure Al of 800nm, the yield strength varies from 120 MPa (at 300°C) to 200 MPa (at 60°C).

The brittle materials exhibit a high strength as well as ductile materials: it is known that for these materials the strength depends on the average size and on the density of flaws. The typical small number and density per unit area of flaws in a thin film determines its high strength[20].

$$\sigma_y = \frac{c_1}{d} + \frac{c_2}{h} \tag{1.25}$$

With c_1 and c_2 constants, d is the mean grain size and h is the film thickness. c_1 and c_2 depend on the biaxial modulus, i.e. on the particular grain orientation; σ_y is greater for grains with (111) orientation. If a texture exists, the yielding stress is anisotropic[18].

- **Stiffness**: It is known from literature that the elastic constants of a bulk crystalline material do not depend on the grains' size and shape, and the presence of defects can affect those constants only for a few percent[13]. For an isotropic material the Young modulus is an average of the moduli associated to the different crystallographic orientations. For thin films, however, unexpected variations in elastic properties are found.

  Smaller is the grain size, closer the properties of thin films are to the amorphous material; larger they are, closer they get to the bulk material. The stiffness depends on the strength of the interatomic bonds, and so on the interatomic distance; in the case of an amorphous material or a quasi-amorphous one, the interatomic spacing is not unique, but it is described by a distribution whose width is inversely proportional to the mean grain size. Furthermore, lower is the degree of crystallinity, higher is the excess volume associated with grain boundaries and voids. A relation between cristallinity and density has been observed, as well as a relation between cristallinity and biaxial modulus[7]. The amorphousness and porosity of a material are related to a lower density, and a lower elastic modulus.

- **Defects and failure of thin films**: The presence of strong mechanical stresses can cause crack and delamination of the film. The delamination involves the adhesion of the film to the substrate, as well as the mechanical loading and its nature, thermal cycles and chemical environment[13]. Adhesion depends on the surface morphology, coating thickness, bonding across the interfacial region and the defect density at interface.
  Film cracking is often associated with delamination, if the adhesion is poor. In presence of compressive stresses, if the film is brittle and the substrate is ductile, delamination can occur through buckling mechanism at interface.
  On the other hand, is the same thing occur with a tensile stress, film cracks and detaches from the substrates starting from the edges[13].
  More ductile is the film, higher is the probability of a plastic-related failure mode, involving void growth, hillock formation, diffusional creep, grain boundary diffusion[23]. Jackson et al.[23] suggest that plastic flow is a key mechanism for relieving stress in these films and that this process can lead to the growth of **hillocks** on the film's surface during temperature cycles. Grain boundary diffusion due to diffusional creep mechanism does not relieve all the stresses in a thin film; vacancies diffuse inside the grain (Nabarro-Harring creep) or through them (Coble creep), relaxing partially the stresses, but, due to the adherence to substrate, some thermal stress remains within the grain. Then, through local plastic flow mechanism, elastic strain is converted to a non-elastic one, moving dislocations and feeding hillock growths and local thickening.
  During the **annealing** process the out-of-plane grain size reaches the height of the film. This relaxation mechanism, along with the local plastic flow, allows the reduction of the residual stresses through grain boundary diffusion.
  The increasing temperature produces a progressive decrease of yield strength due to the enhanced mobility of dislocations and the increase of mean grain's size.
  As said, once the out-of-plane's dimension of the grains reaches the film thickness, usually a traction stress develops (densification); Gao et al.[24] have proposed a mechanism for tensile stress relaxation: the material is transferred from the unpassivated surface of the film into the grain boundary. This diffusive flow results in the

creation of wedge-shaped defects along the grain boundary that exhibit high stress concentrations, which may significantly enhance dislocation plasticity in the thin film.

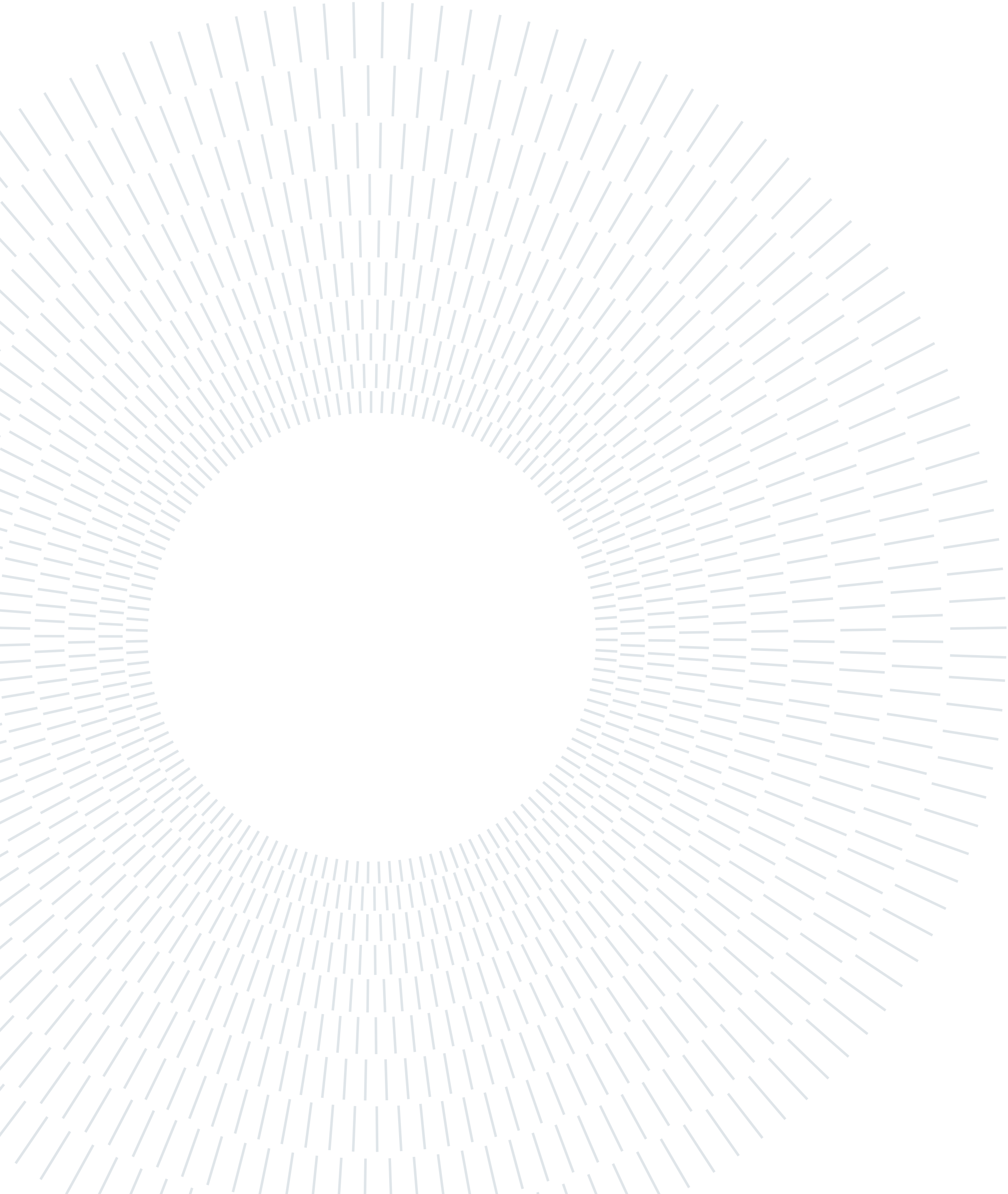

2 | Nuclear Materials

2.1. GEN IV reactors: LFR

Generation IV reactors represent a new advancement in fission reactor technology, characterized by their capability to utilize a broader neutron spectrum compared to Generation II and Generation III reactors. Currently in the prototype stage, the deployment of the first commercial plants is not anticipated until after 2030 [25]. Fast Reactors, a subset of Gen IV reactors, employ fast neutrons to trigger fission in Pu-239 or U-233. Simultaneously, they facilitate the transformation of fertile radionuclides into fissile ones through neutron capture, converting U-238 into Pu-239 and Th-232 into U-233. When the ratio between the number of fissile nuclei generated through the activation of fertile material and the number of fissile nuclei consumed in the fission and fertilization reaction exceeds one, the reaction has the potential to be self-sustaining. In such a scenario, the process becomes self-breeding, meaning it can produce more combustible material than is consumed in the reactions.

The conversion factor, denoted as C, is significantly influenced by the cross-section of the fertilization reaction, and by the mean number of neutrons produced. Several advantages arise from the potential use of a natural uranium blanket following an initial phase with high-enriched fuel (slightly under 20%). Additionally, the fuel composition can consist of depleted uranium or thorium matrices containing separated minor actinides from the spent fuel. This approach allows for the 'burning' of these minor actinides through neutron absorption, resulting in the production of much shorter half-life radioisotopes [26]. This process substantially reduces the time required for the spent fuel to attain natural uranium levels of radioactivity. For instance, a lead-cooled fast reactor with a thermal power of 750 MW and a 1 wt% loading of minor actinides can effectively consume 1.5 times the annual yields of minor actinides (such as Np-237, Am-241, and Am-243) from a pressurized water reactors (PWRs). This approach contributes to heightened sustainability by reducing nuclear waste volume and allowing for the potential use of reprocessed fuel, contingent upon local energy policies.

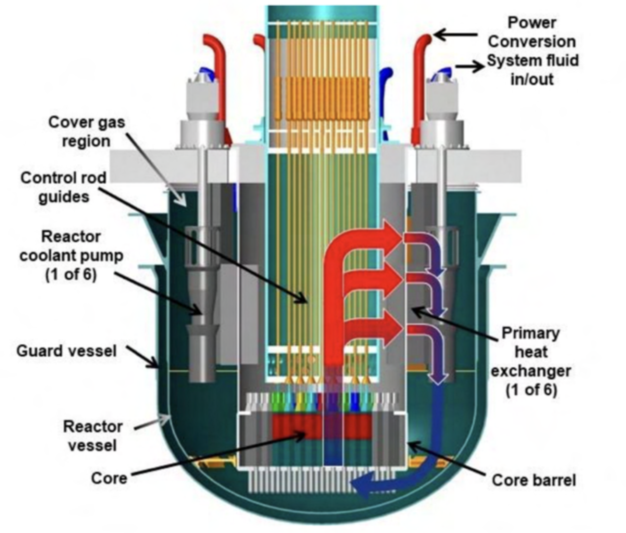

Figure 2.1: Westinghouse LFR [27]

Because fast neutron flux has to be maximized, the moderation has to be avoided. Instead o water, than, liquid metals or salts can be employed: due to their high mass, neutrons lose a very small fraction of their energy during elastic interaction. This substitution enables operation at significantly lower pressures when compared to boiling water reactors (BWR) and pressurized water reactors (PWR).

Lead Fast Reactor (LFR) uses liquid metal (Pb or Pb-Bi eutectic LBE) cooling at atmospheric pressure, exchanging heat by natural convection. Fuel is in the form of metal or nitride. A wide range of unit sizes is envisaged, from factory-built "battery" with 15–20-year life for small grids or developing countries, to modular 300-400 MWe units and large single plants of 1400 MWe. Operating temperature of 550°C is readily achievable, but 800°C is envisaged with advanced materials to provide lead corrosion resistance at high temperatures which would enable thermochemical hydrogen production [19].
In October 2015 Westinghouse announced that it had submitted an LFR project proposal for the DOE's upcoming investment in advanced reactor concepts demonstrable in the 2035 timeframe.
Scalability of this facility enables the adaptation of power output in plant evolutions to meet requirements of diverse future markets, while minimizing redesign efforts.
The lack of significant pressurization sources eliminates the necessity for a large, high-pressure-resistant containment structures seen in conventional plants. Operating at elevated temperatures, the LFR achieves higher efficiencies compared to conventional nuclear plants (up to 42% in the LBE cooled ALFRED, Advanced Lead-cooled Fast Reactor Eu-

ropean Demonstrator)[27][28].

2.1.1. Technological challenges in LFR structural materials

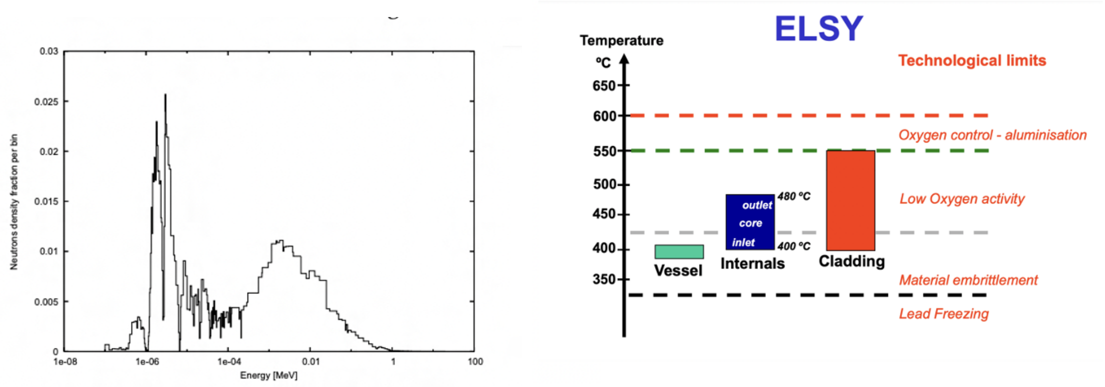

(a) (b)

Figure 2.2: (a)Neutron energy spectrum in an ALFRED type LFR. Two peaks, the first linked to the thermal and the second to the fast neutrons can be observed[29], (b)Temperature and effects at which different component of a ELSY LFR are subjected to[30].

The high neutron flux (up to 10^{15} n/cm^2s for fast and 10^{13} n/cm^2s for thermal neutrons in a 300MW ALFRED type reactor [31]) in an LFR is necessary due to the relatively low high-energy-neutron fission cross-section of fissile materials of interest.

Exposing materials to highly energetic particles, such as neutrons and fission fragments can induce atomic displacement and lead to various changes in microstructure. These alterations can encompass transitions from a crystalline to an amorphous phase or viceversa, as well as the formation of significant concentrations of point defects or solute aggregates within crystalline lattices[32].

Moreover, the presence of a fluent liquid metal can enhance liquid metal corrosion phenomena (LMC) and liquid metal embrittlement (LME), which cause strong degradation of materials properties. The fuel claddings are the components that most suffers critical conditions, such as high temperatures (up to 550°C in ELSY project, see Appendix A or 640°C in BREST project), neutronic irradiation, thermomechanical solicitation and Pb corrosion. Studying the solutions for the protection of the structural materials, the opportunity represented by use of thin film coatings permits to increase the material existence without altering its mechanical properties. Nanocrystalline Al_2O_3 dispersed within an amorphous matrix, deposited via PLD, exhibited robust adhesive properties to steel substrates, minimal porosity, and a peculiar metal-like plastic behavior. Additionally, it displayed remarkable hardness, stiffness, and durability and a good resistance to LMC and LME[33][8][34]. Irradiation's impact on amorphous-nanocrystalline alumina primarily manifests as recrystallization and grain growth (refer to Appendix A). Therefore, annelling of the samples through thermal cycles can qualitatively mimic the microstructural transformation under irradiation.

The effectiveness of yttria (Y_2O_3) and lanthanum oxide in stabilizing the γ phase, impeding its transformation into the more stable sapphire phase, has been established. In terms of metallic coatings, both Fe-Cr-Al and Fe-Al alloys showcase remarkable resistance against corrosion in oxygen-rich liquid lead, enduring 5000 hours at 500°C without any observable erosion or corrosion on the Fe-Al coating surfaces. Although their behavior under intense irradiation remains relatively unexplored, the proposition of utilizing Al as metallic coatings for internal structures, steam generators, DHR heat exchangers, and primary pumps on AISI 316LN substrates has been made[33].

This study extensively investigates Al specimens deposited through HiPIMS and DC magnetron sputtering, aiming to evaluate their thermomechanical and microstructural stability.

A sample of Y_2O_3 deposited with PLD has been characterized, too. More details about irradiation effects, LMC and LME and the materials for LFR structural components in **Appendix A**.

2.2. Fusion reactors

2.2.1. Tokamak reactor

Without delving into the intricacies of nuclear fusion reactors, let's briefly touch upon the energy production, heat transfer, and materials associated with the most critical components of the TOKAMAK reactor, currently under construction as part of the ITER project. The toroidal vacuum chamber will contain a plasma volume of 840 m^3 (Fig,.2.4). The fusion reaction of interest is between deuterium ^2D and tritium ^3D, the hydrogen isotopes with, respectively, one and two neutrons. The fusion between deuterium and tritium (DT) nuclei produces one helium nucleus, one neutron, and great amounts of energy. At extremely high temperatures, electrons become detached from the nuclei, resulting in the formation of plasma—an ionized state of matter. To achieve fusion in a laboratory setting, three conditions must be met: an exceedingly high temperature, approximately 150 million °C, to induce high-energy collisions; an adequate density of plasma particles to enhance the probability of collisions; and a sufficient confinement time to retain the

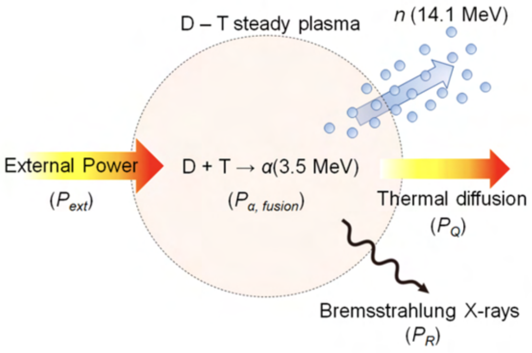
D – T steady plasma
n (14.1 MeV)
External Power
(P_{ext})
D + T → α(3.5 MeV)
($P_{α, fusion}$)
Thermal diffusion
(P_Q)
Bremsstrahlung X-rays
(P_R)

Figure 2.3: Fusion reaction between D and T[7]

plasma, which tends to expand, within a defined volume[35].

While He nucleus produced (charged particle) remain in the plasma and provide enough energy to make the reaction self-sustained, neutrons, which represents almost 80% of the energy produced, are unaffected by the magnetic fields. These neutrons are absorbed by the surrounding walls of the tokamak, transferring their kinetic energy to the walls mainly in the form of heat.

In ITER, this heat is captured by circulating cooling water within the vessel walls. Subsequently, the heat is harnessed to produce steam, leading to the generation of electricity through the use of turbines. The dissipation of excess heat is facilitated through cooling towers.

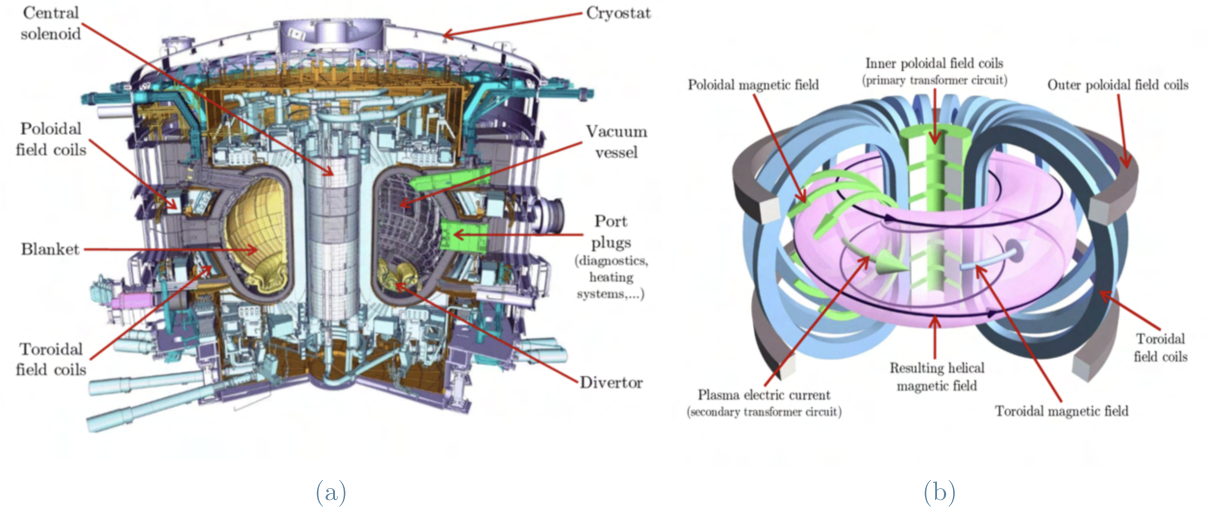
Central solenoid
Cryostat
Poloidal field coils
Vacuum vessel
Blanket
Port plugs (diagnostics, heating systems,...)
Toroidal field coils
Divertor
Poloidal magnetic field
Inner poloidal field coils (primary transformer circuit)
Outer poloidal field coils
Toroidal field coils
Resulting helical magnetic field
Plasma electric current (secondary transformer circuit)
Toroidal magnetic field
(a)
(b)

Figure 2.4: Tokamak reactor[36]

2.2.2. Plasma Facing Materials

PFCs (Plasma Facing Materials) are the systems directly exposed to the thermonuclear plasma (Fig.[7]) and they are constituted by the first wall regions: blanket2.4, which can provide heat transfer to water, and divertor. The materials that make up PCFs are called Plasma Facing Materials (**PFMs**), and their interactions with plasma fall under the so-called Plasma Wall Interactions (**PWIs**). The scope of the divertor is the extraction of heat and ash produced by the fusion reaction, minimizes plasma contamination, and protects the surrounding walls from thermal and neutronic loads.
The inner and outer vertical targets are positioned at the intersection of magnetic field lines where particle bombardment will be particularly intense in ITER (Fig.2.5,[35]).

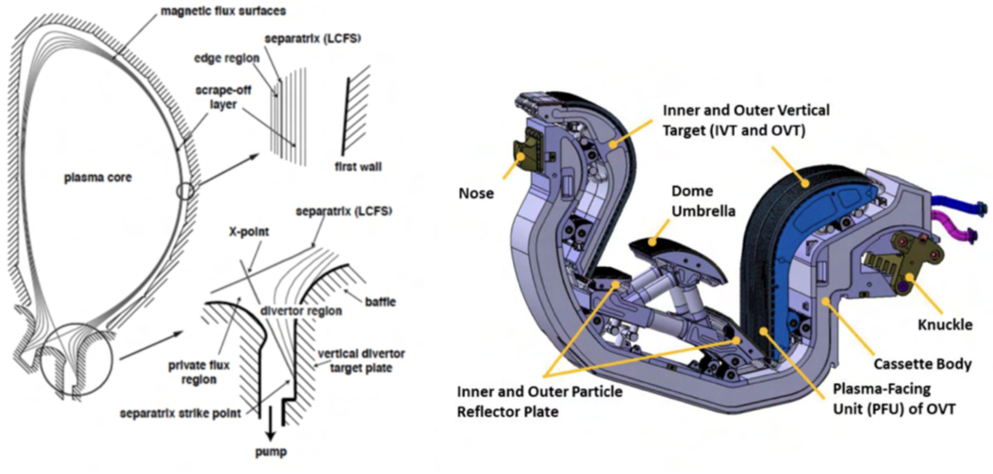
magnetic flux surfaces
separatrix (LCFS)
edge region
scrape-off layer
plasma core
first wall
separatrix (LCFS)
X-point
baffle
divertor region
vertical divertor target plate
private flux region
separatrix strike point
pump
Inner and Outer Vertical Target (IVT and OVT)
Nose
Dome Umbrella
Knuckle
Cassette Body
Inner and Outer Particle Reflector Plate
Plasma-Facing Unit (PFU) of OVT

(a) (b)

Figure 2.5: (a)Divertor position and magnatic fiel lines in a section of the toroid[37] , (b)Divertor's components[38]

The particle flux delivered by the plasma in the divertor region, about 10^{24}m^{2}s^{-1}, and the temperatures, between 1100 °C (corresponding to steady state power, 10 MWm^{-2}) and 2000°C (corresponding to the peak power of 20 MWm^{-2}), are particularly intense. Moreover, if plasma instabilities occur, the thermal load at divertor can reach 2 GWm^{-2}. Most materials at these conditions completely fail, losing all their mechanical properties, and, if several GWm^{-2} are reach, even most materials with the highest melting point will liquefy or evaporate [7]. We can distinguish between the 'atomistic effects', due to particle flux, and the 'thermal effects', due to high T and thermal loads.

Atomistic Effects The impact of n, 2D, 3T, He on the divertor produces several effects, in addition to those already described.

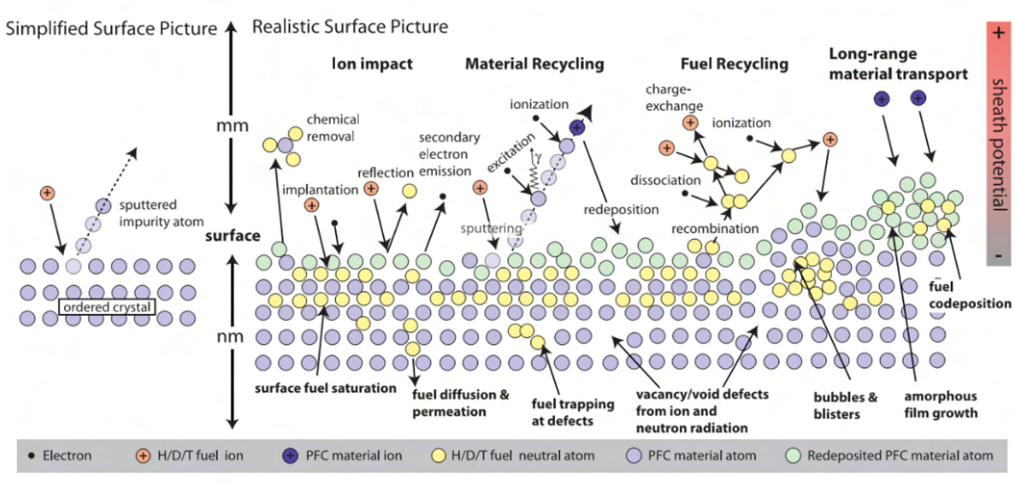
Simplified Surface Picture
Realistic Surface Picture
mm
surface
nm
Ion impact
Material Recycling
Fuel Recycling
Long-range material transport
+
sheath potential
-
sputtered impurity atom
ordered crystal
chemical removal
implantation
reflection
secondary electron emission
ionization
excitation
γ
sputtering
redeposition
charge-exchange
ionization
dissociation
recombination
fuel codeposition
surface fuel saturation
fuel diffusion & permeation
fuel trapping at defects
vacancy/void defects from ion and neutron radiation
bubbles & blisters
amorphous film growth
Electron
H/D/T fuel ion
PFC material ion
H/D/T fuel neutral atom
PFC material atom
Redeposited PFC material atom

Figure 2.6: Atomistic effects in presence of high-energy particles.[7]

- **Nuclear transmutation**: neutron irradiation induce transmutation, then creation of multicomponent alloys, which can modify the thermo-mechanical properties of the material, and generation of nuclear waste, resulting from the formation of radioactive components.

- **Implantation of nuclear fuel**: D, T, He enter the PFM due to their small size, they thermalize, then accumulate at lattice defects. When surface is saturated, they diffuse and are trapped by bulk defects. The fuel retention can cause both fuel loss and radiation protection issue for First Wall materials; limit of T retention is 700g[7].
  In supersaturation conditions of H and He beneath the surface, micrometric swelling and surface deformations (**blistering**) occurs, with cracks and protrusions as a consequence.

- **Erosion**: most important detrimental process that take place in a TOKAMAK. It involves high energy particles, and induce sputtering; hit atoms does not induce a collisional cascade, but are ejected from the surface. The colliding particles can exceed target atoms' bonding energy (**physical sputtering**) or create chemical compounds with the target in presence of low Z materials, mainly C, O, N, Be (**chemical sputtering**).
  Physical sputtering is a threshold process; in order to minimize the probability of this event, the threshold energy has to be maximized, e.g., **maximizing the atomic mass of the target** material.

> Each eroded particle re-deposits on PFMs creating a layer or co-deposits if it is chemically bonded to fuel elements or low Z elements. The result is the growth of a layer with an unknown microstructure (hence an unpredictable behavior) and a weak cohesion with the substrate, that lead to the production of dust, that contaminate the plasma and increase the radiative losses.

Thermal Effects In the presence of thermal loads reaching up to 20 $\mathrm{MWm^{-2}}$ and elevated temperatures, deleterious effects such as erosion, recrystallization (resulting in significant alterations to surface roughness), cracking, and evaporation may manifest. Furthermore, a substantial number of thermal cycles can give rise to thermal fatigue.

2.2.3. Candidate materials and coatings for PMCs

Suitable PFMs: Tungsten, CFC, Be

To alleviate thermal and atomistic effects, researchers seek materials characterized by high melting temperatures, elevated thermal conductivity and diffusivity, substantial yield and ultimate strength, resilience to neutron damage, low sputtering yield, and minimal nuclear fuel retention. High Z materials (such as W) has generally lower fuel retention and lower sputtering yield, but they tend to contaminate plasma through radiative losses. On the contrary, low Z materials (such as carbon fiber composites CFC and Beryllium) show a high chemical sputtering yield and a low contamination[39]. **Tungsten**

Tungsten is a material with a BCC structure. It has the highest melting point (3420 °C), a good thermal conductivity (174 $\mathrm{W\ m^{-1}K^{-1}}$) and a very low sputtering yield and fuel retention: it reaches the retention fuel limit after about 2500 plasma discharges; it recrystallizes at 1200°C (higher than the typical divertor temperature, 1100°C). For these unique features, it is suitable for PFCs both in bulk and thin film form.

At 2000°C, creep and thermal fatigue occur. Blistering occurs between 25°C and 600°C if the particle flux is higher than 10^{24} $\mathrm{m^{-2}s^{-1}}$. As the bubbles interconnect, embrittlement occurs even at T higher than the brittle-ductile transition temperature. Agglomerations of W/W-Be or multielemental deposits of W with C, Ni, Al, Si, B, N, O have been observed after JET-ILW experimental campaign[7].

The radiation damage for W at the end of reactor's life is expected to be 0.6 dpa.

Bulk W

Bulk W has a high density (19.3 g/cm^3) and excellent mechanical properties (Elastic modulus E=400 GPa and hardness H=3.92 GPa)[40]. Inner and outer vertical targets of the divertor can be constituted by W monoblocks (AUG 2013 project, Div-III divertor).

HHF (high heat flux fatigue test) qualification tests conducted on the ITER divertor target prototypes showed that the tungsten monoblock armor suffered from deep cracking due to fatigue, when the applied heat flux approaches 20 MWm^{-2}.

Thin film W

Coated W PFCs have been widely investigated using CFC or graphite as substrates. The are several advantages in using thin films: it allows for greater flexibility in design and integration into complex geometries and their atomic structure can be engineered to enhance resistance to erosion and sputtering. If thickness of the film is too high, i.e., fractions of millimeters, intense thermal loads can induce delamination[7]; if it is too thin, it can be completely eroded after few plasma discharges.

Besozzi et al.[41] exploited nanosecond laser impulses irradiation for simulation of thermal loads that occur during plasma instabilities. They compared bulk W with nanostructured W based coatings (columnar-W, amorphous-W, porous-W) on Si substrates, representative of W coatings and co/re-deposited layers in tokamaks. The best performances have been observed for columnar-W, the most compact and rigid one. The crack threshold started at thermal load slightly higher than the bulk one: the preferential orientation helps to mitigate cracking[41]. The recrystallization and melting thresholds for this kind of coating are slightly lower than the bulk one.

Amorphous and porous coatings, instead, show significantly poorer properties, due to lower diffusivity (85% reduction in melting threshold for $a - WO_3$ in respect to bulk W) and the enhanced formation of bubbles and “fuzzy” morphology.

Seedeing and detachment regime: WN

To address the challenge of excessive heating in the ITER divertor, the baseline strategy for sustaining burning plasmas involves transitioning to a partially detached regime. In this state, the goal is to convert a significant portion of the energy carried by charged particles into radiation, thereby mitigating the problem of localized heat flux deposition. Achieving detachment can be facilitated by introducing specific impurities, which are typically strong radiators. This impurity injection, such as nitrogen gas, not only aids in enhancing radiation but also contributes to power removal[42]. Adding nitrogen gas near the divertor, the plasma is slowed down; redeposited N can react with W, forming WN. If the atomic percentage of N is low (1-30%), intermetallic phases cannot crystallize, so an amorphouse phase is created.

WNs compounds are characterized by an high hardness and a high H/E ratio, so they are studied for several applications, such as anti-wear coatings and diffusional barriers for semiconductors. In this work, high compact WN coatings deposited with HiPIMS are studied.

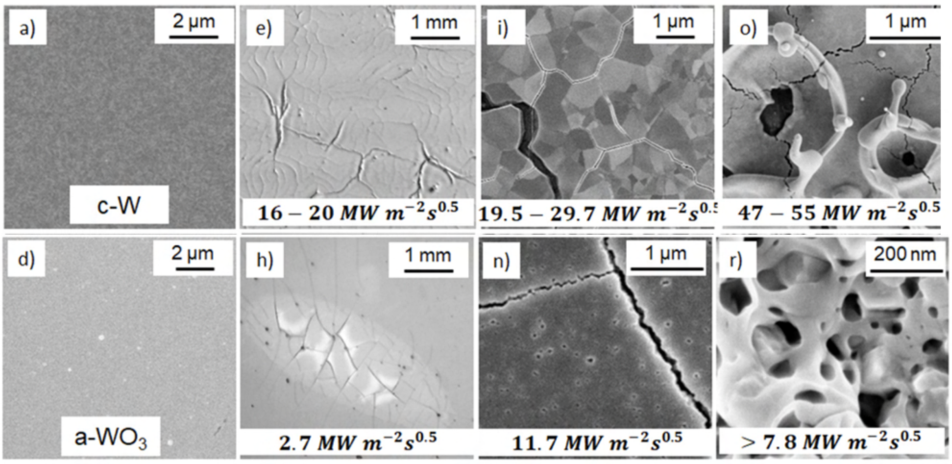
a)
2 µm
c-W
e)
1 mm
$16 - 20\ MW\ m^{-2} s^{0.5}$
i)
1 µm
$19.5 - 29.7\ MW\ m^{-2} s^{0.5}$
o)
1 µm
$47 - 55\ MW\ m^{-2} s^{0.5}$
d)
2 µm
a-WO_3
h)
1 mm
$2.7\ MW\ m^{-2} s^{0.5}$
n)
1 µm
$11.7\ MW\ m^{-2} s^{0.5}$
r)
200 nm
$> 7.8\ MW\ m^{-2} s^{0.5}$

Figure 2.7: Crystalline and amorphous W after different laser-simulated thermal loads. Figure from [41]

3 | Thermo-mechanical Characterization of TF

3.1. Introduction

In the field of mechanical characterization, samples of bulk material are subjected to various forces or displacements and their responses are measured. These methods are inadequate for examining the mechanical characteristics of thin films on substrates since the films of interest usually measure $1\mu m$ or less and are bonded to the substrate[10]. In order to measure stresses that develop in thin films, two approaches are used:

- **X-ray diffraction**: allows the direct measurement of the elastic strain in the film. It permits, in principle, to detect all the components of the stress tensor and their spatial variations, even from grain to grain. It is based on diffraction, therefore it cannot be used for non-crystalline materials.

- **Wafer-curvature technique**: It involves determining stress by measuring the curvature or deflection of the substrate. This method is applicable to various materials and offers convenience compared to X-ray diffraction, especially in specific conditions such as *in-situ* heating or cooling, and film growth processes [10]. Utilizing the Stoney equation (1.15), knowledge of both the film thickness and substrate properties is essential. In this study, the technique has been applied through laser beam deflection to assess film stress and the linear thermal expansion coefficient. (section 3.3).

To evaluate the elastic properties of thin films, the following techniques are under consideration:

- **Nanoindentation**: Nanoindentation involves measuring the forces required to create small indentations in thin films on a substrate. This method provides valuable information about the elastic and plastic properties of films, including parameters such as Young's modulus, Poisson's ratio, and hardness [8][10].

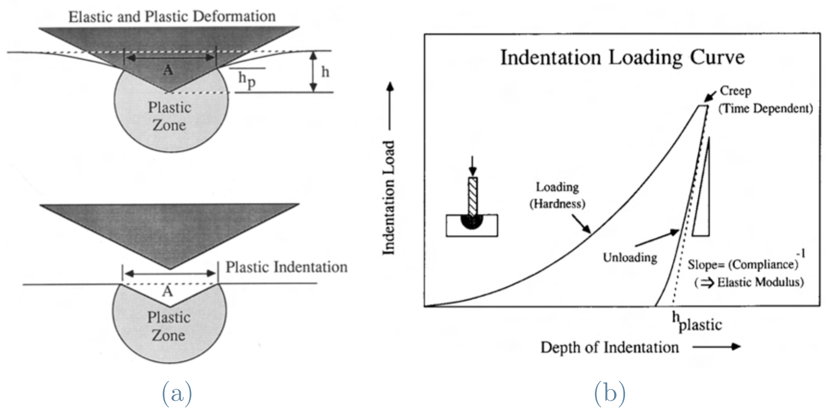
Elastic and Plastic Deformation
A
h_p
h
Plastic Zone
Plastic Indentation
A
Plastic Zone
Indentation Loading Curve
Creep (Time Dependent)
Loading (Hardness)
Unloading
Slope= (Compliance)$^{-1}$ (⇒ Elastic Modulus)
Indentation Load
$h_{plastic}$
Depth of Indentation

(a) (b)

Figure 3.1: Elasto-plastic deformation associated to indentation(a), Loading-Unloading curve in nanoindentation(b)[10]

During unloading (**Fig. 3.1b**), elastic deformation is recovered. The load-depth curve is associated with material elastic modulus.

This technique's limitations stem from potential non-linear effects and the necessity for high-resolution nanoindenter displacement. A high hydrostatic pressure is developed under the nanoindenter, therefore densification can occur in the film, as well as a phase-change; the calculated Young's modulus can be higher than the real one, especially for amorphous and porous materials. Moreover, the influence of the substrate in hardness measurements strongly depend of the substrate hardness and the indentation depth. Usually, for soft films on hard substrates, the indentation depth should be a small fraction of the film thickness to avoid substrate influence: a high displacement resolution is then required.

- **Brillouin light scattering (BLS) spectroscopy**: Exploiting the interaction between light and thermally stimulated acoustic excitations in solids, such as phonons and spin waves, information about elastic constants of the material are deduced. Since it involves low-power laser pulse, it is a completely non-destructive technique (NDT). It has been extensively used in this work, and it is described in section 3.2.

3.2. BLS spectroscopy

To comprehend a Brillouin Light Scattering (BLS) spectrum, it is essential to evaluate the specific type of elastic waves that are under investigation when light interacts with the solid material; then, we are going to extend the reasoning to thin film on substrate.

3.2.1. Bulk and Surface Elastic Waves in a solid

At first, let's consider an isotropic continuum with a linear elastic behavior and a cartesian frame of reference (x_1, x_2, x_3) coincident with the symmetry axes. Considering a generic displacement field $\mathbf{u}$ and the related strain tensor ϵ_{ij} such that:

$$\epsilon_{ij} = \frac{1}{2}\left(\frac{\partial u_i}{\partial x_j} + \frac{\partial u_j}{\partial x_i}\right) \tag{3.1}$$

Where u_1, u_2 and u_3 are the displacements in the x_1, x_2, x_3 directions. The generalized Hooke's Law for an isotropic material relates the stress tensor σ_{ij} to the strain tensor through the *stiffness tensor* C_{ijkl} with only two indipendent constants, C_{11} and C_{44}.

$$\begin{bmatrix} \sigma_{11} \\ \sigma_{22} \\ \sigma_{33} \\ \sigma_{12} \\ \sigma_{13} \\ \sigma_{23} \end{bmatrix} = \begin{bmatrix} C_{11} & C_{12} & C_{12} & 0 & 0 & 0 \\ C_{12} & C_{11} & C_{12} & 0 & 0 & 0 \\ C_{12} & C_{12} & C_{11} & 0 & 0 & 0 \\ 0 & 0 & 0 & C_{44} & 0 & 0 \\ 0 & 0 & 0 & 0 & C_{44} & 0 \\ 0 & 0 & 0 & 0 & 0 & C_{44} \end{bmatrix} \begin{bmatrix} \epsilon_{11} \\ \epsilon_{22} \\ \epsilon_{33} \\ \epsilon_{12} \\ \epsilon_{13} \\ \epsilon_{23} \end{bmatrix} \tag{3.2}$$

With the isotropic condition:

$$C_{11} - C_{12} - 2C_{44} = 0 \tag{3.3}$$

Thus, equation (3.2) becomes:

$$\sigma_{ij} = \sum_{(i,j,k,l)=1}^{3} C_{ijkl}\epsilon_{kl} = \sum_{(i,j,k)=1}^{3} (C_{12}\delta_{ij}\epsilon_{kk} + 2C_{44}\epsilon_{ij}) \tag{3.4}$$

In absence of volume forces and forces on the boundaries, displacements in the solid are due only to **thermal vibrations**. Given the material density ρ, the time-dependence of displacements' components is described by the first dynamic cardinal equation:

$$\rho\frac{\partial^2 u_i}{\partial t^2} = \sum_{k=1}^{3} \frac{\partial \sigma_{ik}}{\partial x_k} \tag{3.5}$$

that, combined with (3.4) and (3.1) gives:

$$\rho\frac{\partial^2 u_i}{\partial t^2} = \sum_{k=1}^{3} \frac{\partial \sigma_{ik}}{\partial x_k} = \sum_{(j,k,l)=1}^{3} C_{ijkl}\frac{\partial^2 u_i}{\partial x_j \partial x_k} \tag{3.6}$$

For the component u_1 in an isotropic solid, eq. (3.6) becomes [43]:

$$\rho\frac{\partial^2 u_1}{\partial t^2} = C_{11}\frac{\partial^2 u_1}{\partial x_1^2} + C_{44}(\frac{\partial^2 u_1}{\partial x_2^2} + \frac{\partial^2 u_1}{\partial x_3^2}) + (C_{11} - C_{44})(\frac{\partial^2 u_2}{\partial x_1 \partial x_2} + \frac{\partial^2 u_3}{\partial x_1 \partial x_3}) \tag{3.7}$$

Eq. (3.6) is the so-called *wave equation*, and admits *D'Alambert* solutions:

$$u(x,t) = A(t - \frac{x}{v}) + B(t + \frac{x}{v}) \tag{3.8}$$

Defining the wavevector $\mathbf{k} = k(l_1\hat{x_1} + l_2\hat{x_2} + l_3\hat{x_3})$, the angular frequency ω, and the polarization vector $\mathbf{A} = A_1\hat{x_1} + A_2\hat{x_2} + A_3\hat{x_3}$ the simplest solution to the eq. (3.6) is the plane wave:

$$\mathbf{u}(\mathbf{x},t) = \mathbf{A}e^{[i(\mathbf{kx} - \omega t)]} \tag{3.9}$$

The wavelength, frequency and phase velocity associated are, respectively, $\lambda = 2\pi/k$, $\nu = \omega/2\pi$, $v_{ph} = \omega/k$. For a generic diplacement's component:

$$u_j = A_j e^{[ik(l_i x_i - v_{ph} t)]} \tag{3.10}$$

Substituting eq. (3.10) into eq. (3.6) we obtain the **Christoffel equation**:

$$det(\Gamma_{ij} - \delta_{ij}\rho v_{ph}^2) = 0 \tag{3.11}$$

With Γ_{ij} the Christoffel tensor, defined as:

$$\Gamma_{ij} = \sum_{i,l=1}^{3} \frac{1}{2}(C_{ijkl} + C_{ijlk})l_i l_l \tag{3.12}$$

Note that the Christoffel equetion as presented in eq.(3.11): it is valid for any material, isotropic, completely anisotropic, or with a particular crystal symmetry.

For a given stiffness tensor and a given wavevector, a set of velocities $v_{ph,n}(\mathbf{k})$ solves the polynomial equation; n corresponds to the number of modes, thus to the number of degrees of freedom in the system (3).

These velocities correspond to the components of the displacement field (3.9) parallel (1 mode) and orthogonal (2 modes) to the wavevector $\mathbf{k}$; in the first case, the perturbation direction and the propagation direction are the same, and the associated mode is called

longitudinal wave or *primary wave* (**P-wave**); in the second cases, the modes are called *transverse waves* or *shear waves* (**S-waves**) and the oscillation is perpendicular to **k**.
If the material is isotropic, v_{ph} do not depend on the direction, but only on the constant C_{11} and C_{44}. If we consider a longitudinal sound wave propagating in the $\langle 100\rangle$ direction of a cubic crystal $(\mathbf{u}(\mathbf{x},t)_{P,\langle 100\rangle} = u_1(x_1,t)\hat{x_1})$, and (3.7) becomes:

$$\rho\frac{\partial^2 u_1}{\partial t^2} = C_{11}\frac{\partial^2 u_1}{\partial x_1^2} \tag{3.13}$$

Substituting the expression $u_1 = A\exp\left[i(k_{x_1}x_1 - \omega t)\right]$ into (3.13) , we obtain the dispersion relation:

$$\rho\omega^2 = C_{11}k_{x_1}^2 \tag{3.14}$$

The longitudinal velocity is:

$$v_{ph,l} = \frac{k_{x_1}}{\omega} = \sqrt{\frac{C_{11}}{\rho}} \tag{3.15}$$

Analogously, two coincidence degeneres transverse velocities are found:

$$v_{ph,t1} = v_{ph,t2} = \sqrt{\frac{C_{44}}{\rho}} \tag{3.16}$$

For an isotropic material, C_{44} is equal to G, the shear modulus, so a shear wave is a propagation of periodical shape deformations; higher is the transverse velocity, higher is the resistance of the material to a shape variation. C_{11}, instead, correlates with the bulk modulus K ($K = (C_{11} + 2C_{12})/3$), indicating the extent of volume alteration under a specific hydrostatic stress condition. Therefore, P-waves is a propagation of volume's variations. For a cubic crystal the (3.3) is not true, so there are three indipendent elastic costants, the value of velocities in directions $\langle 100\rangle$,$\langle 110\rangle$ and $\langle 111\rangle$ are different. In particular, the degeneration in v_t cancels out in direction $\langle 110\rangle$[43].
The above description has been made for *bulk waves*, i.e., acoustic waves generated into the materials volume. We know that acoustic modes associated with an interface exists; Solving Christoffel equation, solutions associated with vibrational modes near the surface appear. These modes can be excited through *surface waves*, generally characterized by lower frequencies.
They are localized at the surface, so the vibrational amplitude decays away from the surface: they propagate along the surface within a thickness approximately equals their wavelength (*Rayleigh waves*), RAW. These modes can be originated from the surface reflections of bulk acoustic waves or from resonances of transverse bulk modes with. In the latter case we are talking about *Pseudo Surface Acoustic Waves*, PSAW.

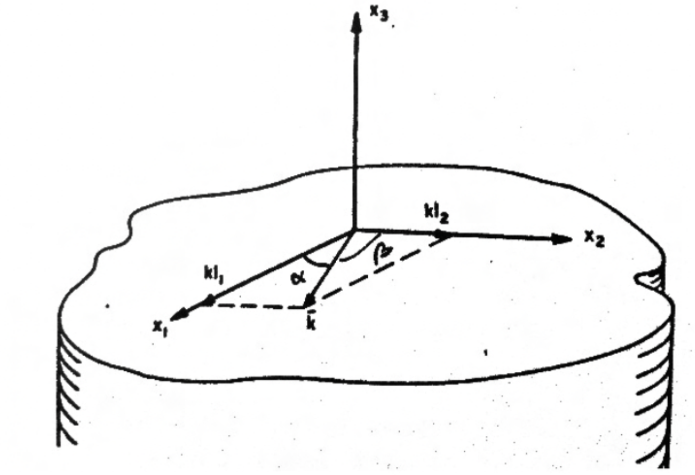

Figure 3.2: Reference geometry for surface dynamic problem. Fig.from[44]

Let's consider a solid with a free surface lying on the plane (x_1, x_2) (**Fig. 3.2**), axis x_3 perpendicular to and exiting the surface, a plane-wave propagating on the surface (i.e. $\mathbf{k} = k(l_1\hat{x_1} + l_2\hat{x_2})$) and a wavefront perpendicular to the plane. Moreover, its amplitude goes to 0 as $x_3 \to -\infty$. Therefore we are considering only surface waves that produce a ripple on the surface, i.e., transverse waves. Longitudinal surface waves (*Love waves*) are not considered in this work, because they do not interact with light through the "surface ripple mechanism" (see Section 3.2.3.

Thus, the wave equation for the i_{th} displacement's component become:

$$u_i = A_i e^{[ik\mu x_3]} e^{[ik(l_1 x_1 + l_2 x_2 - v_{ph} t)]} \tag{3.17}$$

We have introduced an extinction coefficient μ that describe the exponential amplitude decrease in direction $-\hat{x_3}$. Again, substituting this expression in the Christoffel equation (3.11), we obtain a polynomial equation depending both on μ and v_{ph}. Then we follow this algorithm:

- find the n complex solutions for μ as a function of v_{ph}, keeping only those that respect the condition of exponential decrease of the wave in depth: (n) solutions $\mu^{(n)}(v_{ph})$ are obtained.
- we write the wave function for the i_{th} displacement component as a linear combination of n plane waves, each characterized by an extinction coefficient $\mu^{(n)}(v_{ph})$.
- The components σ_{3j} have to be zero at the free surface; applying this boundary conditions:

$$\sigma_{3j}|_{x_3=0} = \frac{\partial u_k}{\partial x_l}|_{x_3=0} = 0 \tag{3.18}$$

we get a set of equations that allows us to find v_{ph} and the weight factors of the linear combination. Applying this method for an isotropic solid, we obtain an equation for v_{th} that give a non-close relation with the elastic constants, but it can be well approximated by an expression that involves the bulk transverse velocity v_t.

$$v_r = v_t \frac{0.87C_{11} + 2C_{12}}{C_{11} + 2C_{12}} \tag{3.19}$$

This velocity is called *Rayleigh velocity.* As seen, it is always lower than v_t and, consequently, than v_l. The displacement field associated is given by:

$$\begin{cases} u_1 = C[e^{ik\mu^{(3)}x_3} - Ae^{ik\mu^{(2)}x_3}]e^{ik(x_1 - c_R t)}, & (3.20a) \\ u_2 = 0, & (3.20b) \\ u_3 = -iC[1 - (c_R/c_l)^2]^{(}1/2)[e^{ik\mu^{(3)}x_3} - (1/A)e^{ik\mu^{(2)}x_3}]e^{ik(x_1 - c_R t)}. & (3.20c) \end{cases}$$

Eq. (3.20) tells us that a particle moves following an elliptic trajectory on a plane parallel to the wave direction. The amplitude of this trajectory tend to 0 exponentially for $x_3 \rightarrow -\infty$.

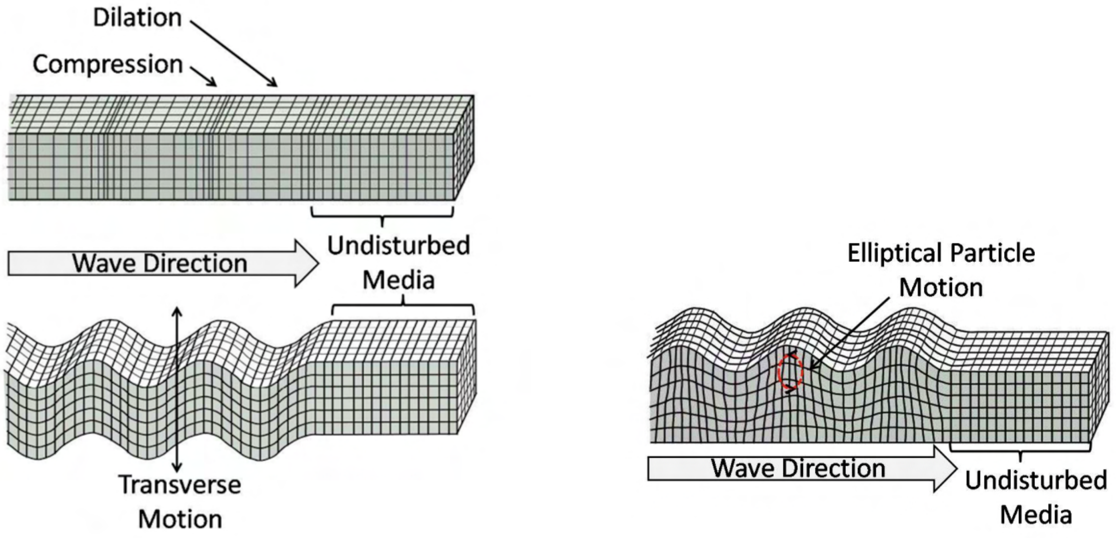
Dilation
Compression
Undisturbed Media
Wave Direction
Undisturbed Media
Transverse Motion
Elliptical Particle Motion
Wave Direction
Undisturbed Media

(a)

(b)

Figure 3.3: Acoustic Waves in solids: Longitudinal and transverse bulk waves(a), Rayleigh waves(b)[45]

3.2.2. Acoustic modes in a supported thin film

When we approach the study of SAW of a thin film on substrate, we have to keep in mind that, if we are looking for surface modes whose wavelength are comparable with the film thickness, the interaction of substrate surface waves and film SAWs is not negligible. In our analysis, we consider the substrate as semi-infinite medium; if the thickness of the film is greater than the characteristic extinction lenght of SAWs, we can consider the film a semi-infinite medium, too. Otherwise, the substrate interaction has to be taken into account, and its importance is grater, lower is the film thickness and lower is the wavevector inspected.

In order to solve the Christoffel's equation for the supported film, the boundary conditions, in addition to the absence of stresses on the free surface (3.18), have to ensure the continuity of the displacements and the stresses at the film/substrate interface.

The v_{ph} values that satisfy the equation are referred to:

- Rayleigh acoustic wave (RAW) with associated velocities v_R;
- Sezawa's modes (S(n)), i.e., guided SAWs confined in the film: if the transverse velocity of the substrate is much higher than the film's one, the film acoustic waves are completely reflected at the interface; thus, film can act as a wave-guide, and several modes (n) can propagate with $\mathrm{v}_{S(n)}$.

A particular case is a **slow film** on a **fast substrate**:

$$v_t^f < v_t^s \tag{3.21}$$

Both Sezawa's and Rayleigh's modes can be strongly influenced by the substrate. As said, if the wavenumber is small enough (and/or the film is thin enough) the coupling between the film's and substrate's SAWs appears. The film's velocities tend to the substrate's ones as its influence become more and more important. A dispersion reletion developes, as seen in (**Fig. 3.4**). The trend of velocities is:

$$\begin{cases} \lim\limits_{hk_{//}\to 0} v_R = v_R^s, & \text{(3.22a)} \\ \lim\limits_{hk_{//}\to \infty} v_R = v_R^f & \text{(3.22b)} \\ \lim\limits_{hk_{//}\to \infty} v_{S(n)} = v_t^f & \text{(3.22c)} \\ v_{S(n)} \leq v_t^s & \text{(3.22d)} \end{cases}$$

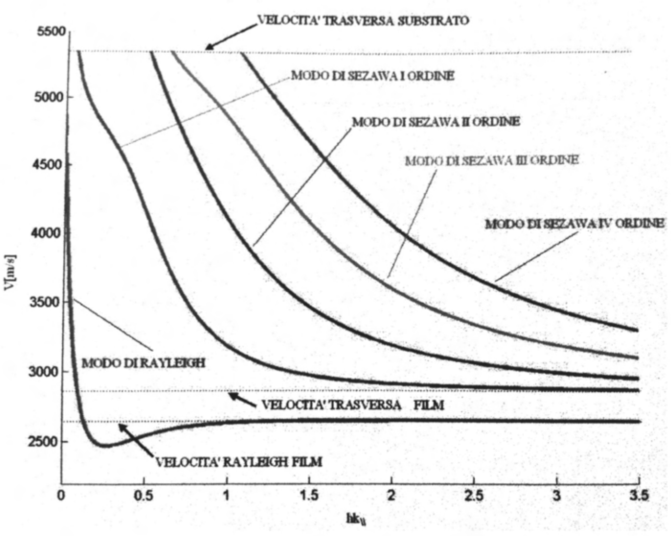

Figure 3.4: Dispersion relation of a W thin film on a Si substrate. In absissa, the product of the surface wavenumber $k_{//}$ and film thickness h; in ordinates, the velocities associated to Rayleigh and Sezawa modes. Figure from [44]

3.2.3. Light interaction with acoustic modes

The aim of Brillouin spectroscopy is the inspection of material's acoustic modes through the interaction with photons. The inelastic scattering of light by thermally generated elemental excitations, such as phonons or magnons gives us information about the elastic constants of the material. The incident light with wavevector, $\boldsymbol{k_i}$, and frequency, ω_i, is scattered to the $\boldsymbol{k_s}$, ω_s state either by absorbing (anti-Stokes process) or emitting (Stokes process) a phonon (i.e., a quantum of vibrational energy associated with a vibrational mode) with the wavevector and frequency of $\boldsymbol{q}$, ω_q, satisfying the momentum- and energy-conservation laws (**Fig. 3.5**). The scattering angle, ϕ, is defined as the angle between $\boldsymbol{k_i}$ and $\boldsymbol{k_s}$[46]. Looking at Fig. 3.5, the momentum conservation implies that:

$$\boldsymbol{k_s} - \boldsymbol{k_i} = \pm \boldsymbol{q} \tag{3.23}$$

Respectively for an anti-Stokes(+) and a Stokes(-) event. For a given wavenumber k, the ratio between energy of the phonon $E_{phonon}(k)$ and the photon's one $E_{photon}(k)$ is equal

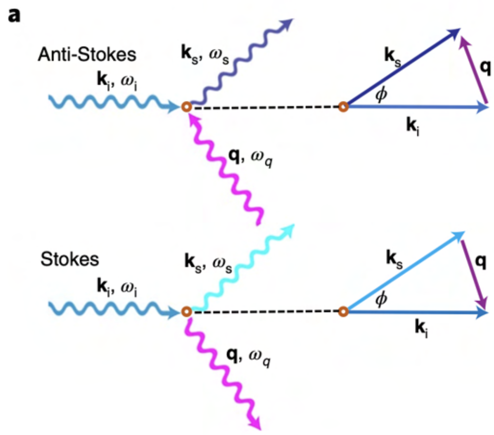
a
Anti-Stokes
$\mathbf{k}_i, \omega_i$
$\mathbf{k}_s, \omega_s$
$\mathbf{q}, \omega_q$
$\mathbf{k}_s$
$\mathbf{q}$
ϕ
$\mathbf{k}_i$
Stokes
$\mathbf{k}_i, \omega_i$
$\mathbf{k}_s, \omega_s$
$\mathbf{q}, \omega_q$
$\mathbf{k}_s$
$\mathbf{q}$
ϕ
$\mathbf{k}_i$

Figure 3.5: Interaction and momentum conservation in the laser light-phonon interaction. Figure from [46]

.

to the ratio of the vibrational mode's velocity and the light velocity.

$$\begin{cases} E_{phonon} = \hbar\omega = \hbar v_{acous} k, & (3.24a) \\ E_{photon} = \hbar v_{light} k & (3.24b) \\ \dfrac{E_{photon}}{E_{phonon}} = \dfrac{v_{light}}{v_{acous}} \sim 10^5 & (3.24c) \end{cases}$$

So,

$$(E_{phot})_{scat} = (E_{phot})_{in} \pm (E_{phonon}) = (E_{phot})_{inc} \times (1 \pm 10^{-5}) \tag{3.25}$$

The energy gained from or tranferred to the photon is very small compared to its initial energy. Therefore, we can assume no significant variation in its impinging and scattered wave number: $k_i \approx k_s$. The photon's angular frequency shift is given by:

$$\omega_s - \omega_i = \pm\omega_q(\boldsymbol{q}) \Rightarrow \omega_s \approx \omega_i \Rightarrow |\boldsymbol{k_i}| \approx |\boldsymbol{k_s}| = \frac{2\pi}{\lambda_0} \tag{3.26}$$

With λ_0 the laser light wavelength (532 nm if Ti:sapphire laser is used). If material is not opaque, the light can interact with bulk modes. Being n the material's refractive index, the bulk wavenumber inspected $|\boldsymbol{q}|$ is obtained combining equation (3.26) and

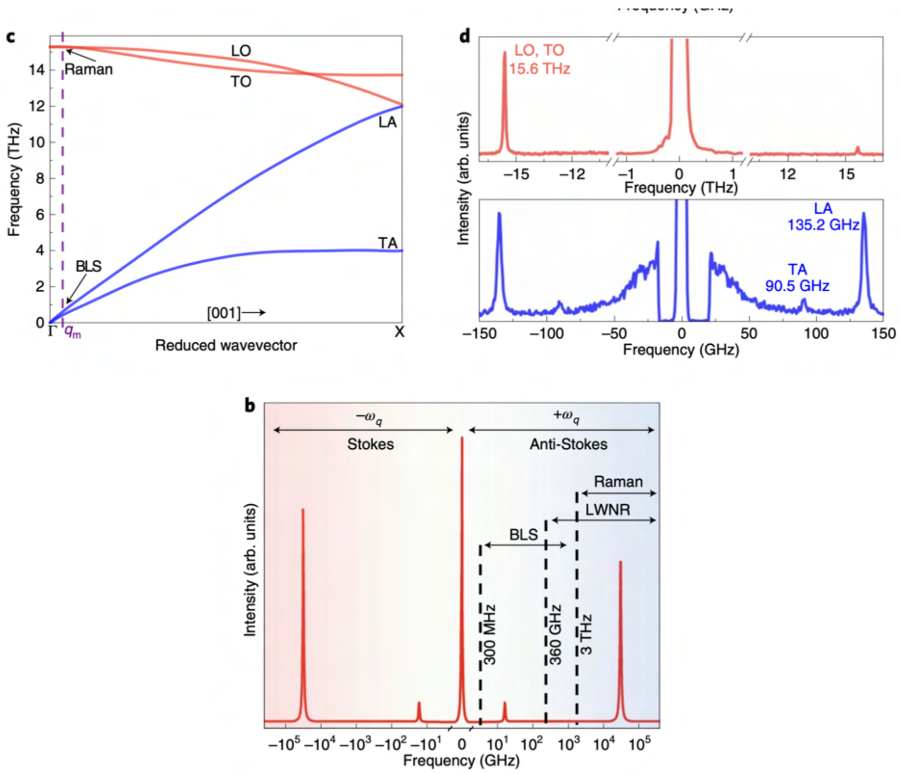

Figure 3.6: (b)Typical frequency's range for Raman, BLS and LWNR techniques. (c)Dispesion relation for a cubic crystal, showing longitudinal and tranverse modes in acoustic (blue) and optic (red) branches. (d) typical Raman (optical phonons, high frequency) and BLS (acoustic phonons, low frequency) spectra. Figures from [46]

.

(3.23) (Bragg's law):

$$|\boldsymbol{q}| = \frac{2\pi}{\lambda_{acoust}} = \frac{4\pi n}{\lambda_0}\sin(\frac{\phi}{2}) \tag{3.27}$$

Being $\Delta f = (\omega_s - \omega_i)/2\pi$ the light's frequency shift, bulk phonon velocity from the Brillouin peak shift is given by:

$$v_{acoust} = \frac{\lambda_0 \Delta f}{2n\sin(\phi/2)} \tag{3.28}$$

In **backscattering** configuration, the scattered light detected is the one parallel to the incident beam, i.e., $\phi = \pi$.

Light can interact with SAWs through the *Surface Ripple mechanism.* For opaque materials, this is the only type of interaction that can occur (**Fig. 3.6**). The SAWs wavevector $\boldsymbol{q}_{||}$ lies on the film surface, so light interacts only through its wavevector's parallel component, $\boldsymbol{k}_{||}$. Occurring at surface, this kind of interaction does not involve refraction[47]. Of course, $\boldsymbol{k}_{||}$ depends on the angle θ between $\boldsymbol{k}$ and the normal to the surface (**Fig. 3.7**).

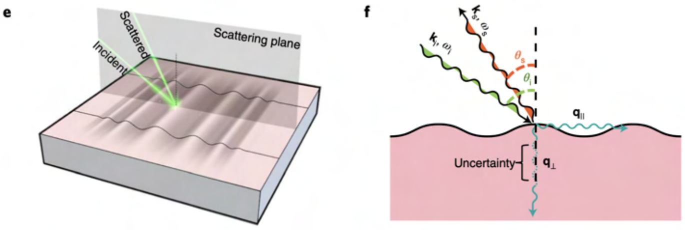

Figure 3.7: Surface ripple mechanism. Figures from [46]

.

Referring to (**Fig. 3.7**), the relations for SAWs interactions for the exact backscattering configuration ($\boldsymbol{k_s} = -\boldsymbol{k_i}$):

$$\left\{\begin{aligned} |\boldsymbol{k}_{||}| &= \frac{2\pi}{\lambda_0}\sin\theta && (3.29a)\\ (\boldsymbol{k_s} - \boldsymbol{k_i})_{||} &= \pm\boldsymbol{q}_{||} && (3.29b)\\ q = |\boldsymbol{q}_{||}| = 2|\boldsymbol{k}_{||}| &= 2\frac{2\pi}{\lambda_0}\sin\theta && (3.29c)\\ v_{acoust} &= \frac{\lambda_0 \Delta f}{2\sin\theta} && (3.29d) \end{aligned}\right.$$

Considering a semi-infinite elastically isotropic material, the scattering cross section for the Surface Ripple mechanism is proportional, according to the *fluctation dissipation theorem*[47], to the mean square displacement perpendicular to $q_{||}$ in the scattering plane[46][48], i.e.,

$$\frac{d^2\sigma}{d\Omega d\omega_s} \sim |u^z(0)|^2_{q_{||},\omega} \tag{3.30}$$

This term determines which phonon modes contribute to the light scattering. As it is seen, only those surface modes with a vibrational displacement perpendicular to $q_{||}$ in the plane of scattering appear in the BLS spectrum[46].

Another important aspect concerns the film-substrate interaction. As θ decreases, the inspected wavenumber $q_{||}$ decreases (3.29c) and the wavelength increases; thus the substrate interaction becomes more and more important. In order to draw the dispersion relation like the one seen in **Fig. 3.4**, we need to obtain the spectrum at different angles (i.e., at different $q_{||}$), register the position of the peaks (Rayleigh and/or Sezawa modes) and finally represent the trends of SAWs velocities as a function of θ.

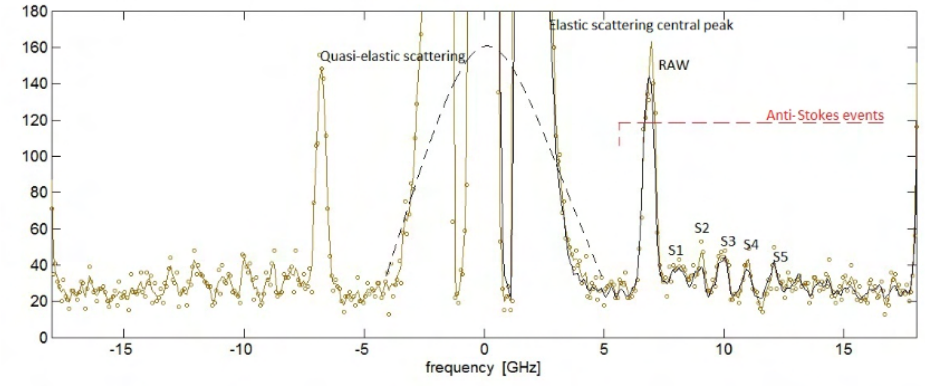

Figure 3.8: A typical Brillouin spectrum, showing peaks for different SAW's modes (Rayleigh and Sezawa). Figure from [44]

.

3.3. Wafer Curvature Technique

Wafer curvature techniques, as suggested by its name, involve the measurement of the substrate curvature through different methods[10][20]. This information is important because it allows us to calculate the stresses in the film and its linear thermal expansion coefficient (CTE). It is based on the Stoney Relation (derived in chapter 1),

$$\kappa = \frac{1-\nu_s}{E_s}\frac{6\sigma_f t_f}{t_s^2} \tag{3.31}$$

This technique is used both for residual stresses calculation, and for thermal-induced curvature(eq.(1.20)). Considering a tungsten thin film on a silicon substrate with properties described in table 3.1,

	Si$_{100}$	**W**
YoungModulusE (GPa)	180	400
Poisson Ratio ν	0.28	0.28
CTE(K^{-1})	$3.1{\times}10^{-6}$	$4.5{\times}10^{-6}$
Thickness(μm)	500	0.500

Table 3.1: Bulk properties of Si(s) and W(f).

The substrate curvature developed through a temperature increase of 200°C is (eq.(3.31)

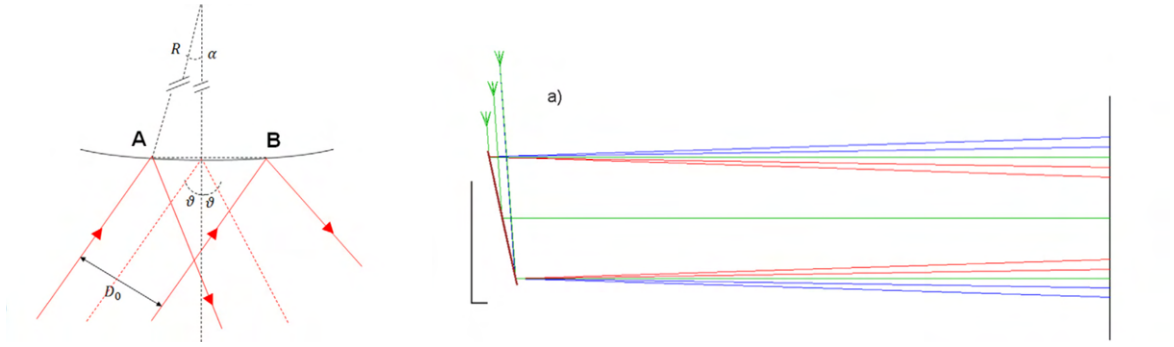

(a) (b)

Figure 3.9: Laser Beam Deflection technique. Figure (b) has been vertically dilated; the ortoghonal segments (at the left) are two unitary segments in the 2 directions. Figure from [49]

and eq.(1.20):

$$\kappa = (\frac{E_f}{E_s})(\frac{1-\nu_s}{1-\nu_f})\frac{6t_f}{t_s^2}(\alpha_s - \alpha_f)(\Delta T) = 1.5 \times 10^{-3} m^{-1} \tag{3.32}$$

It corresponds to a curvature radius of **661 m** and a stress σ_f=-156 MPa (compressive). With such small curvatures, the main issue is being able to measure them.
As discussed in section 4.2, the technique used in this work is called **Laser Beam Deflection**: it consists in sending parallel laser beams on the specimen's surface, and measure their deflection through a sensor placed at a certain distance from the sample(Fig.3.9).

If the film is perfectly flat, both impinging and reflected laser beams are parallel, thus the distance D_0 between the beams remains unperturbed. If a certain curvature is present, after reflections beams diverge or converge; after a certain distance, the laser's spot are collected through a sensor placed orthogonally to the beams. By simples geometric evidences, one can relate the specimen's curvature to the spot distance on the sensor, knowing the optical path and the system's configuration.
Of course, as said in section 1.1 some assumptions have to be made in order to relate the curvature to the stresses during thermal cycles:

- perfectly flat substrate
- uniform film thickness
- perfect substraste-film adhesion
- negligible variations of film's and substrate's Young Modulus, Poisson's Ratio and Thermal Expansion Coefficient CTE with temperature.

- Homogeneous temperature of the sample. At any instant, T assumes the same value all over the film's surface.

Heating the substrate, we can obtain a graph relating the curvature to the temperature. In we remain in elastic regime, the curvature should depend linearly from the temperature, so we should see two overlapping lines, one associated to heating, and the other one to cooling.
Unfortunately, often this is not the case, since several plastic or stress relaxation mechanisms can occur:

- If the biaxial film's stress σ_f exceeds the film's yield stress σ_y at a given temperature, the relation between curvature and temperature becomes more and more flat.
- if some initial residual stresses are present, several relaxation mechanism can occur, as the film is heated, such as creep, grain growth, atomic diffusion (that can induce hillock formation), and, if the stress exceeds the ultimate stress and the adhesion is not perfect, cracking and delamination.
- If the initial structure is metastable, such as an amorphous phase, relaxation mechanism related to densification can occur; then a temperature-enhanced microstructural reorganization occur, tensile stress develops in the film, and a strongly non-linear behaviour is observed.

To better understand the plastic flow's mechanisms, the strain rate should be taken into account; Fig 3.10 shows the deformation mechanism map associated with a thermal cycle for thin film Al. A deviation in linearity can be seen, as a consequence of thermal creep and dynamic recrystallization.

The imposed thermal strain is accomodated as elastic and plastic deformation. At all temperatures, the strain relationship is:

$$\epsilon_{thermal} + \epsilon_{elastic} + \epsilon_{plastic} \approx 0 \tag{3.33}$$

thus,

$$d\epsilon_{elastic} + d\epsilon_{plastic} = (\alpha_f - \alpha_s)dT \tag{3.34}$$

Please note that in relation (3.33) the elastic strain of the substrate has been neglected, being orders of magnitude lower than the elastic strain of the film (eq.(1.18)). This relation tells us that in a curve stress versus temperature, **provided there are no volume changes**, the slope can never exceed the value $[E_f/(1-\nu_f)]\Delta\alpha$. When the slope becomes smaller than the purely elastic one, we know that a plastic flow developes.

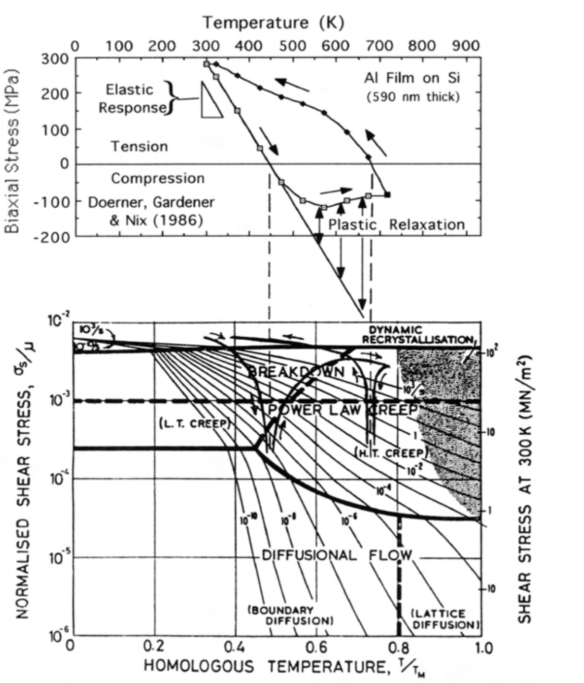

Figure 3.10: Stress-Temperature curve and Deformation Mechanism Map for thin Al on substrate[50]

On the other hand, if the slope exceeds this value, other mechanism involving a volume variation occur, such as densification.

3.3.1. CTE determination

Assuming, in first approximation, a purely elastic behaviour, we derive equation (1.20) with respect to T:

$$\frac{d\sigma_f}{dT} = \frac{E_f}{1-\nu_f}(\alpha_s - \alpha_f); \tag{3.35}$$

$$\alpha_f = \alpha_s - \frac{d\sigma_f}{dT}\frac{E_f}{1-\nu_f} \tag{3.36}$$

That, combined with eq.(3.32) becomes:

$$\alpha_f = \alpha_s - \frac{d\kappa}{dT}\frac{E_s}{E_f}\frac{1-\nu_f}{1-\nu_s}\frac{t_s^2}{6t_f} = \alpha_s - \frac{d\kappa}{dT}\frac{E_s'}{E_f'}\frac{t_s^2}{6t_f} \tag{3.37}$$

Referring again to equation (1.20), we note that when α_f is greater than α_s, stress assumes a negative sign, i.e., it is compressive. Similarly, curvature κ is assumed negative when the geometry with the film on top is concave and positive whet it is convex.

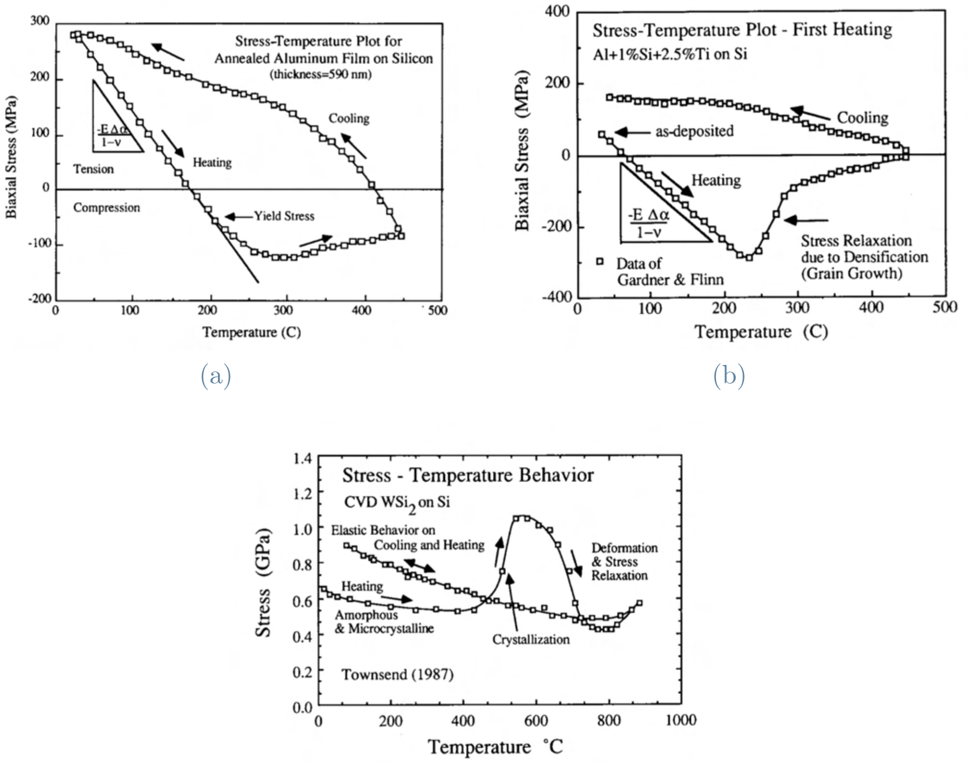

(a)

(b)

(c)

Figure 3.11: (a)Stress-temperature plot for an Al film on a Si substrate, (b) stress relaxation due to densification, (c) crystallization and following stress relaxation. Fig. from [10]

3.3.2. Residual stresses

If a residual stress σ_i is present the expression for the total stress becomes:

$$\sigma = \sigma_f(T) + \sigma_i \tag{3.38}$$

$$\sigma_f(T) = \sigma - \sigma_i = \frac{E_s}{1-\nu_s}\frac{t_s^2}{6t_f}(\kappa - \kappa_i) \tag{3.39}$$

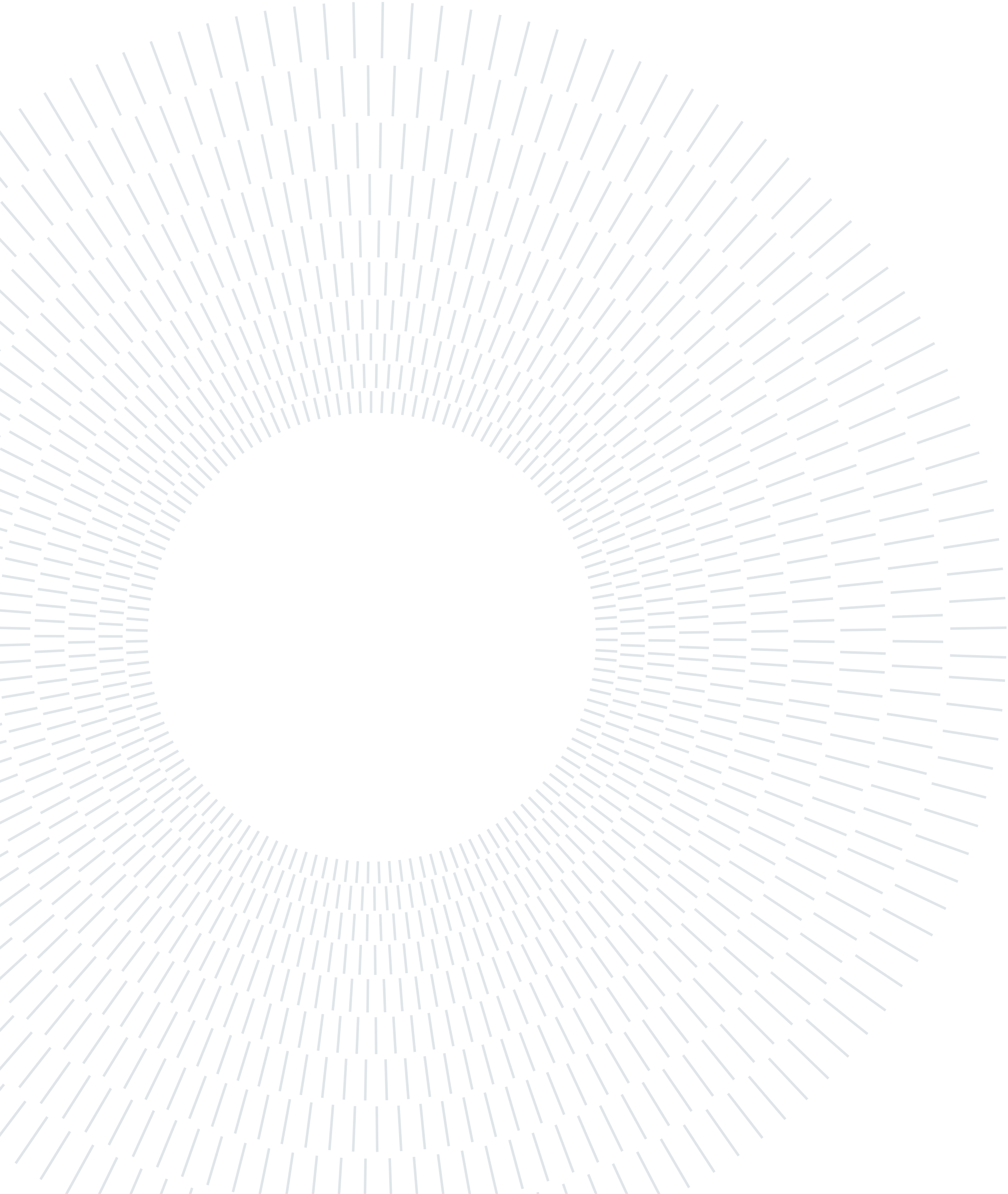

4 | Methodology and Experimental Setup

4.1. Brillouin Spectroscopy Experimental Setup

The experimental setup used for Brillouin spectrospcopy includes a laser, optical systems and collection lenses, a Fabry-Perot interferometer, a photomultiplier tube and a chain of electroning components, devoted to signal's processing and elaboration. Because the great majority of photon's emission belongs to elastic peak and inelastic scattering cross-section is very small, a high revelation efficiency is required. The **backscattering** configuration is used.

4.1.1. Laser and Optical Path

The laser utilized is a continuous-wave solid-state Ti:sapphire model from *Laser Quantum*, operating at a steady power output of 200mW. Emitting light at a wavelength of **532 nm**, it corresponds to an associated frequency of approximately 6×10^5 GHz, significantly surpassing the typical frequency range of acoustic waves (typically within the GHz scale). The laser's monochromaticity is rigorously maintained through electronic feedback mechanisms.

As seen in Fig 4.1 Light exits from the laser with a vertical polarization, than it is splitted through a *beam splitter* in a primary beam, directed to the sample, and an auxiliary beam, of much lower intesity, used for calibration and mirrors' alignment.

The mirror S deflects the light by 90°, sending it to the lens L1 that provides a focusing on the sample. After the interaction with the sample, backscattered light is defocused and arrives to the lens L2, where a focalization occur before the interaction with the interferometer.

The sample holder allows a manual selection of the incident angle. The associated uncertainty is not lower than 0.2°-0.3°.

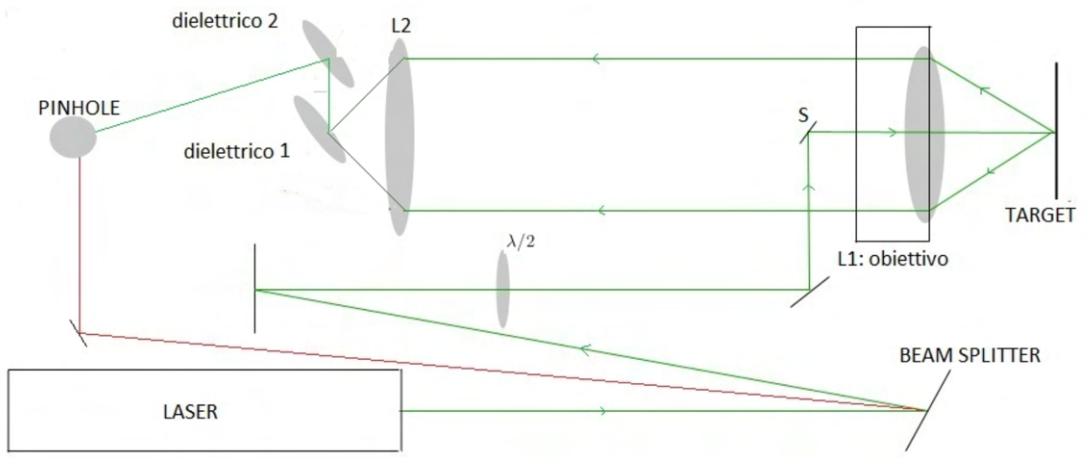

Figure 4.1: Scheme of optical path. Green line represents the principal beam, while red one the auxilary beam[44].

4.1.2. Fabry-Perot interferometer

Because the frequency's shifts are very small, without a *Tandem Multi-Pass* Fabry-Perot interferometer the peaks' resolution is almost impossible. In fact, it permits to precisely trasmit selected frequencies, descarding the others. This component is constituded by a pair semi-reflective flat mirrors (with a reflectivity, respectively, **R1** and **R2**) at a distance D. They create a resonant-cavity: the beams inside this cavity can constructively or distructively interact, depending on their optical path. After every complete travel, light acquires a phase difference respect to the previous ray equal to:

$$\phi = 2\pi\nu t_{rt} = 2\pi\nu\frac{2D}{c} = \frac{2\pi}{\lambda}2D \tag{4.1}$$

Being t_{rt} the travel time, ν the frequency, and λ the wavelength and c the speed of light in vacuum. Referring to figure 4.2, the constructive interference condition is $\phi = 2m\pi$, (considering for simplicity α=0), thus:

$$2D = m\lambda \tag{4.2}$$

Resonance occurs at wavelengths, with integer m, at which light exhibits constructive interference after one trip (2D). Those wavelength correspond to the maximum trasmissivity of the interferometer. The associated frequencies are:

$$\nu = m\frac{c}{2D} \tag{4.3}$$

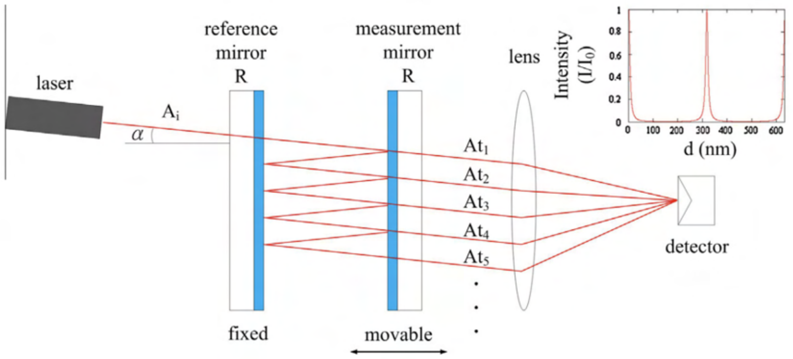

Figure 4.2: Fabry-Perot interferometer, Figure from [51]

The frequency difference between two trasmission peaks depends only on the distance between the mirrors. It is called **FSR**, Free Spectral Range:

$$FSR = \frac{c}{2D} \tag{4.4}$$

Ideally transmitted light is maximum if the resonance condition is valid, and zero if it is not. Instead, due to internal losses and a non-perfect reflectivity of the mirrors, which induces photon-decay[52]; hence, light bounces back and forth not an infinite number of times, but a finite number, and thus, out of resonance, destructive interference doesn't completely nullify the intensity. This behaviour modifies the frequencies' maximum and minimum intensities, but not their position. The frequency's spectrum reaches a minimum (but not zero) if $\phi = (2m+1)\pi$, and a maximum in resonance. The Airy Distribution (Fig.4.3) describes the frequency dependence of the trasmission intensity. The parameters involved are the mirrors' reflectivities (R) and phase shift ϕ:

$$\begin{cases} T_I = T^2 A(R,\phi) & \text{(4.5a)} \\ A(R,\phi) = \dfrac{1}{(1-R)^2 + 4R\sin^2(\phi/2)} & \text{(4.5b)} \end{cases}$$

Being T=(1-R) and T_I the ratio between the transmitted and the incident intensities I_t/I_i.

Two parameters describe the selectivity and resolving power of the Fabry-Perot: the *finesse* **F** and the *contrast* **C**, the first defined as the ration between the FSR and the width of the peaks (FWHM), the second the ratio between the maximum and the minimum of

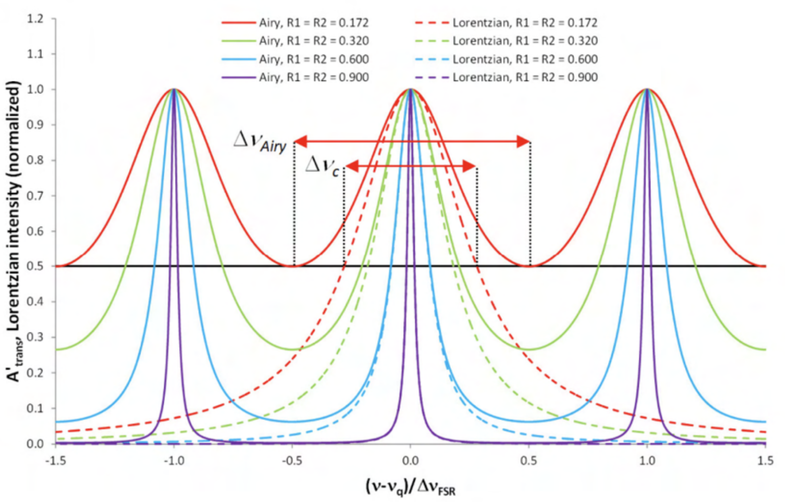

Figure 4.3: Airy distribution compared to Lorenzian distribution for different values of R1 and R2, Figure from [52]

the Airy's function, both increasing with the mirrors' reflectivity. If R_1=R_2=R:

$$\begin{cases} F = \dfrac{FSR}{FWHM} = \dfrac{4R}{(1-R^2)} & (4.6a) \\ C = \dfrac{1+R^2}{1-R^2} & (4.6b) \end{cases}$$

In our setup, F∼100. Once selected the distance between the mirrors, D, FSR is defined, hence the maximum frequency shift is set. Decreasing D, wee can investigate higher frequency shifts, but the resolution near the central elastic peak is lower. Through piezoelectric crystals, the imposed distance D is varied step by step of a quantity δD, such that $\|\delta D\| < \lambda/2 << D$. The fixed mechanical dimension, D, measures in the range of millimeters, whereas $\lambda/2$ spans hundreds of nanometers. Therefore, it is possible to select all frequencies inside the FSR without varying it. In fact $c/2D \sim c/(2(D + \delta D))$.

If a beam passes n times through a FB interferometer (*multi-pass)*, the contrast and finesse increase:

$$C_n = [\frac{1+R^2}{1-R^2}]^n \tag{4.7}$$

but the signal degrades. Moreover, several spurious peaks can develop[44]. Sandercock, in 1980, proposed the multi-pass tandem configuration, in which light pass several time through a pair of FB interferometers in series, mounted on the same movable support so that the ratio of the mirror pair distances is unchanged. This configuration, used in this work, proved to be the most sensitive.

4.1.3. Measurement Error

Several measures errors' sources are present:

- uncertainty in the incident angle θ_i, determined by the accuracy in determination of the angle 0, estimated to be 0.2°.
- uncertainty related to the finite opening of the collecting lens. Ideally, if perfect backscattering exist, only those photon with $\mathbf{k}_i = \mathbf{k}_s$ are selected. In contrast, due to the finite opening of the lens, all photons owning a wavevector falling into the aperture cone can be send to the interferometer, widening the scattring Bragg peak.
- uncertainty on the scattering angle θ_s. If backscattering configuration is non-perfect, beam and simmetry axis of collecting cone are not perfectly aligned.

Calling σ_ν^2 the variance associated with the widening in frequency shift peaks and σ_θ^2 the one relative to the incidence angle, from eq.(3.29c), the variance of the inspected wavenumber $q_{||}$ is:

$$\sigma_{q_{||}}^2 = (\frac{\partial q_{||}}{\partial \theta})^2 \sigma_\theta^2 = (\frac{q_{||}}{\tan\theta})^2 \sigma_\theta^2 \tag{4.8}$$

Then, being the SAW velocity $v_{saw} = 2\pi\nu/q_{||}$, the total uncertainty σ_v is:

$$\sigma_v^2 = (\frac{\partial v}{\partial \nu})^2 \sigma_\nu^2 + (\frac{\partial v}{\partial q_{||}})^2 \sigma_{q_{||}}^2 = \frac{1}{q_{||}^2}\sigma_\nu^2 + \frac{\nu^2}{q_{||}^2(\tan\theta)^2}\sigma_\theta^2 \tag{4.9}$$

At the end of the measurements, performed at a discrete set of incidence angles, we have $l \times j$ values of velocities $v_m(l,j)$, related to the j-th mode and the l-th wavevector (i.e., the l-th angle), with corresponding variances $\sigma_{v(l,j)}^2$. Deduct the elastic constants C_{11} and C_{44} and their error bars from measured velocities is not an easy task, since they are related through the Christoffel equation (3.11), which is not in a closed form.

The strategy adopted is to construct a mesh of values C_{11} and C_{44} and calculate the velocities $v_c(C_{11}, C_{44}|l,j)$ with a repetitive procedure at each node. Then, for each pair of values (C_{11}, C_{44}) we calculate the *least square estimator* by summing the square deviations corresponding to all different modes and angles, weighted on the variance of the measured velocity:

$$LS(C_{11}, C_{44}) = \sum_{j,l} \frac{[v_c(C_{11}, C_{44}|j,l) - v_m(j,l)]^2}{\sigma_{v_m}(j,l)^2} \tag{4.10}$$

The most probable values for the elastic constants are those who minimize the LS estimator given by the equation (4.10). In the space (C_{11}, C_{44}) we draw the level curves linked to the different values of LS. In order to estimate the errors bars, we must rely on the *estimation theory*: using the Fisher distribution, the level of the maximum likelihood estimator (MLE) is obtained, normalized to its minimum, corresponding to a predetermined level of confidence. So, we associate one of the level curve to the perimeter of a confidence region, within which the parameters have a probability equal to the confidence level chosen of being the right ones.

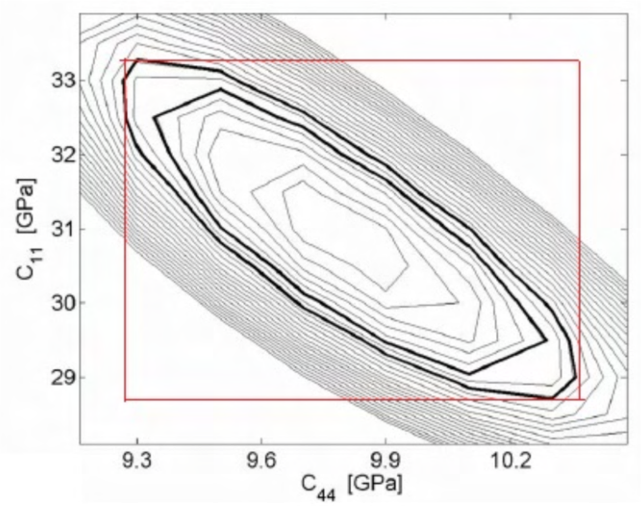

Figure 4.4: LS level curves: the thicker curves indentify regions relative to a 68% and 90% confidence level (black curves)[44]

4.2. Stoney's experimental setup

The Wafer Curvature technique's apparatus consists of laser optics, a vacuum chamber, and a CMOS sensor used to measure the position of the laser beam.

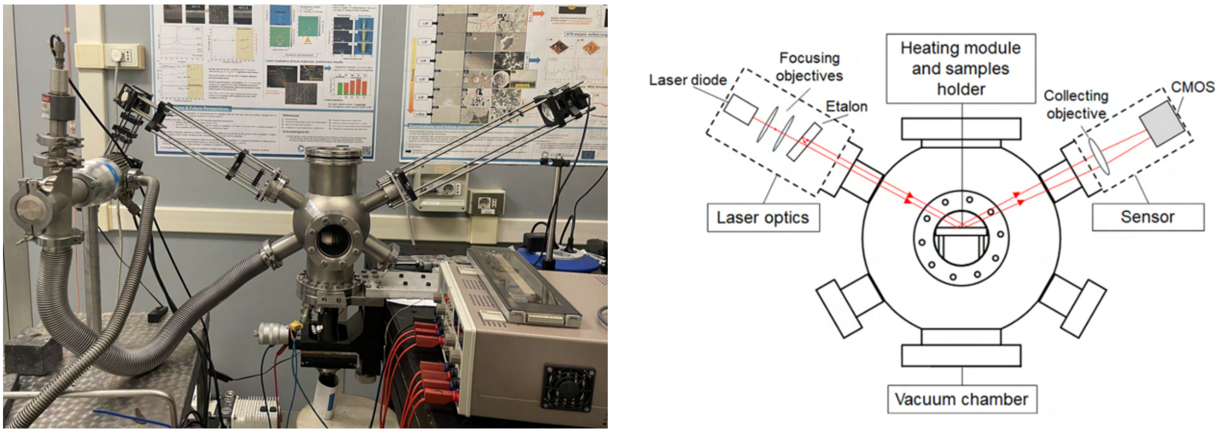
Laser diode
Focusing objectives
Etalon
Heating module and samples holder
Collecting objective
CMOS
Laser optics
Sensor
Vacuum chamber

(a) (b)

Figure 4.5: Experimental apparatus, (b) from [38]

4.2.1. Laser and Optical Path

The laser beam array is generated by combining a laser diode with an output of approximately 5 mW and a wavelength of 630 nm (near the CMOS maximum quantum efficiency), along with a pair of etalons. The first etalon multiplies the laser beam, producing three aligned beams in the first direction direction, while the second etalon, positioned at a 45° angle relative to the first, replicates the 1D array in the perpendicular direction, resulting in a 2D array of 9 parallel laser beams (3 ×3). In our setup we select only the beams

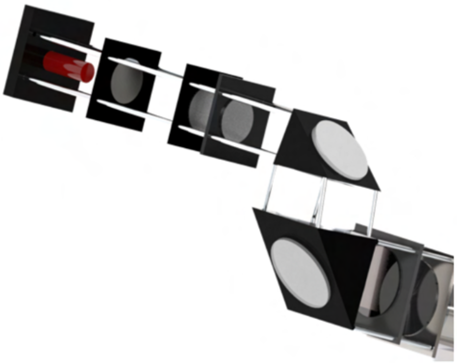

Figure 4.6: Laser and etalons[53]

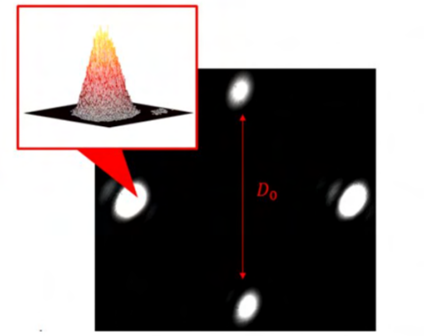

Figure 4.7: Spots on the sensor. Intensity profile can be seen.[53]

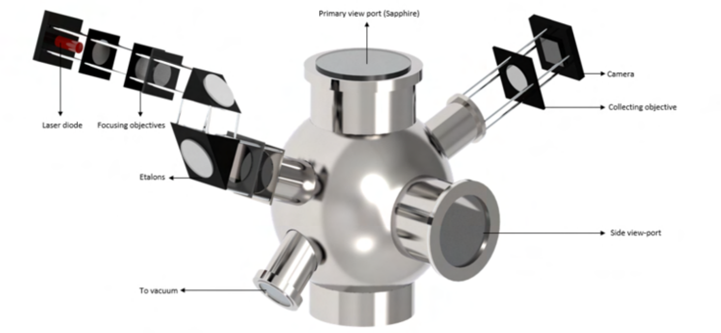

Figure 4.8: Vacuum chamber and optical system[53]

at the edges of the 2D array (2x2), spaced evenly at 1 cm intervals, covering a total measurement area of 1 × 1 cm^2. The array strikes the sample surface at a 60° angle of incidence at its center, and the measurement position remains constant throughout the entire measurement process. The reflected beams are captured by the CMOS camera with the aid of a collecting lens.

4.2.2. CMOS

The camera is has a 1.3 Megapixel sensor with a 1024×1248 pixel digital image and a physical dimension of 6.65×5.32mm^2. This small dimensions make a collective lens necessary, to ensure that the beams impinge on the sensor. The acquisition rate is 10 fps. The position of the beams' spot on the sensor is assessed through the determination on the spot's centroid of intensity, weighting the intensity of each pixel in the irradiation area over the total irradiated pixels[49]. The presence of an array of spots permits to associate the curvature to the position of the spots relative to each others on the sensor, independent of the rigid position of the array as a whole.

The single spots' positions is subjected to fluctuations, primarily due to the vacuum system; the array gives the possibility to work on the relative positions of the spots.

4.2.3. Vacuum Chamber, Power Supply, Heater and Thermocouples

The spherical vacuum chamber, measuring 300mm in diameter, is equipped with two 2" viewport flanges positioned at a 60° orientation for the entry and exit of laser beams. Additionally, there are two symmetrical flanges that allow for connections to the vacuum system and the introduction of gases, enabling precise control over the chamber's atmosphere for specialized treatments. As seen in Fig.4.8, the primary view port is made of sapphire; due to its transparency to infrared radiation, is not likely to break due to thermal stresses.

The vacuum system is constituted by a coupled rotary and turbomolecular pumps; it guarantees a pressure of 2-5$\times 10^{-6}$ mbar to prevent oxidation.

The heating module consists of a power supply constituted by four modules; each module can provide a power of 96 W, for a total 384 W. Two modules in series with a corrent of 3A and a total voltage of 64V have been used, reaching a maximum heating rate of 2°C/s. The cooling rate is dictated by the radiative thermal conduction, and is much slower than the heating one.

The power heats up a ceramic heating plate through Joule effect. Alumina's plate has been chosen for its low thermal expansion coefficient and high temperature homogeneity.

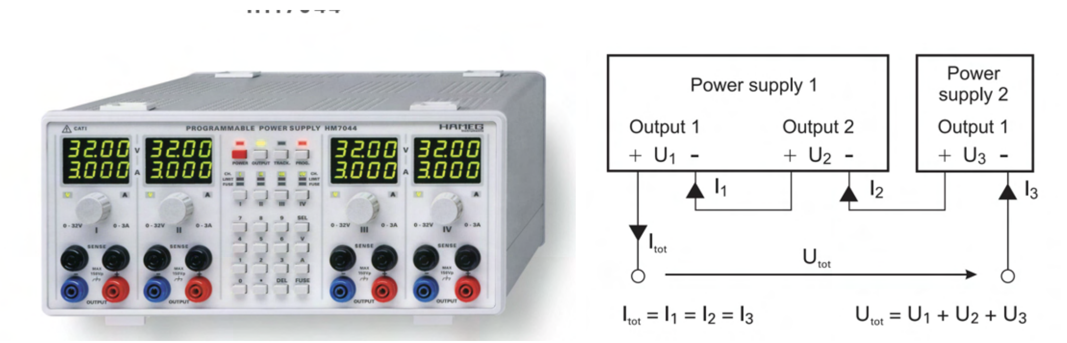

(a) (b)

Figure 4.9: (a)Programmable power supply, (b)Series-modules configuration, from [54]

4.2.4. Acquisition and Elaboration Software

The thermocouple, positioned under the sample, in a dedicated hole (type K) is linked to a Data Acquisition system (DAQ device), enabling a seamless and automated cycle of temperature measurements carried out using a LabVIEW Virtual Interface. This software acquires both temperatures and frames, simultaneously.

This ensures that the centroid positions of each spot are automatically coordinated with temperature data.
Temperature is measured every 0.5s. A MATLAB® code for centroids' determination and distances between spots as a function of temperature has been improved. Another script is used for curvature determination and CTE, knowing the system's geometry and optical components' features, as well as film's and substrate's properties.

4.2.5. Sensitivity Analysis and Measurement Errors

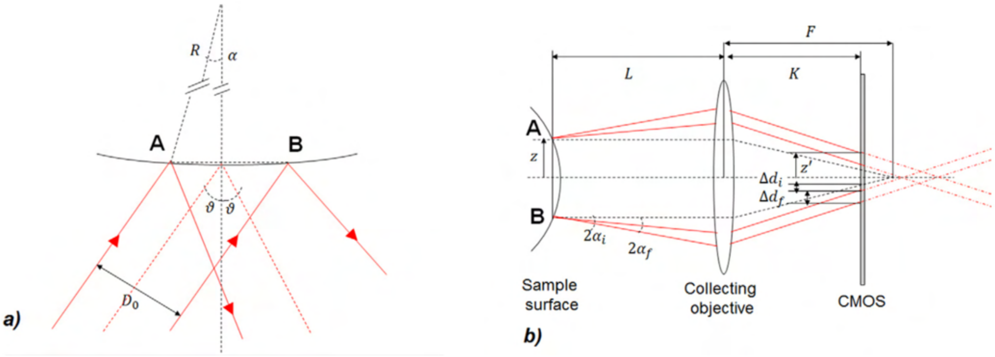

(a) (b)

Figure 4.10: (a)Parallel beams deflection on a curved sample, (b)optical path seen from the rays point of view [49]

Referring to figure Fig4.10a, being θ the angle between the entry and exit laser beam with the vertical (60°), R the curvature radius, α the deviation angle of the beam with respect to the optical axis of the system and D_0 the distance between inlet parallel; The simple relation between α and θ is:

$$\sin\alpha = \frac{D_0}{2R\cos\theta} \tag{4.11}$$

At first, let consider the system without the lens, and a distance A between the sample and the sensor. Since $D_0 = 1cm$, $R > 10m$, $\alpha < 10^{-3}$, paraxial approximation can be used; $\sin\alpha \sim \tan\alpha \sim \alpha$. If the sample is flat (R $\rightarrow \infty$, $\alpha \rightarrow 0$) the parallel beams exit and arrive on the sensor at an unperturbed distance D_0; if a certain curvature exist, the distance d between the spots on the CMOS is:

$$d = D_0 + 2A\tan 2\alpha \approx D_0 + 2A\sin 2\alpha = D_0(1 + \frac{4A}{2R\cos\theta}) \tag{4.12}$$

The system is well characterized by the relative sensitivity, i.e., the variation of the spots' distance on the sensor with respect to the curvature variation, weighted on the unperturbed spot distance D_0.

$$s_r = \frac{d(d/D_0)}{d(1/R)} = \frac{4A}{2\cos\theta} \tag{4.13}$$

Then, relative sensitivity increases both with increasing arm length A and angle θ. As said, the physical dimensions of the sensor dictate a limit for A. A converging lens is then necessary in order to being able to perform the measure with a high sensitivity.
Looking at figure Fig4.10b, a collective lens with focal length F is placed at a distance L from the sample. Being K the distance between the lens and CMOS, A=L+K. The distance z' between a spot and the optical axis on the sensor is linked to the distance z on the sample ($=D_0/2$, constant) and the angle α by the relation:

$$z' = (1 - \frac{K}{F})z + 2\alpha[L(1 - \frac{K}{F}) + K] \tag{4.14}$$

Thin lens approximation has been used ([49]).
As seen, if K>F, i.e., the CMOS is placed after the focal point, z' is negative.
If the sample is flat, the distance between the spots on the sensor is:

$$d_\infty = (1 - K/F)D_0 \tag{4.15}$$

and the distance variation $d - d_\infty = \Delta d$ is:

$$\Delta d = 2 \times z'(2\alpha) \tag{4.16}$$

Combined eq.4.16 and eq.4.11 we can obtain a relation between the spot's distance variation on the sensor and the sample curvature:

$$\frac{\Delta d}{D_0} = \frac{1}{R} \times \frac{2[L(1 - K/F) + K]}{\cos\theta} \tag{4.17}$$

The relative sensitivity is given by (θ=60°):

$$\frac{1}{d_\infty}\frac{d(\Delta d)}{d(1/R)} = \frac{D_0}{d_\infty} \times 4[L(1 - K/F) + K] = 4\frac{F}{F - K}[L(1 - K/F) + K] \tag{4.18}$$

The sensitivity does not depend on D_0 and curvature, but only on geometrical features. As seen in graph 4.11, when K approach F, relative sensitivity tends to ∞, because d_∞ tends to zero.

As seen in Fig. 4.11, if K>F sensitivity rapidly goes to 0, then a little variation in the lens position when the focal point is before the sensor causes a strong variation in sensitivity.

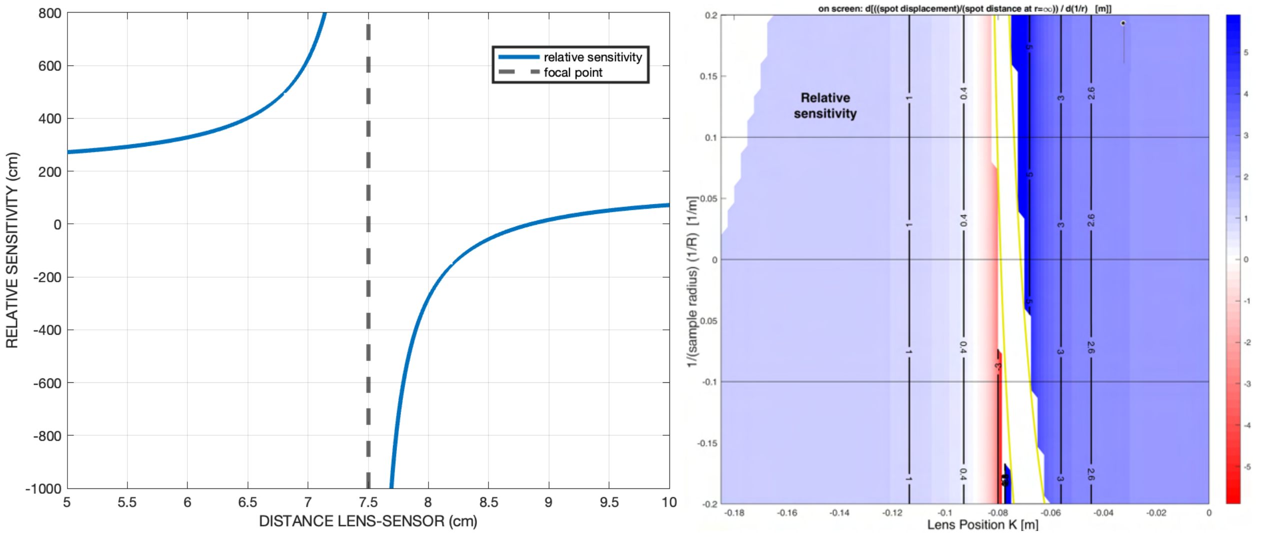

(a) (b)

Figure 4.11: (a)Sensitivity variation with K. The dotted line represent the focus position. A=58cm and F=7.5cm, (b) Relative sensitivity level curves. The white strip represent the "forbidden region": here spots are not resolvable. The optical axis goes from the sample to the sensor, so the distane lens-sensor K is assumed negative.

The configuration K<F is selected, because it guarantees higher room for movement, maintaining an higher sensitivity. Additionally, the focal position cannot be too close to the sensor because the finite size of the spots prevents them from being distinguished if they are in very close proximity to each other. A map with the level curves of the sensitivity, as a function of both curvature and lens position is useful to identify the forbidden region. The arm legth A is 58cm, F is 7.5cm and the selected K has been varied from 8.5cm to is 6.2cm. Hence, the relative senitivity went from 57cm to **357cm**.

The measure accuracy strongly depend on the background noise. Measuring the spot's position on a non-heated sample, we should see no variation in spots' distances' values. Instead, we see an oscillation δd of about 0.5-0.8 pixels. The average distance between two spots is $\sim$ 200 px, so the relative uncertainty is $\delta d/d_\infty \sim 0.004$. Being the relative sensitivity s_{rel}=3.57m, the uncertainty associated to the curvature is:

$$\delta(\frac{1}{R}) = \frac{1}{s_{rel}}\frac{\delta d}{d_\infty} \sim 1.1 \times 10^{-3} m^{-1} \tag{4.19}$$

If the curvature radius is 100m, the relative uncertainty:

$$\frac{\delta(1/R)}{1/R} = 0.1 \tag{4.20}$$

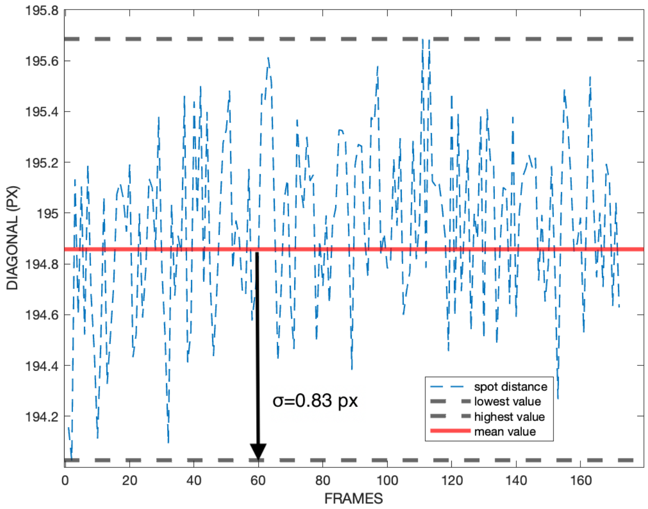

Figure 4.12: Oscillation of the distance between two spots. The dotted line represent the distance d, the arrow represent the variance. The term 'diagonal' refers to the distance between spots positioned at opposite edges of the array.

The uncertainty on CTE values α_f depends on the uncertainty of the measured elastic constants and the confidence interval of the fit parameter of $d\kappa/dT$, i.e., the slope on the curvature-temperature plot.

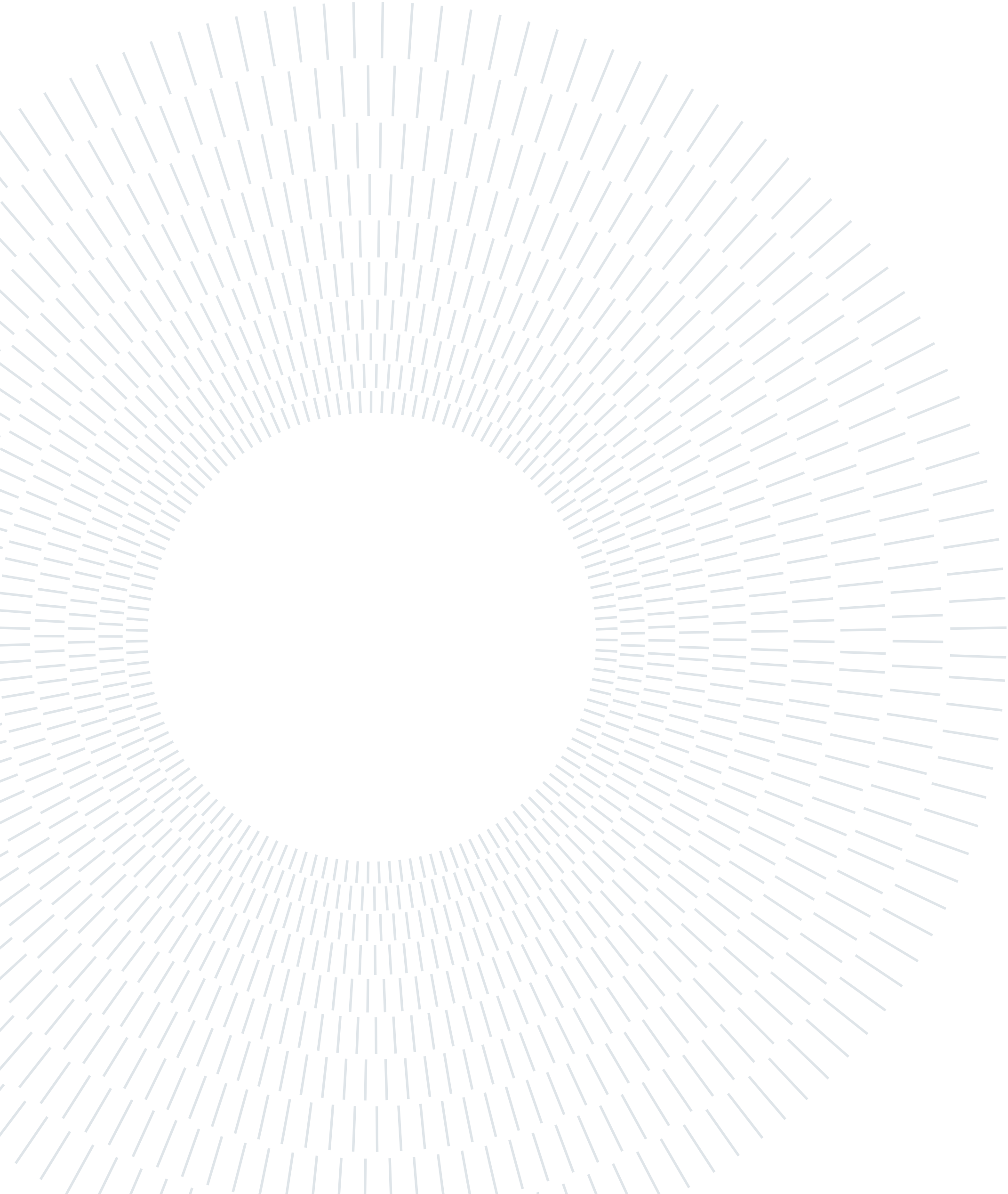

5 | Results and Discussion

5.1. System optimization and Measurement procedure

5.1.1. Introduction

The experimental work encompassed two main components: the optimization of the setup and the analysis of the samples. The samples analyzed in this work have been entirely produced at NanoLab @Polimi. Materials investigated are nanocrystalline and amorphous W and WN thin films, pure aluminum thin films and Y_2O_3 thin film, all deposited on mono or bi-lapped monocrystalline Si, with thickness respectively of 500 and 380±10 μm with the following propertie riassumed in table 3.1.

5.1.2. Wafer Curvature Technique optimization

Several problems have been encountered during Stoney's analysis; Therefore, optimization of the measurement system was necessary in the process. The changes made to the system included:

1. **Modification of optical path**, consisting of the addition of two degrees of freedom in the laser's arm, in order to improve the maneuverability of beam direction and focus. In fact, the possibility to select the incident point of the laser beam on the first etalon, permits to control the positions of the spots on the sample, without moving too much the etalons' mirrors, that would add a great complication.

2. **Electrical insulation** of heater and thermocouples cables. Several short circuits due to calbles' contact with each other and with the grounded aluminum vaccum chamber have compromised some measurements. Electrical insulation with alumina beads has been performed.

3. **Heating modules' connection** from parallel to series configuration. Temperatures up to 650°C have been reached with just two modules lit up, much higher

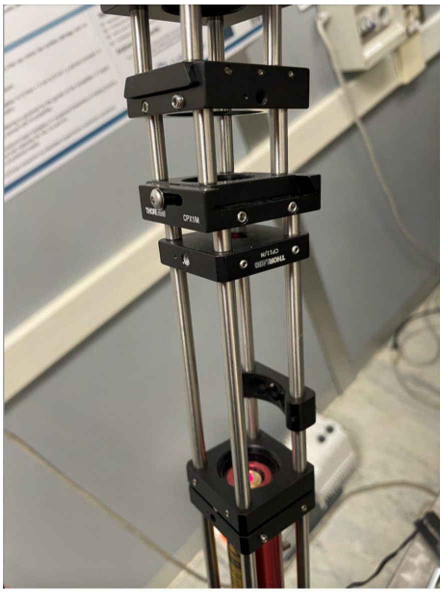

Figure 5.1: Laser's arm with movable components: they allow transverse movements

than the temperatures reched in previous works[53].

4. **Drastic improvement of system's relative sensitivity**, by moving the collecting lens according to the relative sensitivity map (Fig.5.2), as discussed in section 4.2.5.

   The absolute spot displacement is related to the absolute sensitivity;As seen in Fig. 5.3, it increases as relative sensitivity decreases. The lens position chosen is really close to the white band, within which measures are impracticable (see Fig.**??**, so the relative sensitivity is the highest achievable.

5. **Temperature homogeneity assessment**: in order to evaluate the temperature uniformity of the sample and the support, a pyrometer has been used. Once the temperature has been stabilized, it has been measured on different surface's points, both on the film and on the support, as seen in Fig.5.4. A good homogeneity has been observed, with a maximum variation less than 1%. On the support, of course, the temperature is higher, but it is not uniform: away from the alumina plate the temperature is lower. A good procedure consist in positioning the sample over the alumina plate, to have the maximum coherence between the temperature measured through the thermocouple and the sample's one.

6. **Software optimization**: The MATLAB code has undergone optimization to enhance speed and efficiency in analyzing frames. Additionally, I've developed a code to visualize overlapping frames and track the time-dependent positions of centroids.

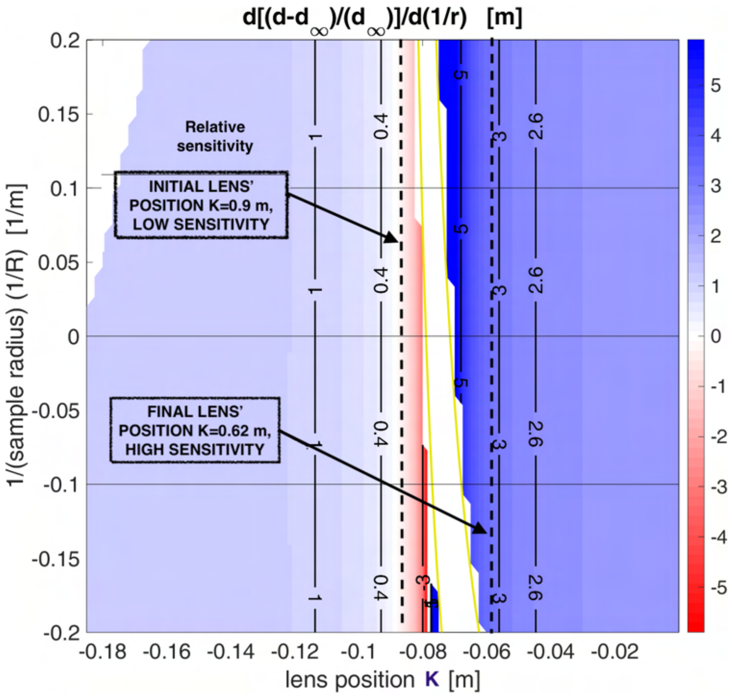

Figure 5.2: Relative sensitivity $\frac{1}{d_\infty}\frac{d(\Delta d)}{d(1/R)}$

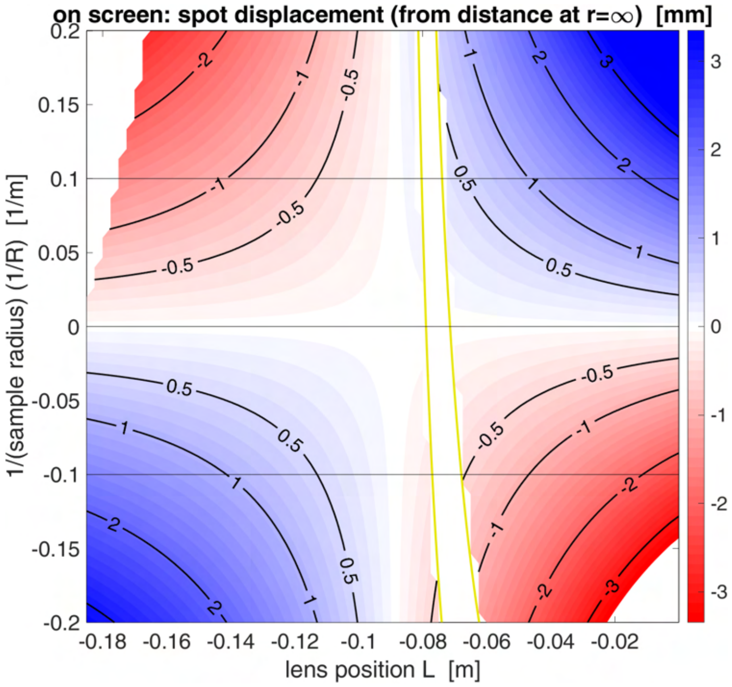

Figure 5.3: Level curves of spots' displacements on the sensor $d - d_\infty$.

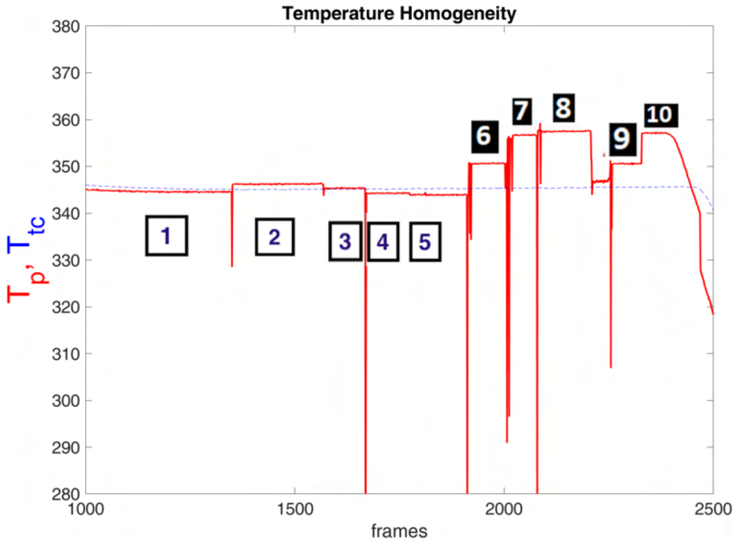

(a)

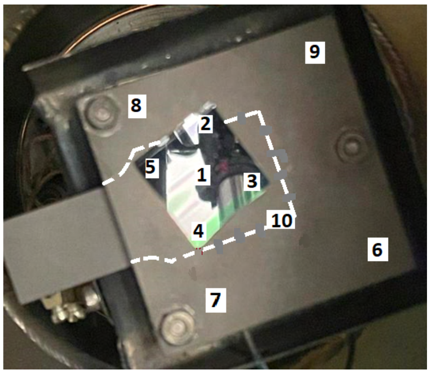

(b)

Figure 5.4: (a)Temperature registered with thermocamera on different points(red line). Points 1-5 refers to the sample's surface, while points 6-9 to the support, as seen in image, as indicated in (b). At steady state, the temperature measured with TCK is lower than that of the pyrometer, since it is positioned right above the alumina plate. White dotted line in (b) shows the position of the alumina plate

The utilization of this code significantly aided in comprehending the dynamics and characteristics of the spots' movements. In Appendix A, the code developed and their output are shown.

5.1.3. Measurement Procedure

Following the deposition process, the films were examined using a Scanning Electron Microscope (SEM), providing valuable information regarding their thickness and microstructure. Additionally, some of these films were subjected to weight measurements to determine their density.
Then, the following procedure has been followed:

- **Brillouin spectroscopy**: The procedure was carried out on specimens of known density, which is essential for calculating the elastic constants from the measured velocities. In cases where the samples lacked this density information, elastic constants were either sourced from existing literature or deduced from correlations with the microstructure of the films. After acquiring spectral data from five different angles and identifying the relevant SAW modes, the velocities, along with their associated uncertainties, were recorded. Subsequently, the least squares method outlined in section 4.1.2 was employed for further analysis. When determining the elastic constants, a 68% confidence region was taken into account. The Young's modulus and Poisson's ratio were then derived from these elastic constants, and their respective uncertainties were assessed using the error propagation equation.

- **Residual stresses determination before thermal cycles**: some provided samples were in a non-annealed state, which meant they retained residual stresses. These residual stresses were quantified using the wafer-curvature technique. For bilapped samples, the difference in curvature between sides A and B allowed for the measurement of residual stresses without the need for comparison to a bare Si sample, as described in equation (4.14). In the case of monolapped samples, the film's curvature was compared to that of a flat, bare Si sample($R \to \infty$).

- **Thermal cycling and CTE determination by Substrate Curvature Technique**: The samples were placed inside the vacuum chamber, and a series of thermal cycles were conducted. During these cycles, data were collected, including the position of the spots' barycenters over time, as well as plots depicting the relationship between curvature and temperature, and stress and temperature. The Young Modulus and Poisson Ratio obtain by Brillouin spectroscopy provide essential informations for CTE_{film} calculation. The use of multiple thermal cycles was a deliberate choice aimed at improving the accuracy of determining the slope between curvature and temperature, as well as enhancing our ability to understand microstructural changes by observing variations in the linearity of the curvature, as discussed in **Chapter 3**. First cycles were conducted at relatively low temperature, to observe the "elastic" behaviour of the film and prevent any microstructural change. Then, higher temperatures were reached to observe plastic flow or stress relaxations.

- **SEM analysis and residual stress' measurement after heating**: Following each thermal cycle, residual stresses were assessed to understand the impact of temperature changes on their reduction. For select critical samples, specifically WN-40 and Al-19, a cross-sectional analysis was conducted using SEM to investigate detachment and the evolution of the microstructure.

5.2. Samples

The table5.1 shows the list of measured samples and their properties.

Samples

	Material	Dep. technique	Microstructure	T_f (nm)	ρ_f (g/cm^3)
Al-19-2	Al	DC	PC	750	2.7
Al-26-2	Al	HP	PC	800	2.5
Al-27-2	Al	HP	PC	800	2.6
Y134	Y_2O_3	PLD	NC	5000	5
W-133	W	HP	DPCG (α-W)	416	19.3[12]
W-137	W	HP	DPCG (α-W)	367	16.7
W-140	W	HP	DPCG (α-W)	454	17.2
WFW-1004	W	PLD	A	800	11
WN-19	WN	HP	NC	320	18.8
WN-21	WN	HP	NC	330	20.3
WN-39	WN	HP	NC	333	17.9
WN-40	WN	HP	UNC	238	$<$17

Table 5.1: Samples used in this work: the bold values of densities are those calculated, the others are extrapolated from previous works. **PC**=polycristalline; **NC**=nanocrystalline; **DPCG**=densely packed columnar grains; **A**=amorphous; **UNC**=ultra-nano-crystalline; **HP**=HiPIMS; **PLD**=Pulsed Laser Deposition

5.3. Experimental results

5.3.1. Aluminum

Aluminum Sample (**Al-19**, **Al-26**,**Al-27**) were deposited with HiPIMS (Al-26, Al-27) and DC magnetron sputtering (Al-19) on a 500μm Si substrate. In Fig.5.5 we can see the microstructure (planar view and cross section) of the as-deposited samples. We can observe a non-columnar and equiaxial-structure, with a grain dimension not lower than 200 nm, so we can assume that the elastic properties of the film are similar to the bulk properties. The low melting temperature ($T_m = 660°C$) of Al enhance a coarsed grain structure (Structure Zone Diagram). Nevertheless, a difference in microstructure between the three samples can be seen:

- **Al-19-2**: It presents the most coarsed grains and the most pronounced texture. Its density is similar to the bulk polycristalline Al.
- **Al-26-2**: It has been deposited in HiPIMS with a substrate negative bias, so it acquired the most uniform thickness and the smoothest surface(Fig.5.6b). Grains are smaller than Al-19-2, and no texture is present, bu some porosity is observable, resulting in a lower density.
- **Al-27-2**: It has been deposited in HiPIMS without a substrate bias. It presents grains with a size similar to Al-26-2, but some grains are bigger (abnormal growth) and the surface is not as smooth as Al-26-2.

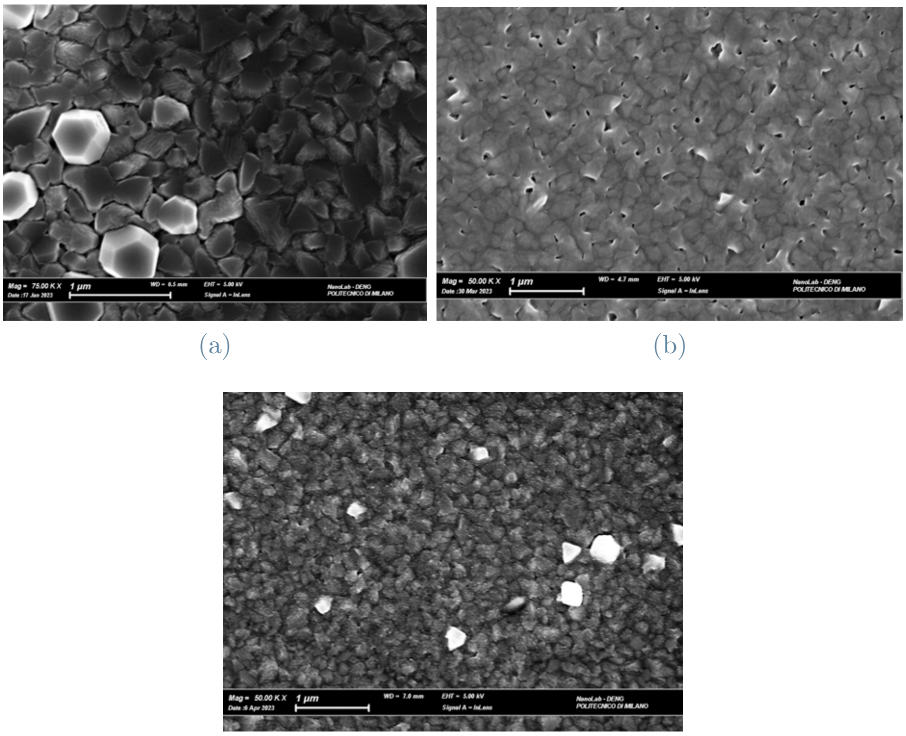
Mag = 75.00 K X
1 µm
Date :17 Jan 2023
WD = 6.5 mm
EHT = 5.00 kV
Signal A = InLens
NanoLab - DENG
POLITECNICO DI MILANO
Mag = 50.00 K X
1 µm
Date :30 Mar 2023
WD = 4.7 mm
EHT = 5.00 kV
Signal A = InLens
NanoLab - DENG
POLITECNICO DI MILANO
Mag = 50.00 K X
1 µm
Date :6 Apr 2023
WD = 7.0 mm
EHT = 5.00 kV
Signal A = InLens
NanoLab - DENG
POLITECNICO DI MILANO

(a)

(b)

(c)

Figure 5.5: Sample magnification with SEM of the as-deposited samples: (a) Al-19-2, (b) Al-26-2, (c)Al-27-2

As seen in figure Fig.5.5, some grains are larger and brighter, especially in Al-19 sample; an abnormal grain growth has occurred. As discussed in chapter 1, several different mechanisms lead to preferential grain growth:

- substrate-film surface energy minimization: it occurs for (111) oriented grains in FCC crystal at high T.

- strain-energy minimization: (100) grains have a low biaxial moduli M_{hkl}, so, in elastic-strain regime, their growth tend to minimize the overall strain energy. It occurs at low T.
- Once the strain exceeds the elastic limit, yielding takes place. Grains that yield more rapidly gain an energetic advantage in their growth. This mechanism specifically promotes the growth of (110) grains [18].

The competitions between these mechanisms at a given temperature determines the 'texture' of the film. We can assume that the larger grains in the as-deposited film have an (100) orientation (low T deposition).

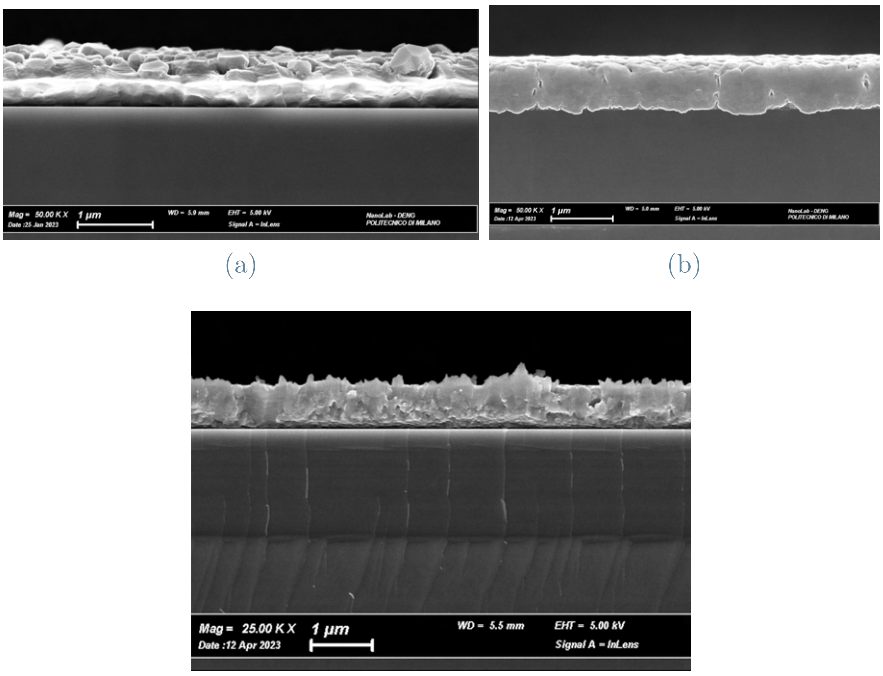

(a)

(b)

(c)

Figure 5.6: Sample magnification with SEM: Cross section of(a) Al-19-2, (b) Al-26-2, (c)Al-27-2. Al-26-2 shows the most compact structure, with the lower crystal dimension.

Al Brillouin Spectroscopy

Being Al on Si a slow film on a fast substrate, it becomes essential to derive a dispersion relation. This relation is crucial for acquiring information regarding the Al elastic constants. Figure 5.7 illustrates the frequency of surface acoustic waves (SAWs), mediated between Stokes and anti-Stokes shifts. While there are additional peaks at lower frequencies, they are disregarded as spurious. These peaks remain constant regardless of the angle (i.e., wavenumber), indicating they are not associated with SAWs but rather to some non traveling excitation, if they are not an instrumental artefact. Using eq.(4.10), a plot of the level curves of the Least Square Estimator as a function of the constants C_{11} and C_{44} has been drawn (Fig.5.8).

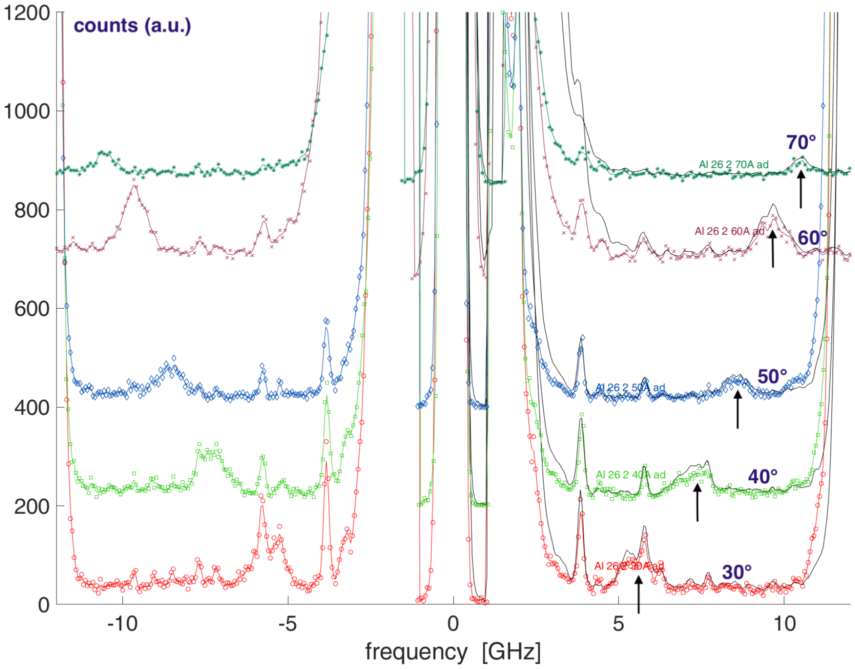

Figure 5.7: Brillouin frequency spectrum of Al-26 made at different angles. Arrows indicate Rayleigh peaks; Peaks at lower frequencies are spurious, since they don't disperse.

The prevalent transverse components of Rayleigh's and Sezawa's waves enables a precise determination of the C_{44} constant, which is equivalent to the shear modulus G in isotropic materials. However, the accuracy in determining the C_{11} constant is relatively poor[44]. Physical and mechanical limits can set bounds to C_{11} values:

- The bulk modulus of the film K_{film}, i.e., its compressibility, cannot exceed the bulk value K_{bulk}. Due to the high density of grain boundaries and the higher free volume of nanocrystalline thin films, they can resist less to compression then the polycrystalline bulk material.

- The film's (G/K) ratio consistently remains lower compared to that of the bulk material. This ratio (G/K) represents both the resistance to shape variation (G) relative to volume alteration (K) and serves as an indicator of a material's ductility.Given that G corresponds to the material's elasticity concerning shape alterations, the film's lower (G/K) ratio can be attributed to the diminished average atomic bond energy within nanocrystalline materials. Consequently, the film exhibits a lower

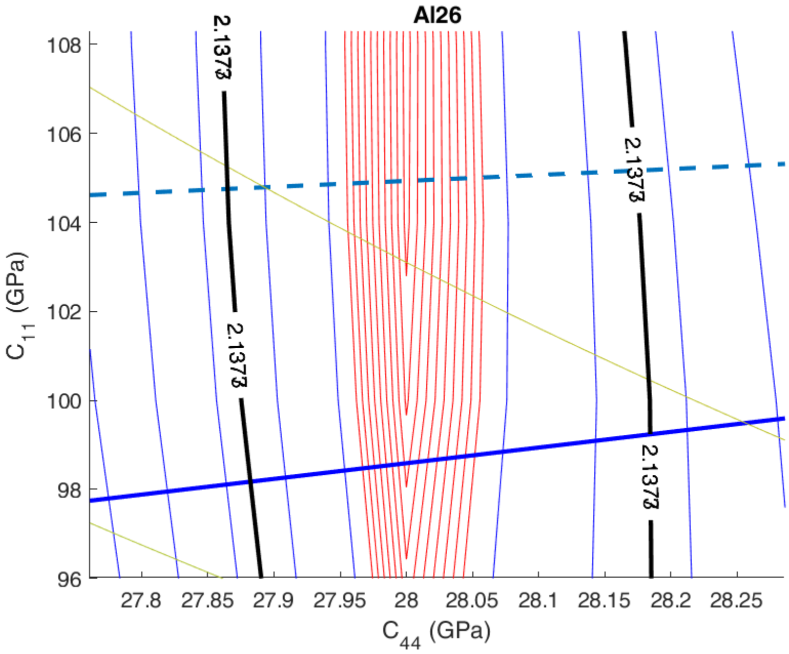

Figure 5.8: LS level curves. Red curves represent lower values of LS. The straight continue line represent the bulk modulus (K$_{bulk}$) of bulk Al, while the dotted one the ratio (G/K$_{bulk}$)

(G/K) ratio than the bulk material due to these properties.

Based on these considerations, we can plot lines associated with K$_{bulk}$ (K$_{bulk,Al}$=67GPa) and (G/K)$_{bulk}$ (G$_{bulk,Al}$=31GPa). By intersecting these lines with the 68% confidence region on the (C$_{11}$,C$_{44}$) map obtained from the LS estimator, we can define a quadrilateral. The center of this quadrilateral is identified as the best estimate, and the half amplitudes of the intervals it encompasses are taken as estimates of the uncertainties. Knowing that for an isotropic material:

$$\begin{cases} K = C_{11} - \frac{4}{3}C_{44} & (5.1a) \\ G = C_{44} & (5.1b) \\ E = \frac{C_{44}(3C_{11} - 4C_{44})}{C_{11} - C_{44}} & (5.1c) \\ \nu = \frac{C_{11} - 2C_{44}}{2C_{11} - 2C_{44}} & (5.1d) \end{cases}$$

We can calculate K,E,G,ν and their uncertainties with the error propagation formula. For Al-27-2 the values obtained are:

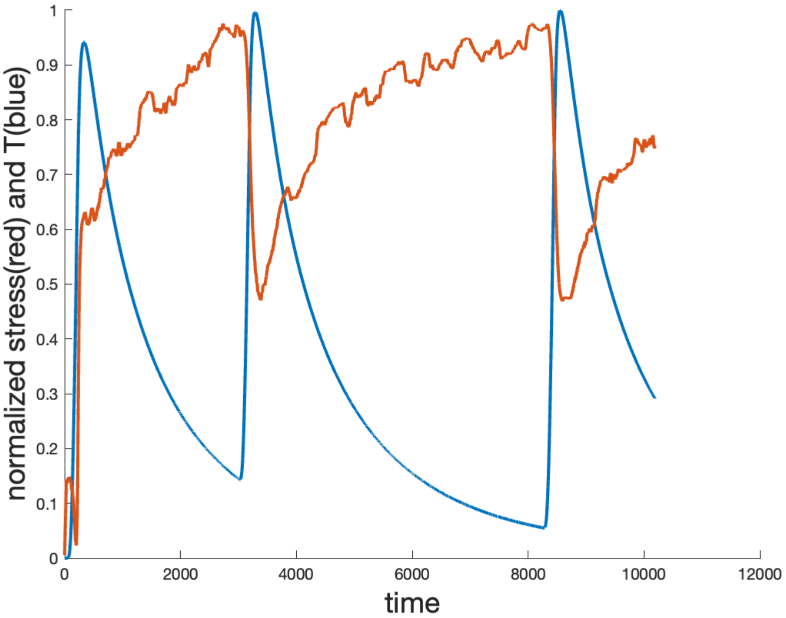

Figure 5.9: Normalized Stress (red) and Temperature (blue) vs time. A filter has been applied to better visualize the stress behavior.

	Al-26	**Al-27**
C_{11} (GPa)	93.7±7.7	100.5±3.5
ν	0.32±0.02	0.31±0.01
G (GPa)	24.7±0.2	28.1±0.2
E (GPa)	65.3±1.1	70.2±1.0
K (GPa)	60.8±1.1	63.0±6.1

Table 5.2: Measured and calculated elastic propertis of Al TF

The biased sample Al-26-2, with the lower density, has a lower Young modulus. This is probably due to the presence of voids and entrapped background gas. Elastic properties of Al-19 are deducted from bulk properties, since it has a significantly higher grain's mean size.

After evaluating the elastic properties of aluminum thin films, the coefficient of thermal expansion can be determined using the Wafer Curvature Technique. Once a plot depicting stress or curvature versus temperature (T) is obtained, the calculation of CTE involves analyzing the linear segment of the graph. Non-linear portions are addressed subsequently to gain a comprehensive understanding of plastic deformation behavior.

Figure5.9illustrates a characteristic behavior observed in films with a coefficient of thermal

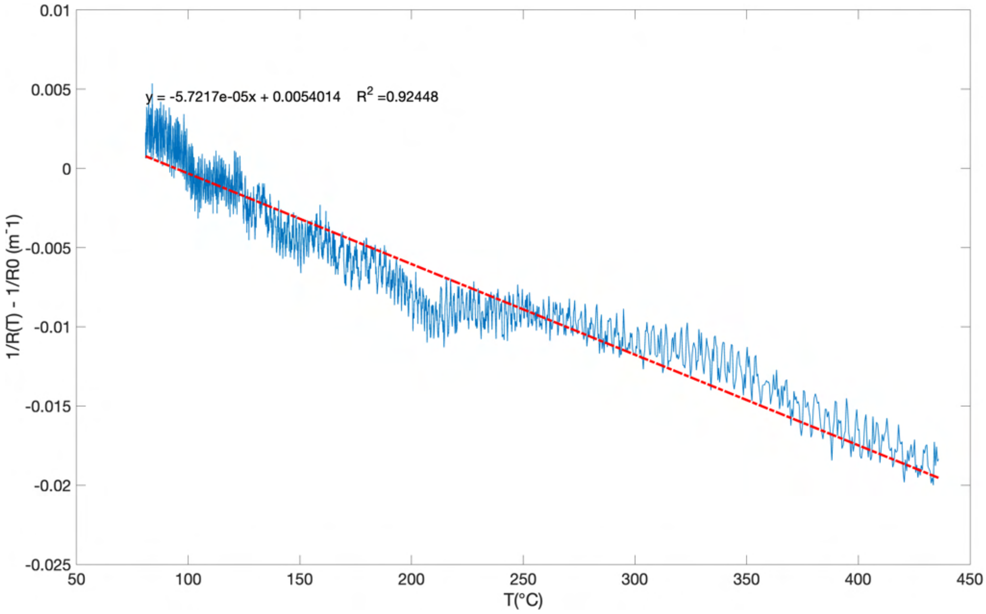

Figure 5.10: Linear segment of κ vs T plot of Al-27-2 during cooling.

expansion (CTE) greater than that of the substrate. As temperature increases, the film experiences the development of compressive stresses. The rapid temperature increase during heating (with a rate of dT/dt $\sim 2°C/s$) encourages the occurrence of nonlinear behaviors, probably due to several causes, not excluding simple settling of the sample on the heating plate, on which it is only resting, so as not to impose constraints. In the cooling phase these phenomena are less present, so we consider only the coolings. Consequently, our focus is solely on the cooling slopes. In each cycle, a linear regression is conducted on the Curvature vs Temperature plot. The confidence interval for each angular coefficient is calculated, and it is associated with the R^2 value using a t-distribution (68%). Following this, we compute the mean of the angular coefficients (b $= d\kappa/dT$), taking into account the weight of each contribution based on its uncertainty. Other source of uncertainties in CTE measure are linked to the substrate thickness ($\pm 10\mu m$), the film thickness ($\pm 10nm$), and the elastic constants (discussed above).

Through Stoney equation and error propagation, the CTE obtained are:

	Al-19	**Al-26**	**Al-27**
CTE$\times 10^6$ (K^{-1})	19.5±0.5	20.1±0.8	14.5±0.65

Table 5.3: Measured and calculated elastic propertis of Al TF

There are no notable differences in the measured coefficients of thermal expansion (CTE), except for Al-27-2, which exhibits a CTEvalue lower than the others. It's important to highlight that these CTE values are lower than both the bulk CTE values and the CTE values of Al thin films reported in the literature[55]. Due to the limited number of measurements, these values should not be attributed statistical significance. Additional measurements are essential to either confirm or dismiss these results.

Non-linear behaviour

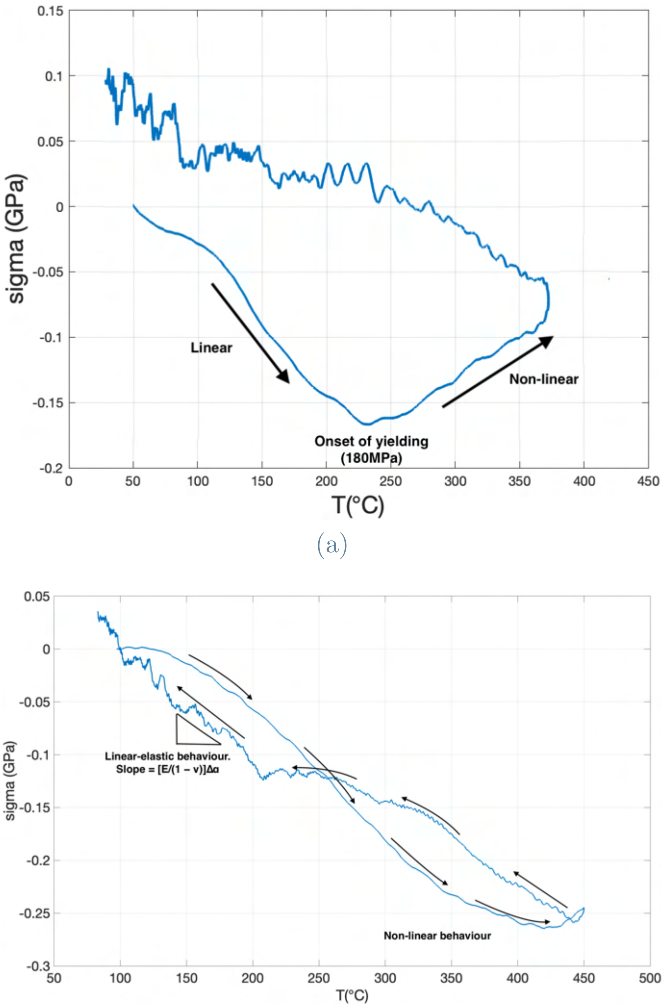

(a)

(b)

Figure 5.11: Stress vs Temperature: the non-linear behaviour is shown. (a)Al-19-2, (b) Al-27-2

All samples were annealed before heating, so no residual stress were present. Looking at Fig5.11, we can see a thermal cycle for Al-19-2 and Al-27-2 we can see two different nonlinear behaviour.

Al-19-2: At 200-250°C (180MPa) a plastic flow mechanism begins: the stress invert its

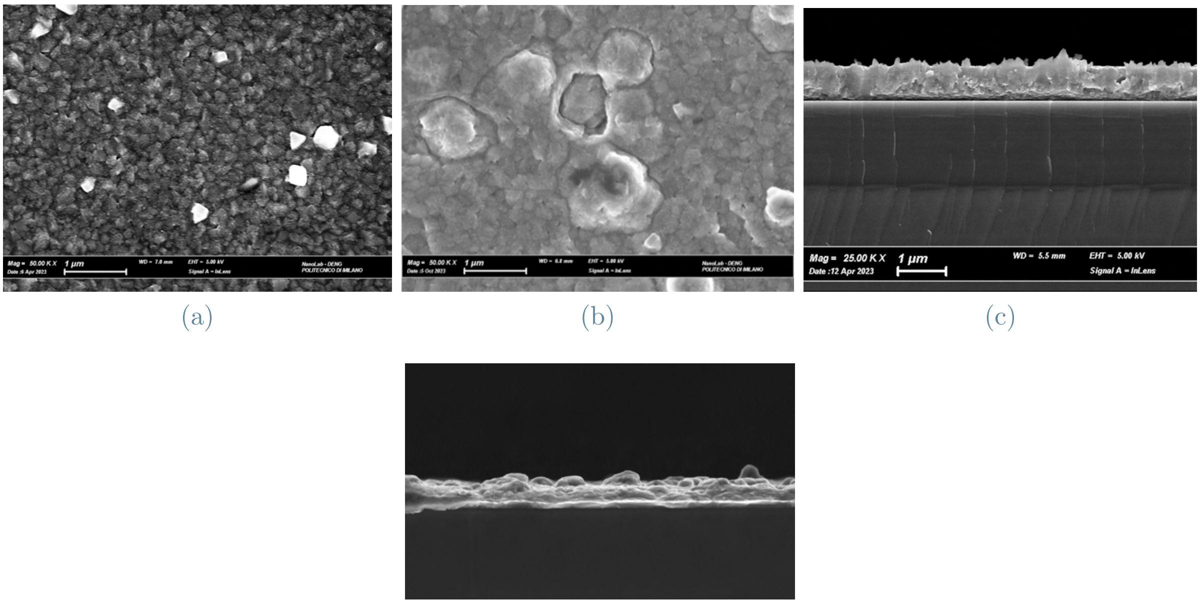
Mag = 50.00 K X
1 µm
WD = 7.0 mm
EHT = 5.00 kV
Date :6 Apr 2023
Signal A = InLens
NanoLab - DENG
POLITECNICO DI MILANO
Mag = 50.00 K X
1 µm
WD = 6.8 mm
EHT = 5.00 kV
Date :5 Oct 2023
Signal A = InLens
NanoLab - DENG
POLITECNICO DI MILANO
Mag = 25.00 K X
1 µm
WD = 5.5 mm
EHT = 5.00 kV
Date :12 Apr 2023
Signal A = InLens

(a) (b) (c)

(d)

Figure 5.12: (a) and (c): Al-27 as deposited; (b) and (d): Al-27 after heating. Increased hillocks are observable after heating. The cross sections show a severe roughness modification.

tendency, hence some relaxation mechanisms occurs:

- Force-driven grain growth may occur, with certain grains experiencing growth due to their lower surface energy or reduced yielding resistance. This phenomenon can lead to a densification effect, introducing a tensile component to the overall stress state.
- Low and high temperaure creep (see deformation map **Fig.3.10**) can describe the deformation kinetics.

Al-27-2: A yielding behavior without pronounced densification is observed. In subsequent cycles, yielding takes place at higher compressive stresses, indicating a strain-hardening effect. Figure 5.12 illustrates the SEM magnification of Al-27 in its as-deposited state and after thermal cycles (reaching 600°C): the surface is no longer uniform and exhibits "hillocks." The formation of hillocks in Al thin films is a well-documented phenomenon in the literature [56], contributing to yielding stress relaxation through diffusional flow. Kim et al. [56] suggested that the incorporation of impurities (Ti, W, O) serves as a driving force for significant hillock formation.

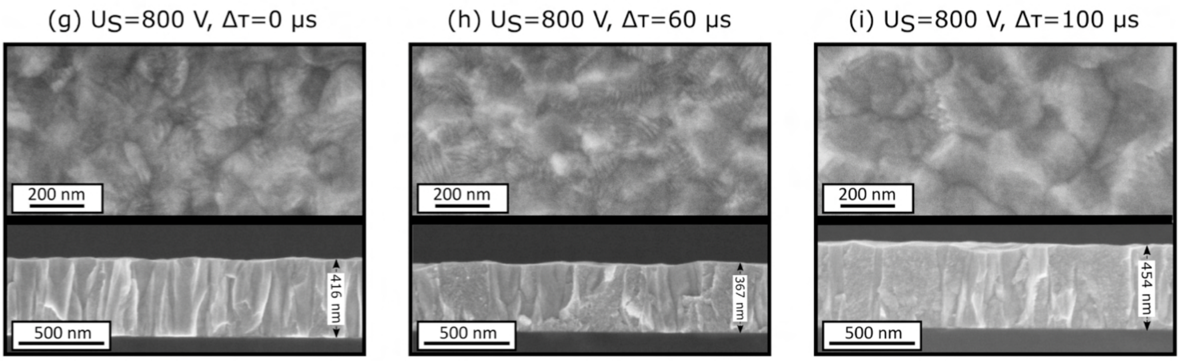
(g) U_S=800 V, ΔT=0 μs (h) U_S=800 V, ΔT=60 μs (i) U_S=800 V, ΔT=100 μs

Figure 5.13: W-133(g), W-137(h), W-140(i)[12]

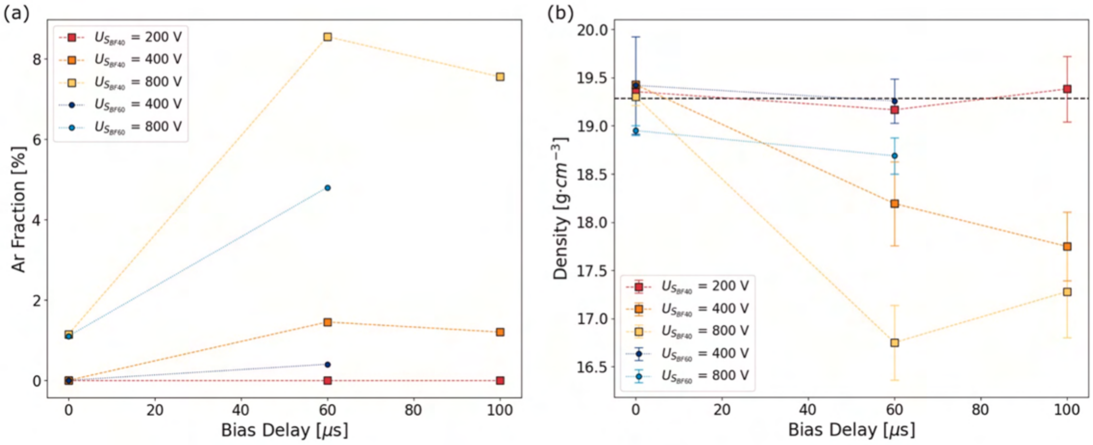

Figure 5.14: Density and Ar (%at) in each samples (yellow dots represents W-133, 137, and 140)[12]

5.3.2. Nanocrystalline Tungsten

Samples W-133, W-137 and W-140 were deposited by Vavassori et al.[12] with HiPIMS at a duty cycle of 1.75% (100μs pulse) with a substrate bias. Time delays were applied to samples W-137 and W-140 (respectively 60 and 100 μs). Both W-137 and W-140 presented a slightly lower density (due to Ar inglobation) than W-133. All samples are characterized by a densely packed columnar structure associated with a preferential <110>-orientation of the α-W phase[12]. No significance difference in residual stresses is observed(table5.4.

	W-133	W-137	W-140
σ_{res}(MPa)	581±34(c)	729±28(c)	694±31(c)

Table 5.4: Measured residual stresses for W samples,(c)stands for *compressive*

W Brillouin spectroscopy

Brillouin Spectroscopy has been performed on W-137 sample, showed in Fig.5.13): W-140 has a density similar to W-137, so we can assume the same elastic properties. For W-133, on the other hand, has a higher density and a more compact structure. A less precise method to determine Young Modulus is using the Rayleigh velocity measured at 70° ($\lambda_{||}$=273nm ∼ $t_f/2$, small interaction of the substrate) and Poisson ratio of the bulk material (ν=0.288). Following this procedure, **E$_{W133}$=363±15 GPa**.

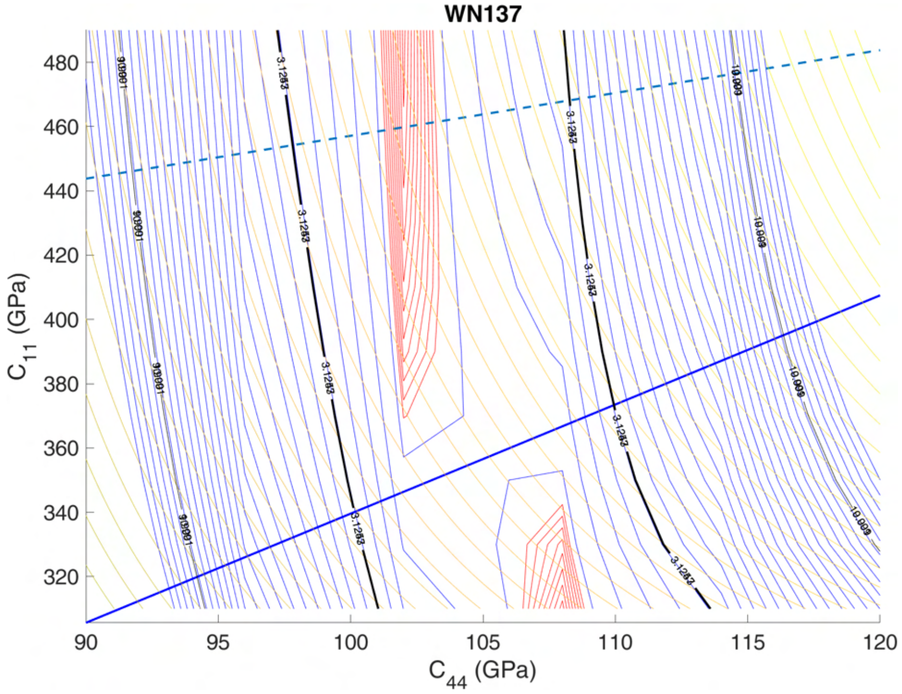

Figure 5.15: W-137 LS estimator level curves: As seen for Al, bounds are set for K$_{bulk}$(continuous blue line) and (G/K)$_{bulk}$(dotted line); black curve is 68% confidence region. Yellow lines represent constant Young moduli.

	W-137
$\rho(g/cm^3)$	16.7±1.0
C_{11} (GPa)	403.5±64.5
ν	0.326±0.039
G (GPa)	103.9±6.1
E (GPa)	275.6±15.2
K (GPa)	265.0±14.9

Table 5.5: Measured and calculated elastic properties of W-137

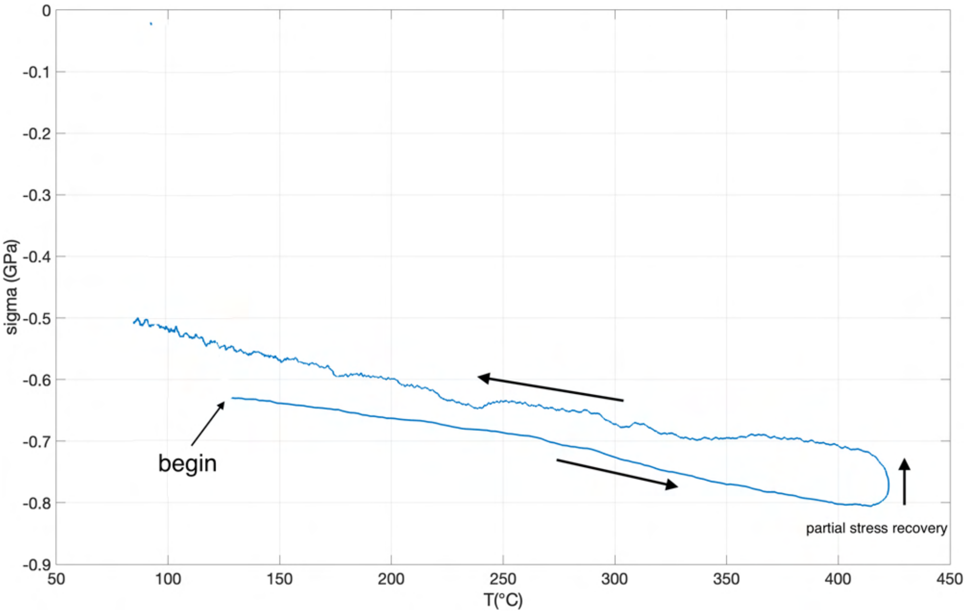

Figure 5.16: Stress Temperature Diagram for W133

Residual Stress Relief

It is well known that tungsten is an inert material: its compressive strength is up to 3500 MPa (at low T), and recrystalliztaton and grain growth begin at T>1100°C. So, plastic flow is not observed in these samples, and only a partial residual stress recovery is observed (Fig.5.14). The mechanism is unknown, but it can be linked to a crystallization of a metastable phase present due to the interdiffusion of Si and W (for example W_5Si_3 phase[12])

CTE

The measured value of CTE for W-133, W-137 and W-140 are very similar to the bulk values (5×10^{-6}):

	W-133	W-137	W-140
CTE×10^6 (K^{-1})	5.1±0.5	5.87±0.13	5.32±0.4

Table 5.6: Measured CTE

There is no significant difference observed among these three samples, except for a slightly elevated value in W-137, which exhibits lower density, indicating a higher percentage of void fraction. Although the samples are nanocrystalline, their CTE is not much different from that of the bulk material; this could be due to the high compactness and density.

5.3.3. Amorphous Tungsten

Sample **WFW1004** was deposited with PLD in a helium atmosphere at 70 Pa, resulting in the formation of an **amorphous**, **non-porous** structure. The crystallite dimensions do not exceed 2 nm, and the density is approximately 11 g/cm^3. The biaxial modulus is reported to be 227 GPa[49]. Anticipated is a higher coefficient of thermal expansion (CTE) compared to the bulk material, as the lower mass density of the amorphous phase leads to increased interatomic distance and reduced binding energy. Consequently, the average displacement of atoms from their lattice positions is expected to be heightened.
The sample was deposited on a bilapped Si wafer, enhancing the accuracy of measurements by allowing assessments on both sides.
The residual stresses were very small compared to HiPIMS samples, about 73MPa. Figure 5.17 illustrates the initial thermal cycle of WFW1004. A notable observation is the onset of a densification effect in the temperature range of 180-200°C. The metastable state of the as-deposited film transforms into a more stable state, leading to an increase in density and the consequential densification effect. Subsequently, a significant tensile stress of 323 MPa is developed as a result of this process. Observing Figure 5.18, it becomes evident that the crystallization of amorphous tungsten initiates within the temperature range of 450 to 650°C. This suggests that while significant grain growth may not occur, there is a more probable reduction of voids in the film due to structural relaxation, leading to a subsequent increase in density. The measured CTE is $\mathbf{(6.92 \pm 0.24)} \times 10^{-6}$, which is consistent with previous results in literature[49].

5.3.4. Tungsten Nitride

Samples **WN-19**, **WN-21**, **WN-39**, **WN-40**, were all deposited with HiPIMS in an atmosphere of argon and nitrogen with a total pressure of 0.5 Pa. Unlike with argon

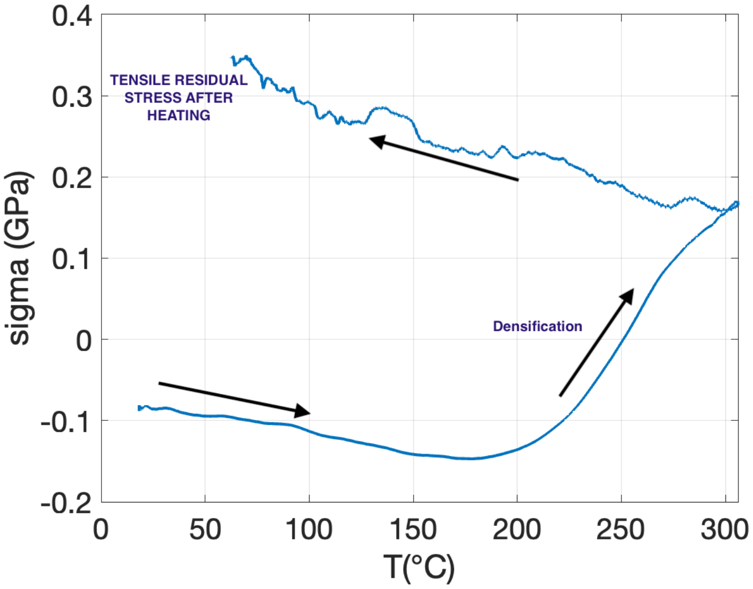

Figure 5.17: Stress Temperature Diagram for WFW1004

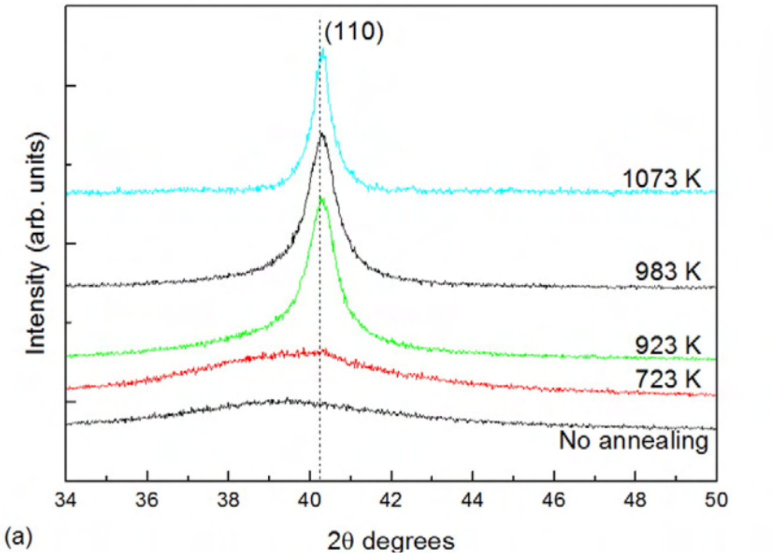

Figure 5.18: XRD of amorphous W as a function of the annealing temperature; a peak linked to the (100) crystal develops at temperatures higher than 450°C. Figure from [57]

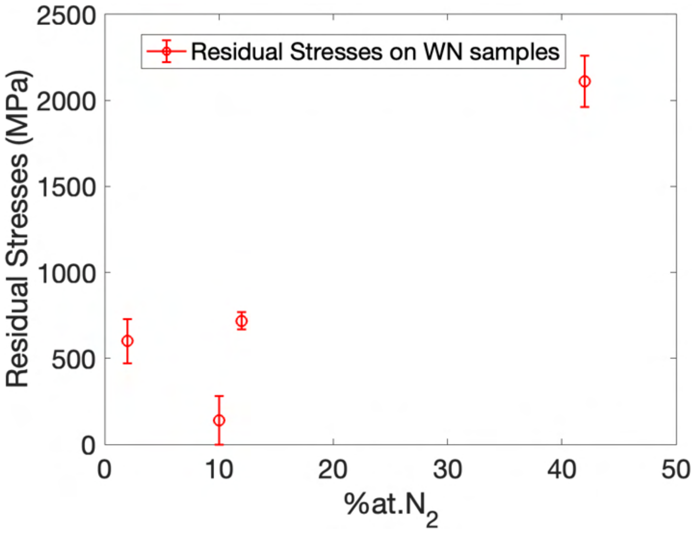

Figure 5.19: Measured residual stresses of the as-deposited samples

alone, with nitrogen the application of a substrate bias can produce a densification effects in the film and a lower atomic fraction of nitrogen: bias tends to break the W-N bond, reducing the amorphousness of the film and promoting a nano-crystalline microstructure.

WN Samples

Sample	N_2 partial pressure (%)	Bias	N_2%at.	density (g/cm^3)
WN-19	10%	yes	2-3%	18.8
WN-21	25%	yes	∼10%	20.3
WN-39	10%	no	10-12%	17.9
WN-40	50%	yes	42%	-

Table 5.7: Deposition parameters, atomic composiotion and density of WN samples

Very high compressive residual stresses have been measure for WN-40, WN-39 and WN-19. The higher compressive residual stress, 2.11 GPa, is observed for WN-40: the presence of a high quantity of nitrogen has induced a high stress. Several other measurements have to be done in order to explain quantitatively the effect of nitrogen on the residual stresses.

Brillouin spectroscopy

Brillouin spectroscopy have been performed on WN-21 and WN-39. From WN-21 and WN-39 spectra we obtained values for velocities both for Sezawa and Rayleigh modes, for

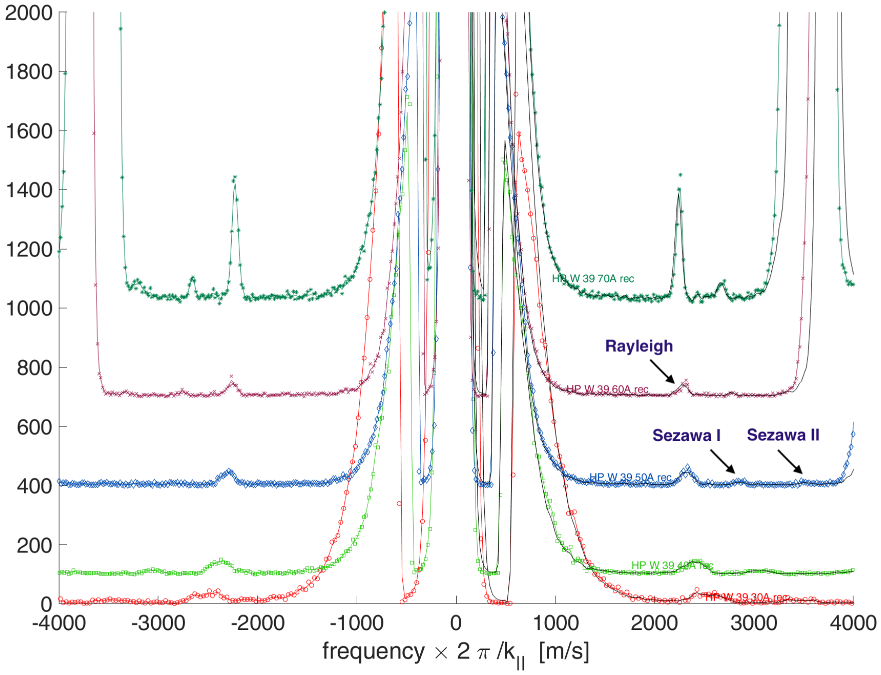

Figure 5.20: Brillouin Spectra at different angles for WN-39; we can see both Rayleigh's and Sezawa's modes

a total of three dispersion relations for each sample (Figure5.20). A sensible increase in accuracy on elastic constants' determination is achieved(Figure5.21).

	WN-21	**WN-39**
C_{11} (GPa)	448±40	415±53
ν	0.329±0.029	0.312±0.023
G (GPa)	122±2	105.5±2.5
E (GPa)	320.1±7.2	280±8
E (GPa)	285.3±6.3	274.3±8.2

Table 5.8: Measured and calculated elastic properties of W-137

Residual Stress Relief and Densification

For WN-39 and WN-21 an strong densification effect has been observed for temperatures higher than 300°C (Fig.5.22). A tensile residual stress develops after thermal cycling. For WN-40, the residual stress reached such high levels that the thermal cycling resulted in film cracking and delamination, attributed to a buckling effect. Notably, an immediate stress relief was observed at 450° C. Microscopic examination under SEM magnification

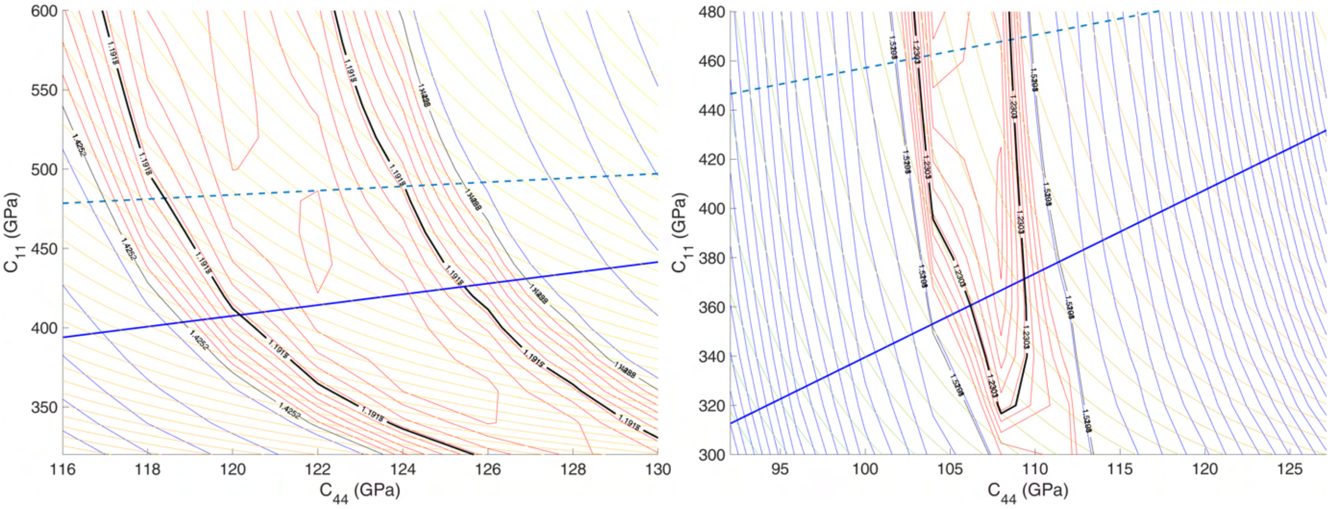

(a)

(b)

Figure 5.21: Intersection between elastic constants of bulk W and LS level curve corresponding to 68% confidence region. (a)WN-21 and (b) WN-39

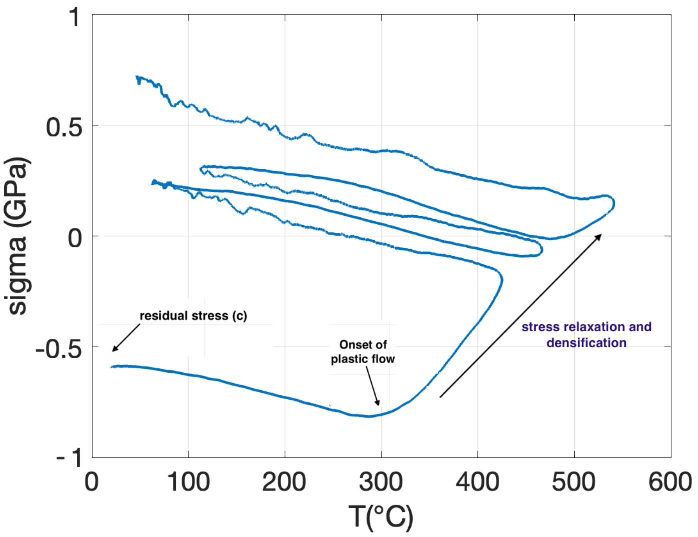

Figure 5.22: Thermal cycles for WN39. Stress relaxation occurs through densification at every cycles, for a combined effect of plastic flow and structural relaxation.

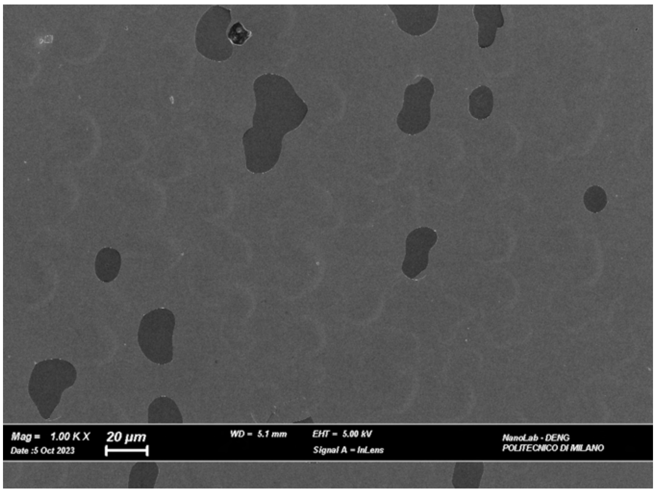

Figure 5.23: SEM image of annealed WN40 surface.Darker regions on the surface signify areas where the film has undergone delamination.

revealed micrometric fractures and distinct delamination spots on the surface, providing visual evidence of the structural impact caused by the pronounced residual stress and thermal-induced strain (Fig.5.23).

CTE

Again, the measured CTEs are not much different from the bulk W CTE ($5\times10^{-6}K^{-1}$):

	WN-19	**WN-21**	**WN-39**	**WN-40**
CTE$\times10^6$ (K^{-1})	5.66±1.29	5.27±0.87	5.49±0.24	4.95±0.41

Table 5.9: CTEs of WN samples

5.3.5. Yttrium Oxide

In alumina systems, certain elements have been identified to impede crystalline growth. Specifically, Yttria and Lanthanum oxide have demonstrated the ability to stabilize the γ phase, hindering the transition to the more stable sapphire phase. The researchers noted that at elevated temperatures (900-1000°C), alumina reacts with yttrium oxide Y_2O_3 (or La_2O_3), resulting in the formation of a ternary compound. The produced AlYO3 (or LaAlO3) exhibits an isostructural relationship with γ alumina, effectively preventing the rearrangement of the material and thereby stabilizing it in its less stable phase[58]. In order to characterized these materials and to establish the accuracy of the techniques for ceramic materials, a thick (5μm) Y_2O_3 film deposited with PLD on Si substrate has been examinated. The measured CTE is $\mathbf{(16.85 \pm 0.73)}\times10^{-6}$ $\mathbf{K^{-1}}$, much higher than the bulk value (8×10^{-6} K^{-1}).

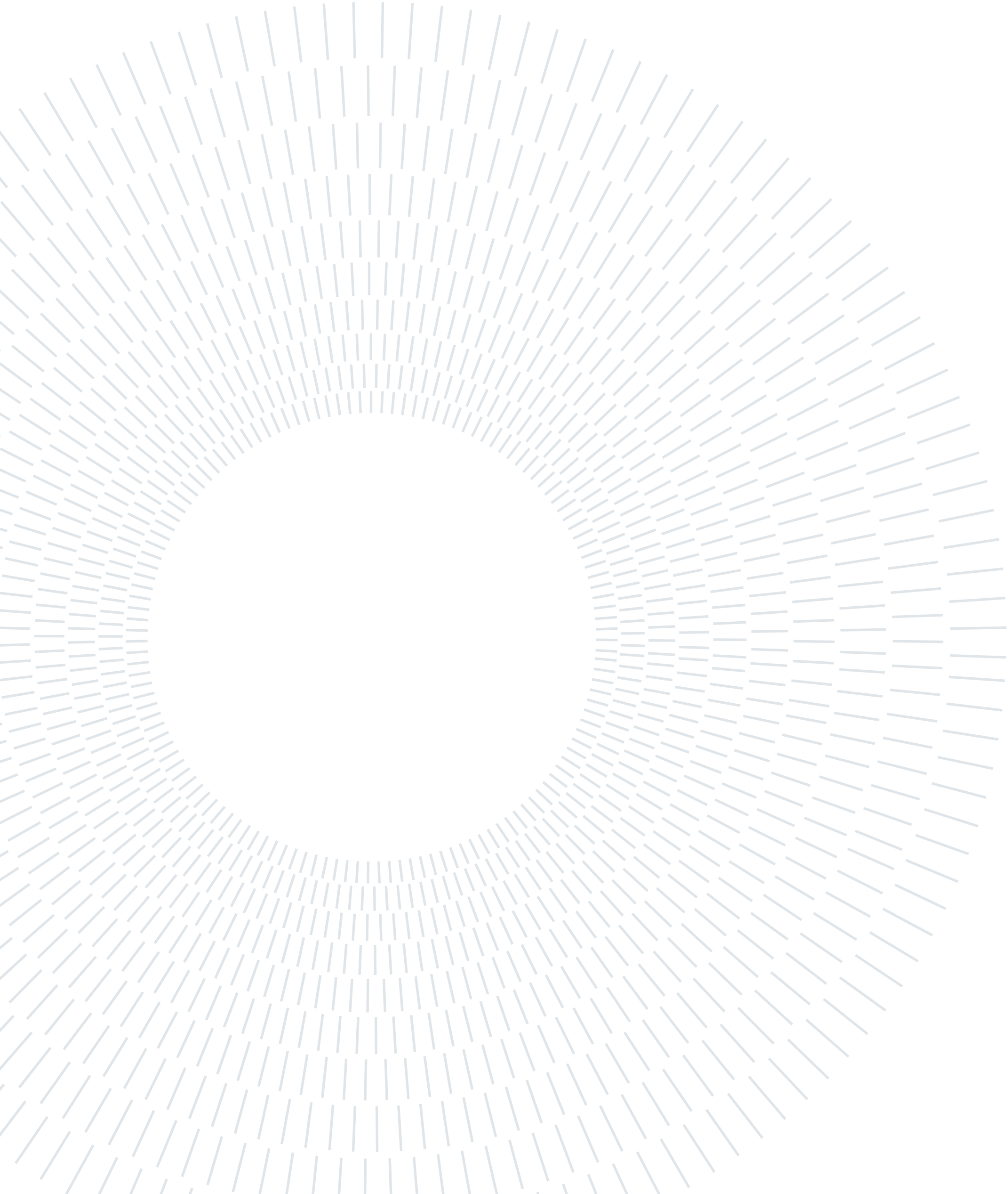

6 | Conclusions and future developments

In this study, we conducted a comprehensive characterization of the thermo-mechanical properties of thin films made of Aluminum, Tungsten, and Tungsten-Nitride. Our focus extended to establishing correlations between deposition techniques, film microstructure, and the elastic, plastic, and thermal properties of these films. To achieve this, we employed Brillouin spectroscopy and the Substrate Curvature Technique, optimizing the measurement system for heightened sensitivity and accuracy. Significant enhancements were achieved in the Substrate Curvature Technique, with a relative sensitivity increase by a factor of approximately 6. Our investigations encompassed amorphous, nano-crystalline, and micro-crystalline samples, exhibiting a broad spectrum of densities and residual stresses.

The Brillouin measurements underscored the influence of crystallinity and density on stiffness. A higher density of grain boundaries per unit volume correlated with an increased void fraction and decreased density. Consequently, smaller crystallite dimensions and greater mean spacing between atoms were associated with lower stiffness. Simultaneously, a higher strength was anticipated, akin to the Hall-Petch effect.

For instance, in the case of HiPIMS WN, we observed a notable discrepancy in E values between high-density nanocrystalline WN-21 (320 GPa) and low-density WN-39 (280 GPa). Notably, both samples contained the same nitrogen content, but the former, deposited with substrate bias, exhibited a densely packed structure, leading to the observed variations in mechanical properties.

Similar behaviour has been observed for Al samples. The wafer curvature technique permit us to measure residual stresses and thermal expansion coefficient (CTE) of thin film, as well as a qualitative description of stress relaxation mechanisms and onset of plastic flow.

In the case of aluminum samples, the compressive yielding stress has been noted to be significantly higher than that of bulk aluminum, ranging between 150-200 MPa compared

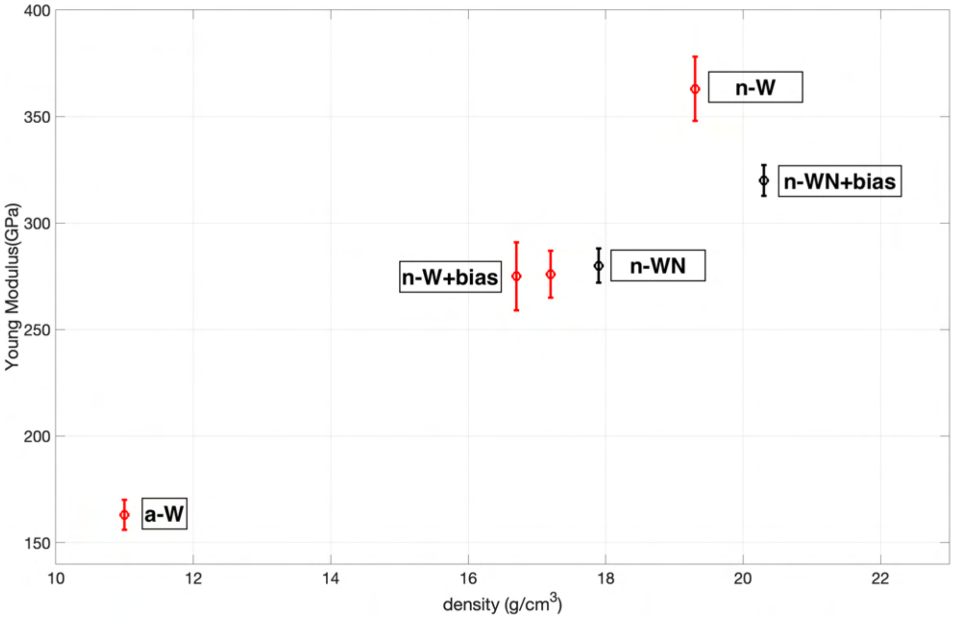

Figure 6.1: Young Modulus of W samples (red) and WN samples (black).

to the typical 10 MPa for bulk aluminum. This remarkable increase is attributed to the small grain dimensions and low film thickness. However, evaluating the yield strength for nanocrystalline and amorphous tungsten presents a more intricate challenge. In these cases, the density begins to increase, leading to the development of tensile stress before yielding can take place. The interplay of factors such as grain structure, density evolution, and stress development adds complexity to the assessment of yield strength in tungsten films.

The measurements of coefficient of thermal expansion (CTE) reveal no significant difference between the HiPIMS-deposited samples and the bulk material, with a lower CTE observed for aluminum. In contrast, samples deposited using Pulsed Laser Deposition (PLD) generally exhibit a higher CTE. This disparity may be attributed to the high compactness and density structure of HiPIMS samples, which provides a high atomic bond similar to the bulk material. Additionally, residual stresses play a crucial role in modifying the mean interatomic strength, resulting in lower CTE values. This observation is promising, especially when considering the thermal fatigue that a tungsten film may experience in nuclear applications, potentially minimizing thermal loads. However, it's essential to note that the high residual stresses developed with HiPIMS can lead to failure at lower temperatures. Furthermore, a higher yield strength is associated with a greater hardness (H). The ratio of hardness to Young's modulus (H/E) serves as a reliable indicator of a material's wear resistance. As crystallinity and thickness decrease, yield strength increases, and Young's modulus decreases. This leads to an improved wear resistance,

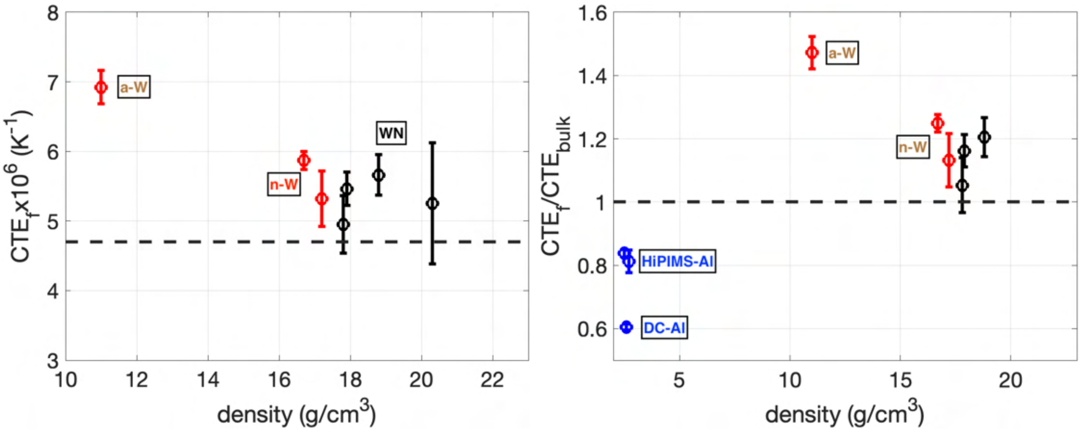

(a)

(b)

Figure 6.2: (a)CTE values of W samples, the dotted line represent the value of bulk-W CTE. (b)Ratio between CTE$_{film}$ and CTE$_{bulk}$ for W(red), WN(black) and Al(blue)

making these films well-suited for Generation IV nuclear applications.

However, the microstructure instability of Al thin films can lead to the formation of hillocks and abnormal grain growth, and prevents it for being used at very high temperatures. Indeed, there is still much to uncover regarding the thermomechanical properties of these films, particularly in understanding how these properties evolve after exposure to factors such as irradiation, a high number of heat cycles, or immersion in a liquid metal environment. These external conditions can introduce complex and dynamic changes in the material behavior, influencing factors like thermal stability, mechanical strength, and resistance to environmental stresses. Investigating the effects of irradiation, heat cycles, and exposure to liquid metal environments on thin films is crucial for evaluating their performance and reliability in real-world applications, especially in fields such as nuclear technology. Research in these areas will contribute significantly to enhancing our understanding of the long-term behavior and durability of these films under various operating conditions.

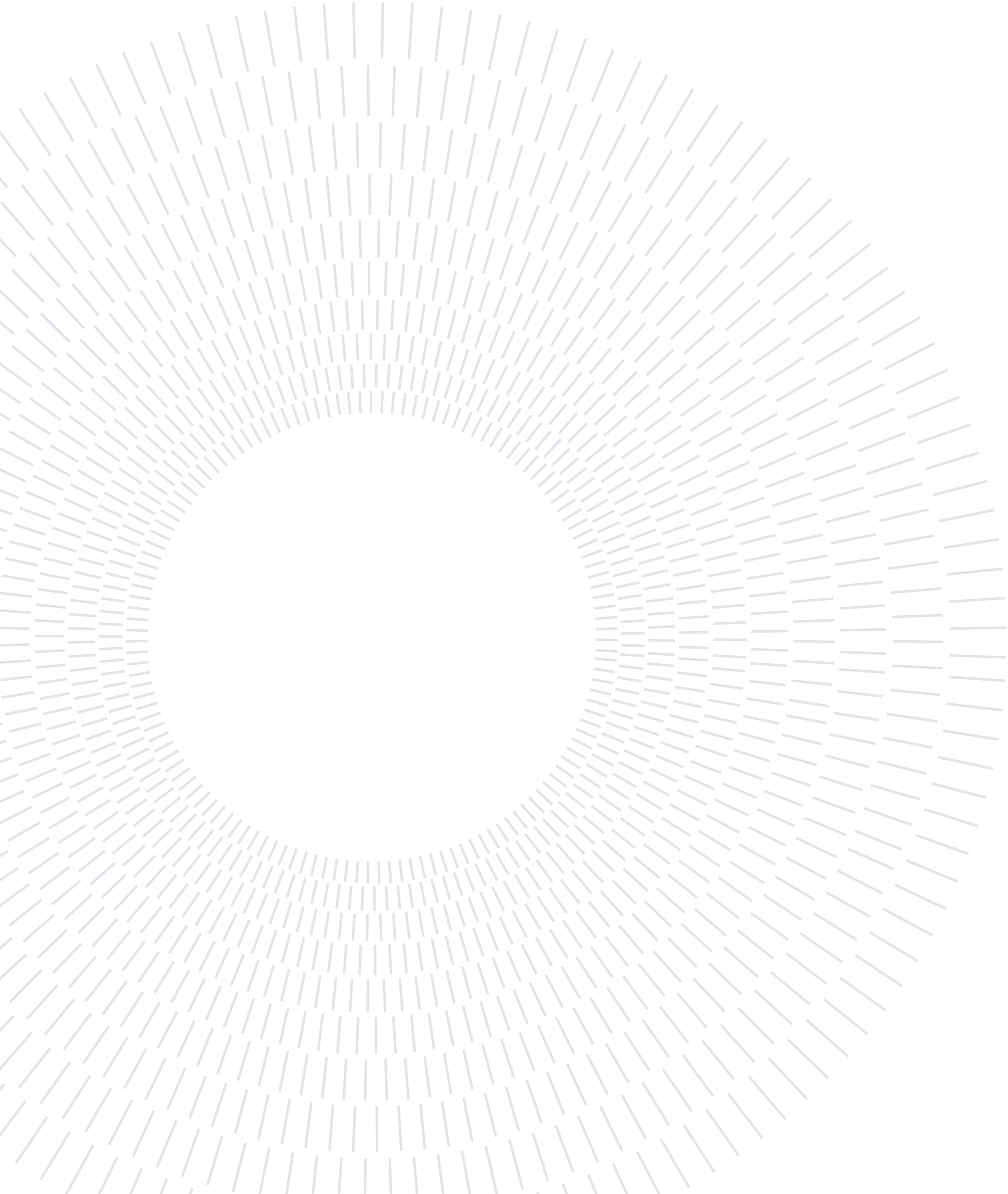

A | Appendix A

A.1. Irradiation effects

It is assumed that, during particle irradiation, energy is deposited instantaneously in a very small region, producing a localized increase of temperature which spreads and dissipates according to the laws of classical heat conduction in a continuum (thermal spike).
If we consider different irradiating particle at the same energy, we can predict what kind of damage will be produced on the target material: electrons and light ions, generally, produces isolated Frenkel pairs (self-interstitial atoms and vacancies), while neutrons and heavy ions, differently, produce energetic displacement cascades, and consequently defect clusters, due to high energy PKA (primary knock-on atom).
A high-energy particle upon impact has the capacity to transfer a portion of its kinetic energy to the primary knock-out atom (PKA). Subsequently, the PKA can transfer its energy to other lattice atoms through collisions, initiating a cascading series of collisions known as a collisional cascade.
As an illustration, consider that a 1 MeV electron striking copper results in a 25 eV PKA, whereas a neutron of the same energy yields a 45 keV PKA.
Neutrons, differently from charged particles or gamma rays, produce an indirect ionization[59], by inelastic scattering or radiative capture and a consequent gamma-ray emission, or transmutation, followed by a proton or an alfa particle emission. Transmutation introduces impurities in the lattice.

The defect production efficiency per DPA (displacements-per-atom, i.e., the mean number of times an atom is moved from its original position) is lower for displacement cascade than for isolated Frenkel pairs, due to recombination and clustering processes of the cascade.
The extent of radiation damage and the temperature constitute the principal factors governing microstructural evolution. The former is linked to the quantity of defects created into the bulk material such as displaced atoms, vacancies, clusters, voids, dislocation loops, precipitates; the second is mainly related to the kinetic of defects interaction and microstructural evolution[32]. Several mechanical, dimensional, and microstructural mod-

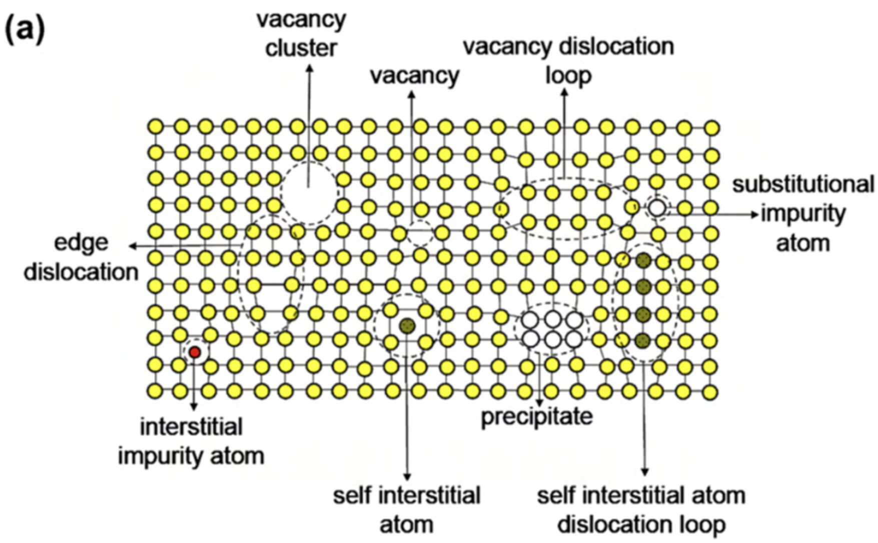
(a)
vacancy cluster
vacancy
vacancy dislocation loop
substitutional impurity atom
edge dislocation
interstitial impurity atom
precipitate
self interstitial atom
self interstitial atom dislocation loop

Figure A.1: Several defects induced by irradiation, mainly due to Frenkel pairs formation[60]

ification induced by irradiation occurs; here below a list.

Radiation induced amorphization: Transition from crystalline to amorphous phase is a radiation-induced process that occur at low temperature. At temperature below a material-specific transition temperature (T_{S_I}), defect migration is inhibited, leading to their accumulation. Amorphization ensues as a direct consequence of collisional cascades, that induce gradual build-up of radiation defects or the increase in free energy associated with the accumulation of defects (chemical disorder). Phase transition usually produces large swelling (5-30%) and a decrease in elastic moduli[32][61]. Saturation in defect concentration occurs at approximately 0.1-0.5 dpa but the dose to induce amorphization increases rapidly with increasing temperature, due to higher defects mobility. Over a threshold temperature, the high mobility of interstitials, clusters and vacancy do not permit any further amorphization.
Snead et al.[61]noted that exposure to fast neutrons on SiC (a ceramic material) resulted in complete amorphization at a dose of 2.56 dpa and 70°C. This led to notable reductions in density by 11% as well as decreases in hardness and Young's modulus by 45%. Complete recrystallization was observed at 1125°C.

Radiation induced hardening and embrittlement (T<0.4Tm; dose>0.1dpa): Defects clusters such as voids, bubbles, dislocation loops clusters or network dislocations are immobile until a threshold temperature, specific for each kind of defect cluster and material. For lower temperatures these defects can create an obstacle for the dislocation motion. Above T_{SV}, these defects become mobile and dissociate; this temperature can be very high (higher than 1000°C for Al_2O_3 and W).

The increase in yield stress is often associated with a decrease in tensile elongation and fracture toughness, especially in bcc metals (such as ferritic steels) [31]. A reduction in absorbed energy before fracture (Charpy test) is observed, as well as an amorphous-ductile transition temperature for bcc metals.

For austenitic stainless steels, a maximum in yield strength is observed around 300°C, which is close to the common temperature values in water reactor.

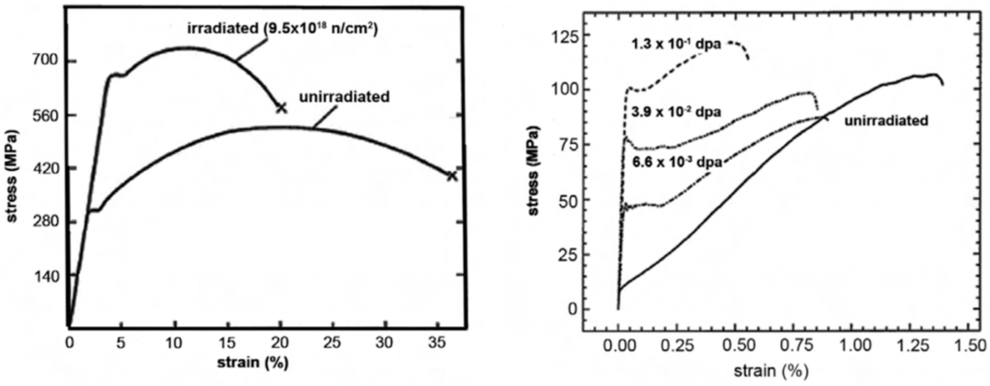

(a)

Figure A.2: Irradiation effects on stress-deformation curve in mild steel(left) and single crystal FCC metal(right)[60]

Irradiation growth (0.1Tm<T<0.3Tm; dose>10dpa) and swelling (0.3Tm<T<0.6Tm; dose>10dpa):

Irradiation growth is a phenomenon that induces macroscopic shape changes, even in the absence of applied stress and without altering volume. This process is attributed to the formation of additional crystal planes due to irradiation. In the presence of a metal texture, characterized by a preferential grain's crystallographic direction, elongation and shrinkage occur due to anisotropy and asymmetry. This shape transformation is particularly pronounced if the extra planes are uniformly oriented. Materials with a hexagonal close-packed (hcp) lattice, such as Zr or $\alpha - Al_2O_3$, exhibit intrinsic anisotropy that favors this phenomenon, leading to a notable decrease in flexural strength.

For $\alpha - Al_2O_3$, microcracking is expected under fast neutron (E>1MeV) fluences exceeding $2 \times 10^{20} n/cm^2$ at 650°C. Fig.A.3[62].

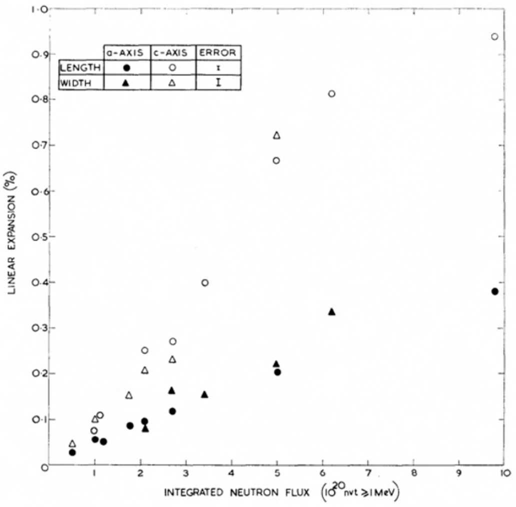

Figure A.3: Linear expansion of different lattice parameters of a FCC metal[62]

Contrastingly, swelling is a process that does not preserve volume; it occurs at higher temperatures than growth, involving the movement of vacancies or vacancy clusters. Once nucleated, typically at grain boundaries or near inclusions, cavities serve as sinks for vacancies, leading to their expansion. As illustrated in Fig.A.3, in austenitic stainless steel irradiated in fast fission reactors, the swelling rate (increase in volume per unit dpa) is 1% per dpa. If volumetric swelling surpasses 5%, engineering design accommodation becomes challenging. Above 10% void swelling, an embrittlement mechanism is observed in austenitic SS.

Void swelling is notably lower in ferritic/martensitic steels, registering at less than 2% after fission neutron damage of 50 dpa, in contrast to the more than 30% observed in series 300 steels: this is due to a higher transient dose before onset of steady state swelling, and a lower content of Ni.

In fact, ^{59}Ni, formed through the neutron capture of ^{56}Ni, promote an (n, α) reaction with thermal neutron:

$$^{59}Ni + n_{th} \rightarrow ^{56} Fe + \alpha; \qquad \sigma_{th}(^{59}Ni) = 1.3 \times 10^4 mb \tag{A.1}$$

The same reaction occurs also in fast neutron spectrum, but with a lower probability (σ_{fast}(Ni)=4.2 mb).

The rate of helium production is proportional to neutron flux and Ni content in the target; due to its insolubility in metals, it tends to create bubbles, starting from preexisting voids. The elevated pressure generated within bubbles, particularly at high temperatures (typically exceeding 0.5 T_m), can result in high temperature helium embrittlement. In presence of tensile stress, intergranular fracture may occur due to helium migration at grain boundaries, as depicted in Fig.A.4. This process involves cavity formations, coalescence, breakaway growth, and eventual rupture under mechanical stress.

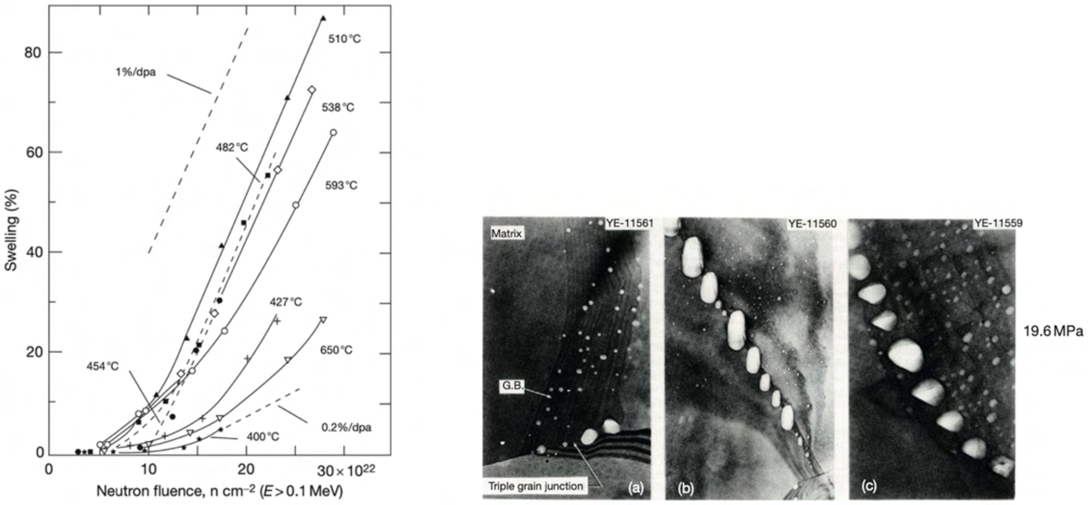

(a) (b)

Figure A.4: Swelling in a FCC metals at different temperatures(a), (b)Voids and bubbles nucleation at GB [32]

Enhanced and induced creep (0.2T$_m$<T<0.45T$_m$; dose>10dpa):
It is widely acknowledged that materials exposed to elevated temperatures (typically exceeding 0.5 times the melting point, T_m) have a propensity to undergo gradual deformation when subjected to prolonged mechanical stresses. This phenomenon, referred to as thermal creep, poses a risk of material failure. Altering the parameters of temperature (T) and stress (σ) can induce various mechanisms at the microstructural level. Specifically, at elevated temperatures and low stresses, interactions between dislocations and point defects result in grain boundary sliding and deformation, a phenomenon known as "Coble creep". At even higher temperatures, a more energy-intensive process takes precedence, involving intragranular motion of vacancies and interstitials, termed "Nabarro-Herring creep," leading to lattice diffusion and deformation.

Both of these processes are diffusive in nature and depend on the quantity of vacancies and interstitials present at a given temperature in a stressed material. Irradiation significantly increases the number of defects in the material, thereby lowering the temperature at which these phenomena occur (radiation-induced creep) and/or increasing the steady-state strain rate when coupled with thermal creep (radiation-enhanced creep).

For ferritic/martensitic steels, the irradiation creep compliance appears to be approximately half that of austenitic steels[32].

Crystallization

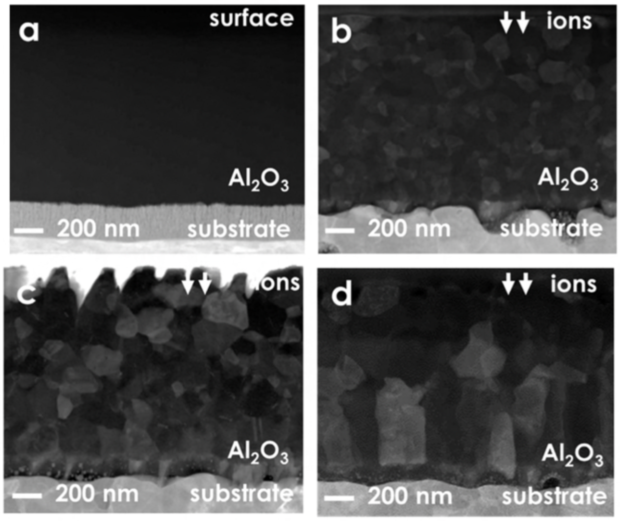

Figure A.5: Crystallization and grain growth induced by neutron fluence in Al_2O_3 [34]

We know that at low T, radiation can induce amorphization. Although, starting from an amorphous ('a') phase, a crystallization is observed. For example, Nakamura et al.[35] observed that in electron irradiated a-Al2O3 a crystallization occurs through an "excited" or "stimulated" amorphous state. In this state, there is breaking and rearrangement of unstable short-range Al-O bonds (specifically involving the fivefold-coordinated Al-O (AlO_5) basic units).
The crystallization process becomes more pronounced at electron energies unable to break the interatomic bonds. This observation suggests that electronic excitation processes play a dominant role in the transformation. In other words, the interaction between electrons and the material at lower energies is more effective in inducing crystallization.
The capture of interstitials by grain boundaries contributes to grain coarsening. Grain mean dimension increases as dose increases **(Fig.A.5)**.

LIQUID METAL EMBRITTLEMENT AND CORROSION

Use of heavy metals as coolant represent an interesting oppurtunity for several reasons, but it deeply affects the behaviour of the steels with which HM come into contact. Corrosion and liquid metal embrittlement (LME), especially at high temperature and high flow rate, are the main obstacles.

Numerous mechanisms have been proposed to elucidate the occurrence of failures in liquid metal environments. In this context, liquid metal infiltrates the grain boundaries of the solid material, facilitated by a decrease in grain boundary surface tension or a reduction in surface free energy due to the wetting nature of the liquid metal. Subsequently, a weakly bonded alloying zone forms, leading to grain boundary decohesion. The adsorption of liquid metal induces a decrease in cohesive forces at the crack tip, resulting in intragranular brittle tensile failure at lower stress levels. Alternatively, liquid metal adsorption can enhance plasticity, manifesting as the ingress and egress of dislocations at the crack tip, leading to embrittlement through a ductile dimpled rupture mode. Another potential scenario involves the diffusion of liquid metal into the grain boundaries (intergranular) or twin boundaries[63].

The general effect is an immediate loss of ductility; it is known that only certain combination of liquid and solid metals resulted in embrittlement. The vast number of experimental variables and the complex interplay thereof make it essentially impossible to prove that a given liquid–solid pair will not result in embrittlement under some combination of conditions. An effect of temperature, deformation rate, exposure time, grain size, composition is observed[63], but the complex dependence of LME on these parameters makes almost impossible to do any prediction. LME is system-specific as it is a chemical reaction.

The coarse-grained materials experience more severe embrittlement than those with smaller grains.

An important case study on the temperature effect is represented by lead-bismuth eutectic (LBE) on T91 steel (martensitic-ferritic, 9Cr-1Mo): despite the low solubility of this material in LBE, at temperature greater than 500°C the oxide layer becomes less protective and the direct contact with liquid metal induces the embrittlement and the dissolution of the steel[63].

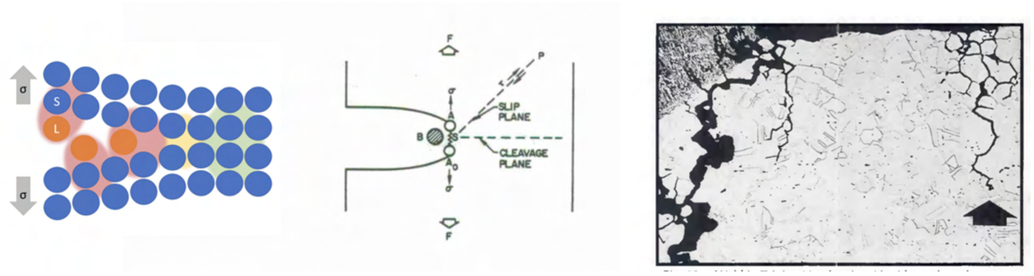

(a)

(b)

Figure A.6: Increase of local plasticity and emission of dislocations from crack tip.(a) LME mechanism[63], (b) intragranular LME[64]

LBE is a phenomenon often associated with structural material corrosion (Liquid Metal Corrosion, LMC): the loss in ductility and the liquid metal penetration causes the dissolution of the structural elements in the coolant due to the physical-chemical interaction between the two. Lead pick preferentially Ni (but also Fe, Cr, Mn) promoting the ferritization of the steel in the outer layers. The change in the microstructure, composition and surface morphology can significantly affect the mechanical and physical properties[65]. Heavy mass transfer to the liquid is observed for austenitic stainless steels at 800°C with a Pb flow rate of 0.5 cm/s A.7. The presence of molybdenum and niobium in the alloy strongly reduces the corrosion rate.

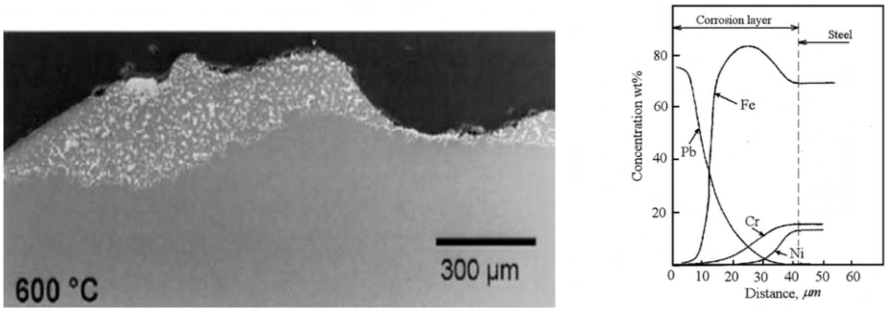

(a) (b)

Figure A.7: Corrosion of an austenitic stainless steel by liquid lead exposure. Reduction in Ni content promote a ferritization(a) from[63], (b) from [64]

The corrosion-inhibitors and the surface protective coatings can decrease the corrosion rate through the formation of stable layers on the metal surface.

-**Oxygen control**: The most important non-metallic corrosion inhibitor is oxygen: controlling the amount of oxygen in the liquid, the formation of an oxide passivating layer on the steel surface is enhanced. From thermodynamic considerations, the oxygen reacts preferentially with Cr and Fe than Pb and Bi, creating a stable and protective layer made or Cr_2O_3 and Fe_3O_4. In general, higher the content of Cr, Al, Si, thinner and more stable is the oxide layer. The oxygen concentration control is complex, since if is too low, an oxide layer cannot be formed and if it is too high the thicker oxide layer loses mechanical stability and resistance; cracks can provide a diffusion path for liquid lead or LBE. Moreover, a too-high O_2 concentration can make energetically possible the formation of lead oxide (PbO) and its deposition of the structural material, in the form of slugs, decreasing the thermal conductivity of the system.

The temperature plays a key role: over 823K, most of steels have a too high oxidation rate and the layer becomes unstable, leading to an increased corrosion rate[66].

-**Metallic inhibitors**: the presence of metals such as Ti and Zr in the liquid can promote the formation of intermetallic nitrides and carbides with the minor elements in the structural materials. The inhibition is effective for low-alloy or carbon steels, while for

stainless steels the inhibition efficiency is very low[66].
-**Thin film coatings**: coatings deposited through PVD or magnetron sputtering; they can provide a strong corrosion and wear resistance. Their features are selected by accurately tuning the deposition techniques' parameters. More details in the next section.

A.1.1. Candidate materials and coatings for LFR

Candidate materials for fuel claddings

The selection of materials for LFR is particularly crucial, especially when considering cladding materials that may be exposed to temperatures of up to 480°C in projects like ELSY and ALFRED in presence of fluent liquid Pb. Austenitic stainless steels, such as AISI 304, AISI 316, and 15-15Ti, exhibit notable characteristics including high ductility, relatively strong resistance, and a lack of transition between brittle and ductile behavior. However, they are susceptible to intergranular corrosion, which can be partially mitigated by incorporating elements like Ti and Nb. These materials are also prone to swelling and high-temperature helium embrittlement due to their high nickel content (9-14%). The likelihood of these issues increases with higher carbon content, but decreasing carbon content, as seen in alloys like F304L, leads to a degradation of mechanical properties[59]. Furthermore, the high chromium content (16-18% for AISI F316) in austenitic stainless steels facilitates the formation of a protective passivating layer in the presence of oxygen. While increasing the Ti/C ratio can reduce intergranular corrosion, it significantly diminishes creep resistance.
Ferritic-martensitic steels (such as T91, T92, T122) are under investigation due to their high mechanical strength, low thermal expansion coefficient, elevated thermal conductivity, and low swelling rate. These properties suggest a potential for increased fuel burn-up. Although extensive studies are required to fully understand the behavior of these materials, initial tests indicate good resistance to Heavy Metal Corrosion (HMC) for ferritic-martensitic steels at temperatures below 400°C[30]. Austenitic steels, which already hold qualifications for Gen II and Gen III reactors, are well-explored in terms of reactor behavior. Their versatility allows for the modification of thermo-mechanical characteristics with minimal changes in composition. Notably, they exhibit a saturation in yield strength at increasing fluence, which is a reflection of microstructural defects saturation[67] and AISI 316L appears to be minimally affected by Liquid Metal Embrittlement (LME) in a controlled oxygen environment, as demonstrated in a test conducted by ENEA at 550°C[33].

Candidate coatings

ENEA, in collaboration with the Italian Institute of Technology (IIT), is actively engaged in the development of ceramic oxide anti-corrosion coatings using the pulsed laser deposition (PLD) technique[33]. The investigation into ceramic materials as coatings is motivated by their inherent chemical inertness, low swelling characteristics, and a microstructure that exhibits resilience against high irradiation doses. Desired attributes for these coatings include strong adhesion to substrates, minimal thermal expansion mismatch to accommodate mechanical stresses, and a deposition process conducted at low temperatures to prevent variations in substrate steel properties. The deposition of Al_2O_3 through pulsed laser deposition (PLD) and atomic layer deposition (ALD) methods has proven effective in producing coatings with high adhesive strength, low porosity, and compressive residual stresses. Notably, the application of PLD has resulted in the growth of dense and compact Al_2O_3 coatings on various steels. These coatings exhibit a structure characterized by a homogeneous dispersion of ultra-fine nanocrystalline domains (4-6 nm) within an amorphous alumina matrix [21]. Unique features have been observed in this type of ceramic coatings: an unusual metal-like plastic behavior, high stiffness and hardness (E = 195 ± 9 GPa, $\nu = 0.29 \pm 0.02$, H=10 GPa), excellent resistance to corrosion up to 600°C in stagnant liquid metals and robust adhesion to substrate[33],[8]. Under heavy ion irradiation dose of 150 dpa at 600°C, higher than the dose expected in an ALFRED reactor core after 5 years (i.e., 100 dpa) grain size increased from 6nm to 290nm and crystalline structure underwent a phase change from $\gamma - Al_2O_3$ to $\alpha/\gamma - Al_2O_3$. With increasing dose, Young modulus E increases monotonically, but the material becomes softer; hardness starts to decrease after the onset of crystallization[34]. For what concerns metallic coatings, Fe-Cr-Al and Fe-Al alloys show excellent anti-corrosion performances in oxygen rich liquid lead after 5000h at 500°C. No erosion/corrosion signs have been observed at the surface of Fe-Al coatings. Since their behavior under high irradiation in still not well known, Al as metallic coatings has been proposed for internal structures, steam generator, DHR heat exchanger and primary pumps on AISI 316LN substrate[33].

A | Appendix B

A.1. Frame comparison and Centroids time-behaviour

In this code, I took the data from the frame analysis (centroids positions) and temperature values. The output is the position in time of a selected frames' interval or the overlapping of to different frames.

```
%%% data inizialization %%%
path_root='D:\Dati Labview\';
title='Enter folder name';
found=0;
while ~found
    answer=inputdlg({'name [dd.mm.yy hh.mm]'},title,[1 70]);
    folder_name=answer{1};
    path_name=strcat(path_root, folder_name);
    found=exist(path_name,'dir');
    if ~found
        title=['Folder ', path_name,' not found'];
    end
end
addpath(path_name);


%%% selezione file %%%
lista=dir([path_name,'\dati_from*.dat']);
nomi_files={lista.name};
[indx,tf] = listdlg('PromptString',{'Select a file.'},...
    'SelectionMode','single','ListString',nomi_files);
if ~tf, return, end
nome_file=lista(indx).name;
```

```
l_nome=length(nome_file);
nome_file_T=[nome_file(1:5), 'T_', nome_file(6:l_nome)];
ppp=load(nome_file, '-ascii');
TT=load(nome_file_T, '-ascii');
if ~ppp(1,1:2)==(TT(1:2))'
    disp('intervals not consistent')
    return
end
file_first=ppp(1,1);
file_last=ppp(1,2);
[nr_p,nc_p]=size(ppp);
ppp=ppp(2:nr_p,:);
[nr,nc]=size(TT);
TT=TT(3:nr,:);
dati_ok=0;
while ~dati_ok
    prompt = {['first frame: [',int2str(file_first),' - ', int2str(file_last), ']'],...
               ['last frame: [',int2str(file_first),' - ', int2str(file_last), ']']};
    dlg_title = [int2str(file_first),' - ', int2str(file_last)];
   % def = {int2str(file_first), int2str(file_last) };
    def = {int2str(file_first), int2str(file_last-1)};
    num_lines = 1;
    answer = inputdlg(prompt,dlg_title,num_lines,def);
    inizio= str2double(answer{1});
    fine=str2double(answer{2});
    dati_ok=(inizio >= file_first && inizio <= file_last)...
        && (fine >= file_first && fine <= file_last)...
        && (fine>=inizio);
end

wsize=0;
iii=inizio-file_first;
ii=fix(iii/2)+1;
fff=fine-file_first;
ff=fix(fff/2)+1;
 %fff=(ff*2)-1  fine=file_first+(ff*2)-1
 baricentro_x=zeros(2,4);
 baricentro_y=baricentro_x;
 baricentro_x(1,1:4)=ppp(ii,1:4);
 baricentro_y(1,1:4)=ppp(ii,5:8);
 baricentro_x(2,1:4)=ppp(ff,1:4);
 baricentro_y(2,1:4)=ppp(ff,5:8);

%%%%%%%%%%%%%%%%%%%%%%%%%%%%%%%%%%%%%%%%%%%%
list={'CTE_dots', 'frame_comparison'};

 [index,tf] = listdlg('PromptString',{'Select a function.'},...
                     'SelectionMode','single','ListString',list);
 if ~tf, return, end
 n_file=list(index);
%%CTE_dots%%
if index==1
colori=[0.7 0.3 0; 0.9 0 0.1; 0 0.7 0.3; 0 0.3 0.7];
markk=['o','s','x','+'];
pp=ppp(:,1:8);
[nt,n8]=size(pp);
if n8<8,  n8;   return,    end
[nT,n1]=size(TT);
if n1>1,  n1;   return,  end
%
if ~(nT==nt)
    nT;    nt,
    nt=min(nt,nT);
    nT=nt;
    TT=TT(1:nT);
end
t_in=TT(1);
TT_max=max(TT);
TT_min=min(TT);
unii=ones(nt,1);
T=(TT-t_in.*unii);
T_max=max(T);
interval=ii:ff;
d=ff-ii+1;
```

```
TT=TT(interval);
pp=ppp(interval,1:8);
%pp=ppp(:,1:8);
%
tt=ii:ff;
unii=ones(d,1);
%
ppmm=zeros(4,2,2);
delta=zeros(4,2);
mezzo=delta;
media=mezzo;
figure
hold on
for j=1:4
    j1=j;
    j2=j+4;
    plot(pp(:,j1),pp(:,j2),'Marker',markk(j),'Color',colori(j,:))
    ppmm(j,1,1)=min(pp(:,j1));
    ppmm(j,1,2)=max(pp(:,j1));
    ppmm(j,2,1)=min(pp(:,j2));
    ppmm(j,2,2)=max(pp(:,j2));
    media(j,1)=mean(pp(:,j1));
    media(j,2)=mean(pp(:,j2));
 for jj=1:2
        delta(j,jj)= ppmm(j,jj,2)-ppmm(j,jj,1);
        mezzo(j,jj)=(ppmm(j,jj,2)+ppmm(j,jj,1))/2;
    end
end
interv=[min(ppmm(:,1,1)),max(ppmm(:,1,2)), ...
        min(ppmm(:,2,1)),max(ppmm(:,2,2))];
marg=0.04;
intervv=interv+[marg.*(interv(2)-interv(1)).*[-1 1], ...
                marg.*(interv(4)-interv(3)).*[-1 1]];
rectangle('Position',[intervv(1), intervv(3), intervv(2)-intervv(1), ...
                                              intervv(4)-intervv(3)])
axis equal
set(gca,'Box','on')
```

```
%
%    pp:  x1,x2,x3,x4,  y1,y2,y3,y4
%    ppmm(j,j1,j2):   j=1,2,3,4,    j1=x,y,  j2=min,max
%    media(j,j1):     j=1,2,3,4,    j1=x,y   media aritmentica
%    delta(j,j1):     j=1,2,3,4,    j1=x,y   max-min
%    mezzo(j,j1):     j=1,2,3,4,    j1=x,y   (min+max)/2
%
delta;
mezzo;
media;
%
deltaa=0.25*max(max(delta));
%deltaa=0;
figure
hold on
for j=1:4
    j1=j;
    j2=j+4;
    if j==1
        ref=[media(j,1),  ppmm(j,2,2)];
    elseif j==2
        ref=[ppmm(j,1,1), media(j,2)];
    elseif j==3
        ref=[ppmm(j,1,2), media(j,2)];
    elseif j==4
        ref=[media(j,1),  ppmm(j,2,1)];
    end
    js=[0 -1; 1 0; -1 0; 0 1];
    plot(pp(:,j1)-(ref(1)-js(j,1)*deltaa).*unii, ...
         pp(:,j2)-(ref(2)-js(j,2)*deltaa).*unii, ...
         'Marker',markk(j),'Color',colori(j,:))
end
axis equal
aaa=axis;
aaa=(1+marg).*aaa;
axis(aaa)
axis equal
```

```
set(gca,'Box','on')
aaa=axis;
plot([aaa(1) 0 aaa(2)],[aaa(3) 0 aaa(4)],'-k', ...
     [aaa(1) 0 aaa(2)],[aaa(4) 0 aaa(3)],'-k')
%
shift=10;
wwsize=floor(wsize);
if wwsize>0
    b = (1/wwsize)*ones(1,wwsize);
    a = 1;
end
figure
hold on
for j=1:4
    jjj=[j,j+4];
    for jj=1:2
        jjs=-(2*jj-3);   % [1,2]-->[1,-1]
        jjjj=jjj(jj);
        ppq=pp(1:d,jjjj)-(pp(1,jjjj)+jjs.*shift).*unii;
        if wwsize>0
            ppqq=filter(b,a,ppq);
        else
            ppqq=ppq;
        end
        plot(tt,ppqq,'-','Color',colori(j,:))
        plot(tt(d),ppqq(d),'Marker',markk(j),'Color',colori(j,:))
    end
end
aaa=axis;
%T=(TT-TT(1).*unii);
T=(TT-t_in.*unii);
% plot(tt,T.*(aaa(4)/max(T)),'-k')
plot(tt,T.*(aaa(4)/T_max),'-k')
text(aaa(1)+0.08*(aaa(2)-aaa(1)),-0.5,['T_m_i_n = ',num2str(TT_min)], ...
      'HorizontalAlignment','left', 'VerticalAlignment','top')
text(aaa(1)+0.45*(aaa(2)-aaa(1)),-0.5,['T_m_a_x = ',num2str(TT_max)], ...
      'HorizontalAlignment','left', 'VerticalAlignment','top')
```

```
text(aaa(1)+0.03*(aaa(2)-aaa(1)),0.4*shift,'x', ...
      'HorizontalAlignment','left', 'VerticalAlignment','bottom')
text(aaa(1)+0.03*(aaa(2)-aaa(1)),-0.4*shift,'y', ...
      'HorizontalAlignment','left', 'VerticalAlignment','top')
set(gca,'Box','on')
     %%%

%frame_comparison%

elseif index==2

    %%%%%%%[i,f]=frame(f1,f2), con f1 e f2 i due valori in
    %%%%%%% ascissa nel grafico (T,ppp) vs time%%%%%%%%%
    file_name_1= strcat('frame_', num2str(inizio) , '.txt');
 fr(:,:,1) = load(file_name_1);
 file_name_2= strcat('frame_', num2str(fine) , '.txt');
 fr(:,:,2) = load(file_name_2);
pixel_max=255;
perc=0.6;
t= perc*pixel_max;       %%threshold
D(:,:,1) = fr(:,:,1)>=t;
D(:,:,2) = fr(:,:,2)>=t;  %% filter images
figure
imshow( D(:,:,1))
[h1,f1]=contourf(D(:,:,1),'LineColor','none');   %draw contour
hold on
[h2,f2]=contour(D(:,:,2),'k--');
baricentro_x
baricentro_y
plot(baricentro_x(1,:),baricentro_y(1,:),'ok')
plot(baricentro_x(2,:),baricentro_y(2,:),'xr')
axis equal
end
```

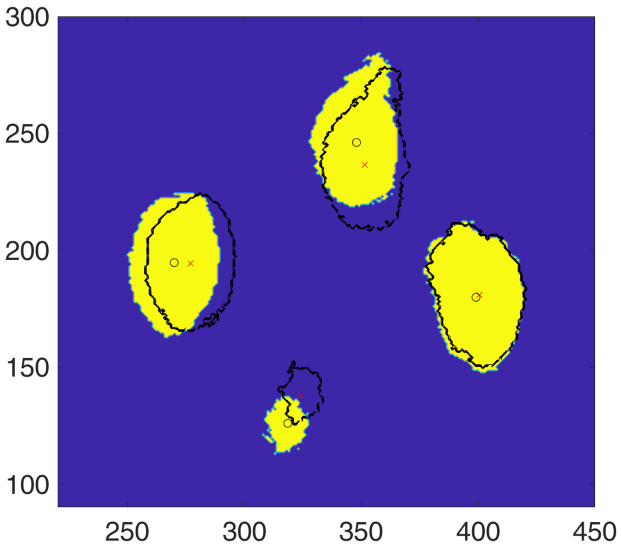

Figure A.1: Output of the code: Position of the spots and the centriods (× and ∘) of two frames recorded at different temperatures. The yellow areas are their initial positions, the black curves represents the final positions. The values on the x and y axis are the pixel

A.2. Residual Stresses determination

This code facilitated the measurement of residual stresses by capturing frames of non-heated samples on both sides for an adequate duration, ensuring a statistically reliable value for spot positions. The variance between the average spot distances on sides A and B provides the curvature. Utilizing the Stoney equation, we can compute the residual stress within the film.

```
path_root='D:\Dati Labview\';
title='Enter folder name';
found=0;
  while ~found
  answer=inputdlg({'name_side_A','name_side_B'},title,[1 70]);
folder_name_A=answer{1}  ;
folder_name_B=answer{2}  ;  %!!
path_name_A=strcat(path_root, folder_name_A);
path_name_B=strcat(path_root, folder_name_B);
found=exist(path_name_A,'dir')||exist(path_name_B,'dir') ;
 if ~found
 title=['Folder ', path_name_A,path_name_B,' not found'];
 end
    end
```

```
addpath(path_name_A);    %!!
addpath(path_name_B);
      % selezione file lato A (film!!)%
listaA=dir([path_name_A,'\dati_from*.dat']);
nomi_files_A={listaA.name};
[indxA,tfA] = listdlg('PromptString',{'Select a file for side A.'},...
    'SelectionMode','single','ListString',nomi_files_A);
if ~tfA, return, end
nome_file_A=listaA(indxA).name;
l_nome_A=length(nome_file_A);
aa=load(nome_file_A, '-ascii');
file_first_A=aa(1,1);
file_last_A=aa(1,2);
[nr_a,nc_a]=size(aa);
aa=aa(2:nr_a,:);

     % selezione file_lato_B %
listaB=dir([path_name_B,'\dati_from*.dat']);
nomi_files_B={listaB.name};
[indxB,tfB] = listdlg('PromptString',{'Select a file for side B.'},...
    'SelectionMode','single','ListString',nomi_files_B);
if ~tfB, return, end
nome_file_B=listaB(indxB).name;
l_nome_B=length(nome_file_B);
bb=load(nome_file_B, '-ascii');
file_first_B=bb(1,1);
file_last_B=bb(1,2);
[nr_b,nc_b]=size(bb);
bb=bb(2:nr_b,:);
  % costruisco una matrice B-A %
aaa=aa(:,1:8);
bbb=bb(:,1:8);
if nr_a>nr_b
    aaa=aaa(1:(nr_b-1),:);
elseif nr_a<=nr_b
    bbb=bbb(1:(nr_a-1),:);
end
```

```
%Define variables x,y for 4 spots
  %% side_a %%
spot1xa=aaa(:, 1);
spot2xa=aaa(:, 2);
spot3xa=aaa(:, 3);
spot4xa=aaa(:, 4);
spot1ya=aaa(:, 5);
spot2ya=aaa(:, 6);
spot3ya=aaa(:, 7);
spot4ya=aaa(:, 8);
diag1a_px=sqrt((spot1xa-spot4xa).^2+(spot1ya-spot4ya).^2);
diag2a_px=sqrt((spot2xa-spot3xa).^2+(spot2ya-spot3ya).^2);
px_to_cm=0.00052*2;
diag1a_cm=diag1a_px*px_to_cm;
diag2a_cm=diag2a_px*px_to_cm;
mean_diag_a=(diag1a_cm+diag2a_cm)/2;
diag_matrix_a=[diag1a_cm diag2a_cm mean_diag_a];
dlmwrite('diagfileA.txt',diag_matrix_a,'-append', 'delimiter','\t','precision',7);

  %% side_b %%
spot1xb=bbb(:, 1);
spot2xb=bbb(:, 2);
spot3xb=bbb(:, 3);
spot4xb=bbb(:, 4);
spot1yb=bbb(:, 5);
spot2yb=bbb(:, 6);
spot3yb=bbb(:, 7);
spot4yb=bbb(:, 8);
diag1b_px=sqrt((spot1xb-spot4xb).^2+(spot1yb-spot4yb).^2);
diag2b_px=sqrt((spot2xb-spot3xb).^2+(spot2yb-spot3yb).^2);
diag1b_cm=diag1b_px*px_to_cm;
diag2b_cm=diag2b_px*px_to_cm;
mean_diag_b=(diag1b_cm+diag2b_cm)/2;
diag_matrix_b=[diag1b_cm diag2b_cm mean_diag_b];
dlmwrite('diagfileB.txt',diag_matrix_b,'-append', 'delimiter','\t','precision',7);
```

```
  % calcolo sforzi %
diff=diag_matrix_a-diag_matrix_b;
kk=(mean(diff,1));
k=kk(3);        %mean of mean diags
m=kk(2);        %mean of diags 2
n=2*kk(1);       %mean of diags 1
if k>0
    disp('compressive residual stress')
else
    disp('tensile residual stress')
end
prompt = {'spessore film(um): ', 'modulo di Young film (GPa): ',...
'coeff. Poisson film (-): '};
dlg_title = 'parametri';
def = {'0.2', '340', '0.31'};
num_lines = 1;
answer = inputdlg(prompt,dlg_title,num_lines,def);
%calculation of 1/radius of curvature
Do= 1;                                         %in cm
theta= 60;
%L=47;
A=58.4;                                        %arm length cm
K=6.2;                                         %distance lens-sensor in cm
L=A-K;                                         %distance sample-lens in cm
F=7.5;                                         %length focal lens in cm
M=L*(1-K/F)+K;                                 %cm
Es=180;                                        %Youngs modulus in GPa
vs=0.23;                                       %Poissons ratio of substrate
ts=0.038;                                      %in cm
tf=str2double(answer{1})*10^-4;                %in cm
CTE_s=2.6e-06;
vf=str2double(answer{3});                      %Poissons ratio of film
Ef=str2double(answer{2});                      %Youngs modulus in GPa
mean_curv = k/(8*Do*M);       %%cm-1
fprintf('the mean curvature is %f m^-1      ', mean_curv*10^2)
sigma_mean=-Es*ts^2*mean_curv/(1-vs)/tf/6;
fprintf('the mean stress is %f GPa     ' , sigma_mean)
```

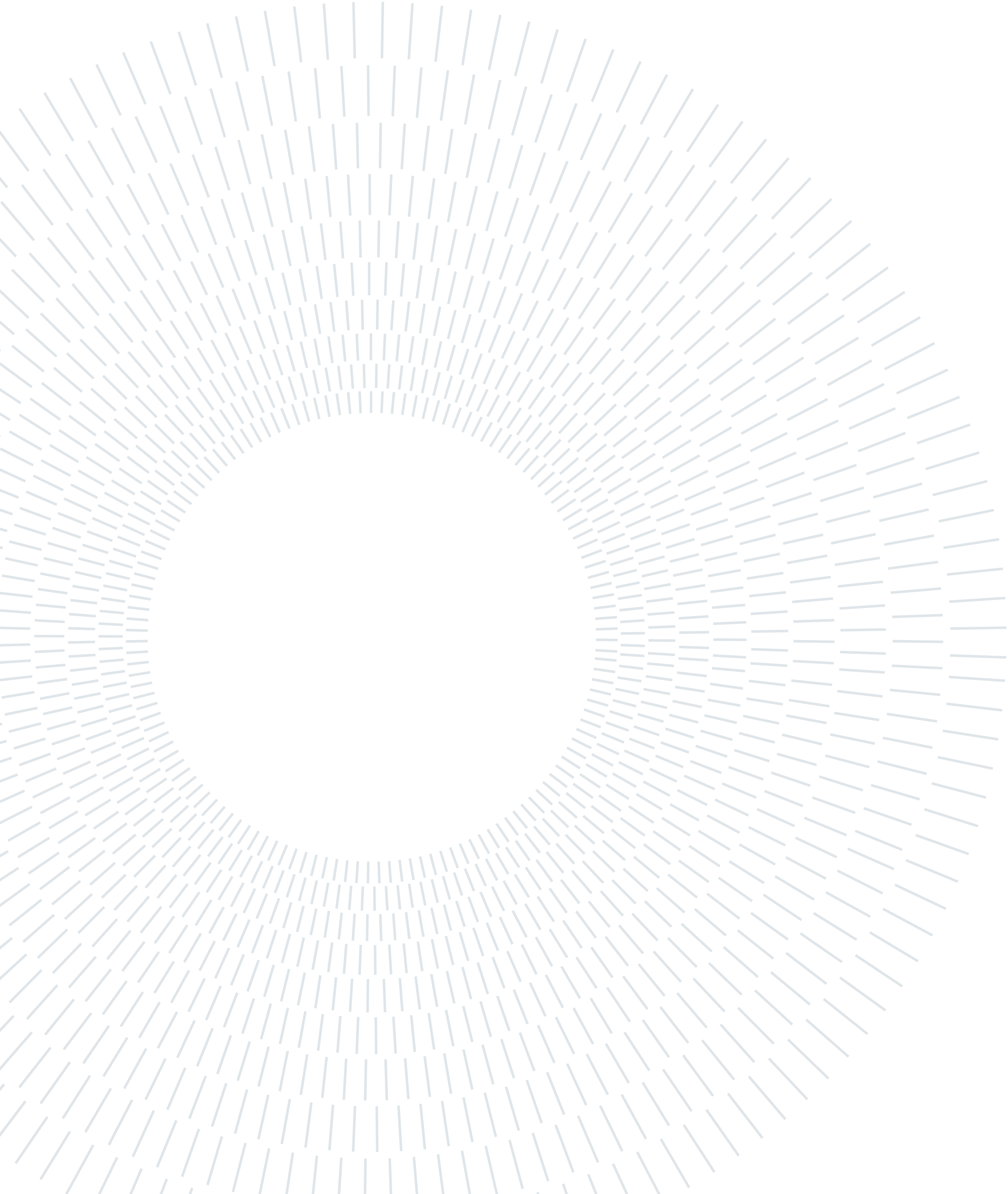

Bibliography

[1] J. E. Greene. Review article: Tracing the recorded history of thin-film sputter deposition: From the 1800s to 2017. *Journal of Vacuum Science and Technology A: Vacuum, Surfaces, and Films, 35(5), 05C204*, 2017.

[2] B. Rogers, J. Adams, and S. Pennathur. Nanotechnology: Understanding small systems, third edition (3rd ed.). *CRC Press.*, 2015.

[3] M.C. Rao and M.S. Shekhawat. A brief survey on basic properties of thin films for device application. *World Scientific*, 2013.

[4] NREL. Best research-cell efficiency chart.

[5] IEA. Electricity market report 2023.

[6] Xin-Jian Xiao and Ke-Jun Jiang. China's nuclear power under the global 1.5 °c target: Preliminary feasibility study and prospects. *Advances in Climate Change Research*, 9(2):138–143, 2018. Including special topic on mitigation for 1.5 °C: Scenarios and options.

[7] E. Besozzi. *Doctoral dissertation, Thermomechanical Characterization of fusion-relevant nanostructured coatings.* PhD thesis, Department of Energy , Politecnico di Milano, 2018.

[8] Francisco García Ferré, Emanuele Bertarelli, Angelica Chiodoni, Davide Carnelli, Dario Gastaldi, Pasquale Vena, Marco G. Beghi, and Fabio Di Fonzo. The mechanical properties of a nanocrystalline $Al_2O_3/a - Al_2O_3$ composite coating measured by nanoindentation and brillouin spectroscopy. *Acta Materialia*, 61(7):2662–2670, 2013.

[9] William D. Nix. Mechanical properties of thin films, 1 2005. Department of Materials Science and Engineering Stanford University.

[10] William D. Nix. Mechanical properties of thin films. *Metallurgical Transactions A*, 20(11):2217–2245, 1989.

[11] Donald M. Mattox. Chapter 4 - physical sputtering and sputter deposition. In

Donald M. Mattox, editor, *The Foundations of Vacuum Coating Technology (Second Edition)*, pages 87–149. William Andrew Publishing, second edition edition, 2018.

[12] D. Vavassori, F. Mirani, F. Gatti, D. Dellasega, and M. Passoni. Role of magnetic field and bias configuration on hipims deposition of w films. *Surface and Coatings Technology*, 458:129343, 2023.

[13] Pantelis Sophoclis Alexopoulos and T. O'sullivan. Mechanical properties of thin films. *Annual Review of Materials Science*, 20:391–420, 1990.

[14] S.Routand, N.Popovici, S.Dalui, M.L. Paramês, R.C.da Silva, A.J. Silvestre, and O. Conde. Phase growth control in low temperature PLD Co: TiO_2 films by pressure. *Current Applied Physics*, 13(2):670–676, 2013.

[15] Guozhong Cao. *Nanostructures and Nanomaterials: Synthesis, Properties And Applications*. World Scientific, 2004.

[16] André Anders. A structure zone diagram including plasma-based deposition and ion etching. *Thin Solid Films*, 518:4087–4090, 05 2010.

[17] H.J. Frost. Microstructural evolution in thin films. *Materials Characterization*, 32(4):257–273, 1994. Computer Modeling and Microstructures.

[18] Carl V. Thompson and Roland Carel. Stress and grain growth in thin films. *Journal of The Mechanics and Physics of Solids*, 44:657–673, 1996.

[19] Milton Ohring. Why are thin films different from the bulk? In Harold E. Bennett, Lloyd L. Chase, Arthur H. Guenther, Brian Emerson Newnam, and M. J. Soileau, editors, *Laser-Induced Damage in Optical Materials: 1993*, volume 2114, pages 624 – 639. International Society for Optics and Photonics, SPIE, 1994.

[20] Paul A. Flinn. Principles and applications of wafer curvature techniques for stress measurements in thin films. *MRS Online Proceedings Library*, 130(1):41–51, 1988.

[21] John A. Thornton and D.W. Hoffman. Stress-related effects in thin films. *Thin Solid Films*, 171(1):5–31, 1989.

[22] Ramnath Venkatraman and John C. Bravman. Separation of film thickness and grain boundary strengthening effects in al thin films on si. *Journal of Materials Research*, 7(8):2040–2048, 1992.

[23] M.S. Jackson and Li Che-yu. Stress relaxation and hillock growth in thin films. *Acta Metallurgica*, 30(11):1993–2000, 1982.

[24] Ramnath Venkatraman and John C. Bravman. Separation of film thickness and grain boundary strengthening effects in al thin films on si. *Journal of Materials Research*, 7(8):2040–2048, 1992.

[25] World-nuclear.org. Generation IV Nuclear Reactors.

[26] Bin Liu, Jinsheng Han, Fang Liu, Jie Sheng, and Zhihao Li. Minor actinide transmutation in the lead-cooled fast reactor. *Progress in Nuclear Energy*, 119:103148, 2020.

[27] Westinghouse Lead Fast Reactor. `https://www.westinghousenuclear.com`, 2019.

[28] Alemberti A. Advanced Lead Fast Reactor European Demonstrator – ALFRED PROJECT.

[29] C. Smith. Lead-Cooled Fast Reactor (LFR) Design: Safety, Neutronics, Thermal Hydraulics, Structural Mechanics, Fuel, Core, and Plant Design. Technical Report LLNL-BOOK–424323, Springer, Germany, Feb 2010.

[30] Luigi Debarberis. On going issues on structural materials of lfr materials of lfr.

[31] Luigi Lepore, Romolo Remetti, and Mauro Cappelli. On Capabilities and Limitations of Current Fast Neutron Flux Monitoring Instrumentation for the Demo LFR ALFRED. *Journal of Nuclear Engineering and Radiation Science*, 2(4):041002, 10 2016.

[32] S.J. Zinkle and Joseth Steven. *Radiation-Induced Effects on Microstructure*, pages 65–98. 02 2012.

[33] Overview on lead-cooled fast reactor design and related technologies development in enea. *Energies*, 14:5157, 08 2021.

[34] F. García Ferré, A. Mairov, L. Ceseracciu, Y. Serruys, P. Trocellier, C. Baumier, O. Kaïtasov, R. Brescia, D. Gastaldi, P. Vena, MG. Beghi, L. Beck, K. Sridharan, and F. Di Fonzo. Radiation endurance in Al_2O_3 nanoceramics, 2016.

[35] `https://www.iter.org`.

[36] Dubus and Gregory. *From Plain Visualisation to Vibration Sensing: Using a Camera to Control the Flexibilities in the ITER Remote Handling Equipment (Doctoral Dissertation)*. PhD thesis, 10 2014.

[37] M. Kikuchi, A. Fasoli, T. Takizuka, Patrick Diamond, Sergei Medvedev, Xutong Duan, H. Zushi, Masaru Furukawa, Yasuaki Kishimoto, Wu Y., O. Sauter, Laurent Villard, Stephan Brunner, Grado Merlo, J.M. Kwon, G. Zheng, Kishore Mishra,

M. Honda, Hanae Urano, and F. Sano. Negative triangularity tokamak as fusion energy system. 03 2014.

[38] Takeshi Hirai, F. Escourbiac, S Carpentier-Chouchana, A Durocher, A Fedosov, Laurent Ferrand, Tommi Jokinen, V Komarov, M Merola, Raphaël Mitteau, R Pitts, W. Shu, M. Sugihara, Vladimir Barabash, Vladimir Kuznetcov, Bruno Riccardi, and Shinji Suzuki. Iter full tungsten divertor qualification program and progress. *Physica Scripta*, 2014:014006, 04 2014.

[39] H Bolt, Vladimir Barabash, Gianfranco Federici, Jochen Linke, Alberto Loarte, J Roth, and K Sato. Plasma facing and high heat flux materials - needs for iter and beyond. *Journal of Nuclear Materials*, 307-311:43–52, 12 2002.

[40] Fei Zhu, Zheng Xie, and Zhengjun Zhang. Phase control and Young's modulus of tungsten thin film prepared by dual ion beam sputtering deposition. *AIP Advances*, 8:035321, 03 2018.

[41] E. Besozzi, A. Maffini, D. Dellasega, V. Russo, A. Facibeni, A. Pazzaglia, M.G. Beghi, and M. Passoni. Nanosecond laser pulses for mimicking thermal effects on nanostructured tungsten-based materials. *Nuclear Fusion*, 58(3):036019, feb 2018.

[42] M. Komm et al. Divertor impurity seeding experiments at the compass tokamak. *Nuclear Fusion*, 59(10):106035, sep 2019.

[43] Karl W. Böer and Udo W. Pohl. *Elasticity and Phonons*, pages 1–34. Springer International Publishing, Cham, 2017.

[44] E. Besozzi. Caratterizzazione di film di tungsteno mediante spettroscopia brillouin. Master's thesis, Politecnico di Milano, Corso di Laurea Magistrale in Ingegneria Nucleare, 2012.

[45] Simon Jones. Ground vibration from underground railways: how simplifying assumptions limit prediction accuracy. 11 2010.

[46] Fariborz Kargar and Alexander A. Balandin. Advances in brillouin–mandelstam light-scattering spectroscopy. *Nature Photonics*, 15(10):720–731, 2021.

[47] Marco G. Beghi, Arthur G. Every, Vitali B. Prakapenka, , and Pavel V. Zinin. *Measurement of the Elastic Properties of Solids by Brillouin Spectroscopy*. CRC Press, 2013.

[48] J. R. Sandercock. *Trends in brillouin scattering: Studies of opaque materials, sup-*

ported films, and central modes, pages 173–206. Springer Berlin Heidelberg, Berlin, Heidelberg, 1982.

[49] E. Besozzi, D. Dellasega, A. Pezzoli, A. Mantegazza, M. Passoni, and M.G. Beghi. Coefficient of thermal expansion of nanostructured tungsten based coatings assessed by substrate curvature method. *Materials & Design*, 137:192–203, 2018.

[50] H. J. Frost. Deformation mechanisms in thin films. *MRS Online Proceedings Library*, 265(1):3–14, 1992.

[51] Chung-Ping Chang, Pi-Cheng Tung, Lih-Horng Shyu, yung-cheng Wang, and Eberhard Manske. Fabry perot displacement interferometer for the measuring range up to 100 mm. *Measurement*, 46:4094–4099, 12 2013.

[52] Nur Ismail, Cristine Calil Kores, Dimitri Geskus, and Markus Pollnau. Fabry-perot resonator: spectral line shapes, generic and related airy distributions, linewidths, finesses, and performance at low or frequency-dependent reflectivity. *Opt. Express*, 24(15):16366–16389, Jul 2016.

[53] Vishakha Nagarajan. Optimization of the Experimental setup for Substrate Curvature Method. Master's thesis, Politecnico di Milano, Milan, 12 2021.

[54] `https://cdn.rohde-schwarz.com/hameg-archive/HM7044_D_E_F_S.pdf`.

[55] O Kraft and W D Nix. Measurement of the lattice thermal expansion coefficients of thin metal films on substrates. *Journal of Applied Physics*, 83(6), 3 1998.

[56] D. Kim, W.D. Nix, Eduard Arzt, Michael Deal, and Jim Plummer. Diffusional hillock formation in al thin films controlled by creep. *MRS Proceedings*, 594, 01 2011.

[57] E. Besozzi, D. Dellasega, A. Pezzoli, C. Conti, M. Passoni, and M.G. Beghi. Amorphous, ultra-nano- and nano-crystalline tungsten-based coatings grown by pulsed laser deposition: mechanical characterization by surface brillouin spectroscopy. *Materials and Design*, 106:14–21, 2016.

[58] Giacomo Leonardis. Preliminary investigation of thermo-mechanical properties of novel ytrria-doped alumina coatings for Lead Fast Reactor applications. Master's thesis, Politecnico di Milano, Milan, 7 2023.

[59] L.M. Cumo. *Nuclear Plants*. Sapienza Università Editrice, 2 edition, 2017.

[60] C.R.F. Azevedo. A review on neutron-irradiation-induced hardening of metallic components. *Engineering Failure Analysis*, 18(8):1921–1942, 2011.

[61] L.L Snead, S.J Zinkle, J.C Hay, and M.C Osborne. Amorphization of SiC under ion and neutron irradiation. *Nuclear Instruments and Methods in Physics Research Section B: Beam Interactions with Materials and Atoms*, 141(1):123–132, 1998.

[62] R.S. Wilks, J.A. Desport, and J.A.G. Smith. The irradiation-induced macroscopic growth of $\alpha - Al_2O_3$ single crystals. *Journal of Nuclear Materials*, 24(1):80–86, 1967.

[63] M.H. Kamdar. Fracture in liquid metal environments, Technical Report ARLCB-TR-85013. *US ARMY Armament R&D Center*, 1985.

[64] R. M. Bruscato. Liquid metal embrittlement of austenitic stainless steel when welded to galvanized steel. *Welding Journal*, 71, 1992.

[65] Li Ning. Active control of oxygen in molten lead–bismuth eutectic systems to prevent steel corrosion and coolant contamination. *Journal of Nuclear Materials*, 300(1):73–81, 2002.

[66] Jinsuo Zhang. A review of steel corrosion by liquid lead and lead–bismuth. *Corrosion Science*, 51(6):1207–1227, 2009.

[67] F.A. Garner, M.L. Hamilton, N.F. Panayotou, and G.D. Johnson. The microstructural origins of yield strength changes in aisi 316 during fission or fusion irradiation. *Journal of Nuclear Materials*, 104:803–807, 1981.

List of Figures

1 From the left: copper interconnect metallization in a transistor (SEM view after etching) , architectural glass coatings, coated cutting tools[1] 2
2 Examples of PV application of thin films (a) and world production of different types of PV (b). Fig.taken from [2] 3
3 World energy consumption trend, Fig.taken from [5] 4

1.1 On the left: biaxial stress induces a bending moment in the substrate; on the right: variation of biaxial stresses in the y-directions[9] 6
1.2 Relation between axial stress in a thin film and the associated substrate bending. Figure from [10] 6
1.3 Forces acting on the film and substrate. Fig. from [10] 7
1.4 Curvature geometryFig. from [10] 8
1.5 Structure Zone Diagram. The evolution of film's structure as a function of the generalized T(i.e., the homologous T, T_m, plus a characteristic temperature of a heated region affecting the rearrangement of N moved atoms) and normalized energy E of the impinging particles. Fig.from [16] 12
1.6 Interaction between working gas atoms and growing film. Fig.from[11] . . . 15

2.1 Westinghouse LFR [27] 20
2.2 (a)Neutron energy spectrum in an ALFRED type LFR. Two peaks, the first linked to the thermal and the second to the fast neutrons can be observed[29], (b)Temperature and effects at which different component of a ELSY LFR are subjected to[30]. 21
2.3 Fusion reaction between D and T[7] 23
2.4 Tokamak reactor[36] 23
2.5 (a)Divertor position and magnatic fiel lines in a section of the toroid[37] , (b)Divertor's components[38] 24
2.6 Atomistic effects in presence of high-energy particles.[7] 25
2.7 Crystalline and amorphous W after different laser-simulated thermal loads. Figure from [41] 28

3.1 Elasto-plastic deformation associated to indentation(a), Loading-Unloading curve in nanoindentation(b)[10] 30
3.2 Reference geometry for surface dynamic problem. Fig.from[44] 34
3.3 Acoustic Waves in solids: Longitudinal and transverse bulk waves(a), Rayleigh waves(b)[45] 35
3.4 Dispersion relation of a W thin film on a Si substrate. In absissa, the product of the surface wavenumber $k_{//}$ and film thickness h; in ordinates, the velocities associated to Rayleigh and Sezawa modes. Figure from [44] . 37
3.5 Interaction and momentum conservation in the laser light-phonon interaction. Figure from [46] 38
3.6 (b)Typical frequency's range for Raman, BLS and LWNR techniques. (c)Dispesion relation for a cubic crystal, showing longitudinal and tranverse modes in acoustic (blue) and optic (red) branches. (d) typical Raman (optical phonons, high frequency) and BLS (acoustic phonons, low frequency) spectra. Figures from [46] 39
3.7 Surface ripple mechanism. Figures from [46] 40
3.8 A typical Brillouin spectrum, showing peaks for different SAW's modes (Rayleigh and Sezawa). Figure from [44] 41
3.9 Laser Beam Deflection technique. Figure (b) has been vertically dilated; the ortoghonal segments (at the left) are two unitary segments in the 2 directions. Figure from [49] 42
3.10 Stress-Temperature curve and Deformation Mechanism Map for thin Al on substrate[50] 44
3.11 (a)Stress-temperature plot for an Al film on a Si substrate, (b) stress relaxation due to densification, (c) crystallization and following stress relaxation. Fig. from [10] 45

4.1 Scheme of optical path. Green line represents the principal beam, while red one the auxilary beam[44]. 48
4.2 Fabry-Perot interferometer, Figure from [51] 49
4.3 Airy distribution compared to Lorenzian distribution for different values of R1 and R2, Figure from [52] 50
4.4 LS level curves: the thicker curves indentify regions relative to a 68% and 90% confidence level (black curves)[44] 52
4.5 Experimental apparatus, (b) from [38] 53
4.6 Laser and etalons[53] 53
4.7 Spots on the sensor. Intensity profile can be seen.[53] 54

4.8 Vacuum chamber and optical system[53] 54
4.9 (a)Programmable power supply, (b)Series-modules configuration, from [54] 55
4.10 (a)Parallel beams deflection on a curved sample, (b)optical path seen from the rays point of view [49] 56
4.11 (a)Sensitivity variation with K. The dotted line represent the focus position. A=58cm and F=7.5cm, (b) Relative sensitivity level curves. The white strip represent the "forbidden region": here spots are not resolvable. The optical axis goes from the sample to the sensor, so the distane lens-sensor K is assumed negative. 58
4.12 Oscillation of the distance between two spots. The dotted line represent the distance d, the arrow represent the variance. The term 'diagonal' refers to the distance between spots positioned at opposite edges of the array. . . 59

5.1 Laser's arm with movable components: they allow transverse movements . 62
5.2 Relative sensitivity $\frac{1}{d_\infty}\frac{d(\Delta d)}{d(1/R)}$ 63
5.3 Level curves of spots' displacements on the sensor $d - d_\infty$. 63
5.4 (a)Temperature registered with thermocamera on different points(red line). Points 1-5 refers to the sample's surface, while points 6-9 to the support, as seen in image, as indicated in (b). At steady state, the temperature measured with TCK is lower than that of the pyrometer, since it is positioned right above the alumina plate. White dotted line in (b) shows the position of the alumina plate 64
5.5 Sample magnification with SEM of the as-deposited samples: (a) Al-19-2, (b) Al-26-2, (c)Al-27-2 68
5.6 Sample magnification with SEM: Cross section of(a) Al-19-2, (b) Al-26-2, (c)Al-27-2. Al-26-2 shows the most compact structure, with the lower crystal dimension. 69
5.7 Brillouin frequency spectrum of Al-26 made at different angles. Arrows indicate Rayleigh peaks; Peaks at lower frequencies are spurious, since they don't disperse. 70
5.8 LS level curves. Red curves represent lower values of LS. The straight continue line represent the bulk modulus (K_{bulk}) of bulk Al, while the dotted one the ratio (G/K_{bulk}) 71
5.9 Normalized Stress (red) and Temperature (blue) vs time. A filter has been applied to better visualize the stress behavior. 72
5.10 Linear segment of κ vs T plot of Al-27-2 during cooling. 73

5.11 Stress vs Temperature: the non-linear behaviour is shown. (a)Al-19-2, (b) Al-27-2 74
5.12 (a) and (c): Al-27 as deposited; (b) and (d): Al-27 after heating. Increased hillocks are observable after heating. The cross sections show a severe roughness modification. 75
5.13 W-133(g), W-137(h), W-140(i)[12] 76
5.14 Density and Ar (%at) in each samples (yellow dots represents W-133, 137, and 140)[12] 76
5.15 W-137 LS estimator level curves: As seen for Al, bounds are set for K_{bulk}(continuous blue line) and $(G/K)_{bulk}$(dotted line); black curve is 68% confidence region. Yellow lines represent constant Young moduli. 77
5.16 Stress Temperature Diagram for W133 78
5.17 Stress Temperature Diagram for WFW1004 80
5.18 XRD of amorphous W as a function of the annealing temperature; a peak linked to the (100) crystal develops at temperatures higher than 450°C. Figure from [57] 80
5.19 Measured residual stresses of the as-deposited samples 81
5.20 Brillouin Spectra at different angles for WN-39; we can see both Rayleigh's and Sezawa's modes 82
5.21 Intersection between elastic constants of bulk W and LS level curve corresponding to 68% confidence region. (a)WN-21 and (b) WN-39 83
5.22 Thermal cycles for WN39. Stress relaxation occurs through densification at every cycles, for a combined effect of plastic flow and structural relaxation. 83
5.23 SEM image of annealed WN40 surface.Darker regions on the surface signify areas where the film has undergone delamination. 84

6.1 Young Modulus of W samples (red) and WN samples (black). 88
6.2 (a)CTE values of W samples, the dotted line represent the value of bulk-W CTE. (b)Ratio between CTE_{film} and CTE_{bulk} for W(red), WN(black) and Al(blue) 89

A.1 Several defects induced by irradiation, mainly due to Frenkel pairs formation[60] 92
A.2 Irradiation effects on stress-deformation curve in mild steel(left) and single crystal FCC metal(right)[60] 93
A.3 Linear expansion of different lattice parameters of a FCC metal[62] 94
A.4 Swelling in a FCC metals at different temperatures(a), (b)Voids and bubbles nucleation at GB [32] 95
A.5 Crystallization and grain growth induced by neutron fluence in Al_2O_3 [34] . 96

A.6 Increase of local plasticity and emission of dislocations from crack tip.(a) LME mechanism[63], (b) intragranular LME[64] 97

A.7 Corrosion of an austenitic stainless steel by liquid lead exposure. Reduction in Ni content promote a ferritization(a) from[63], (b) from [64] 98

A.1 Output of the code: Position of the spots and the centriods (× and ∘) of two frames recorded at different temperatures. The yellow areas are their initial positions, the black curves represents the final positions. The values on the x and y axis are the pixel 108

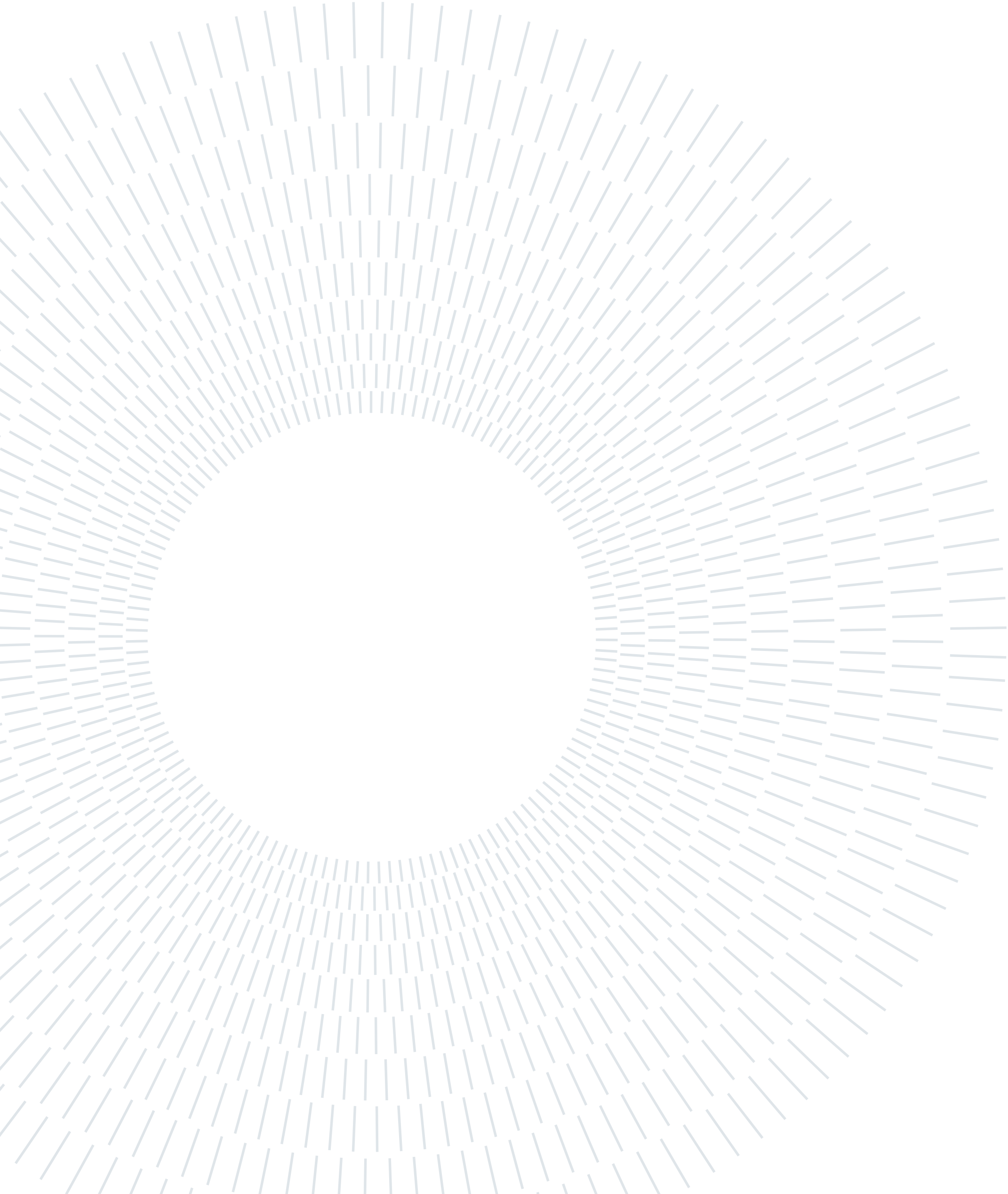

List of Tables

3.1 Bulk properties of Si(s) and W(f). 41

5.1 Samples used in this work: the bold values of densities are those calculated, the others are extrapolated from previous works. **PC**=polycristalline; **NC**=nanocrystalline; **DPCG**=densely packed columnar grains; **A**=amorphous; **UNC**=ultra-nano-crystalline; **HP**=HiPIMS; **PLD**=Pulsed Laser Deposition 67
5.2 Measured and calculated elastic propertis of Al TF 72
5.3 Measured and calculated elastic propertis of Al TF 73
5.4 Measured residual stresses for W samples,(c)stands for *compressive* 77
5.5 Measured and calculated elastic properties of W-137 78
5.6 Measured CTE 79
5.7 Deposition parameters, atomic composiotion and density of WN samples . 81
5.8 Measured and calculated elastic properties of W-137 82
5.9 CTEs of WN samples 84

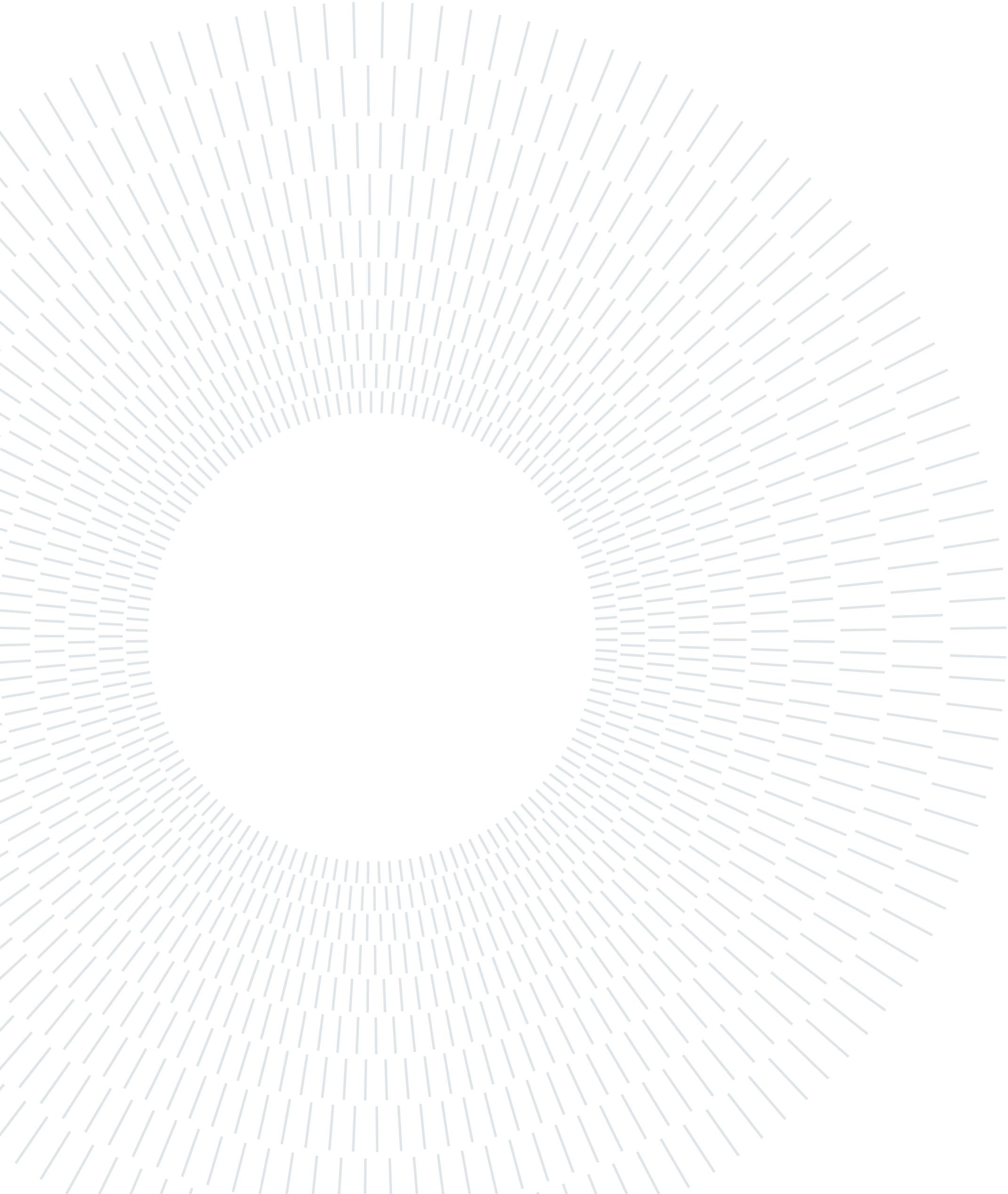

Acknowledgements

I wish to extend my sincere appreciation to Professor Marco Beghi for his invaluable patience and constructive feedback throughout this endeavor. I am also grateful to Luigi Bana and Davide Vavassori for providing the samples and their outstanding assistance in this research.

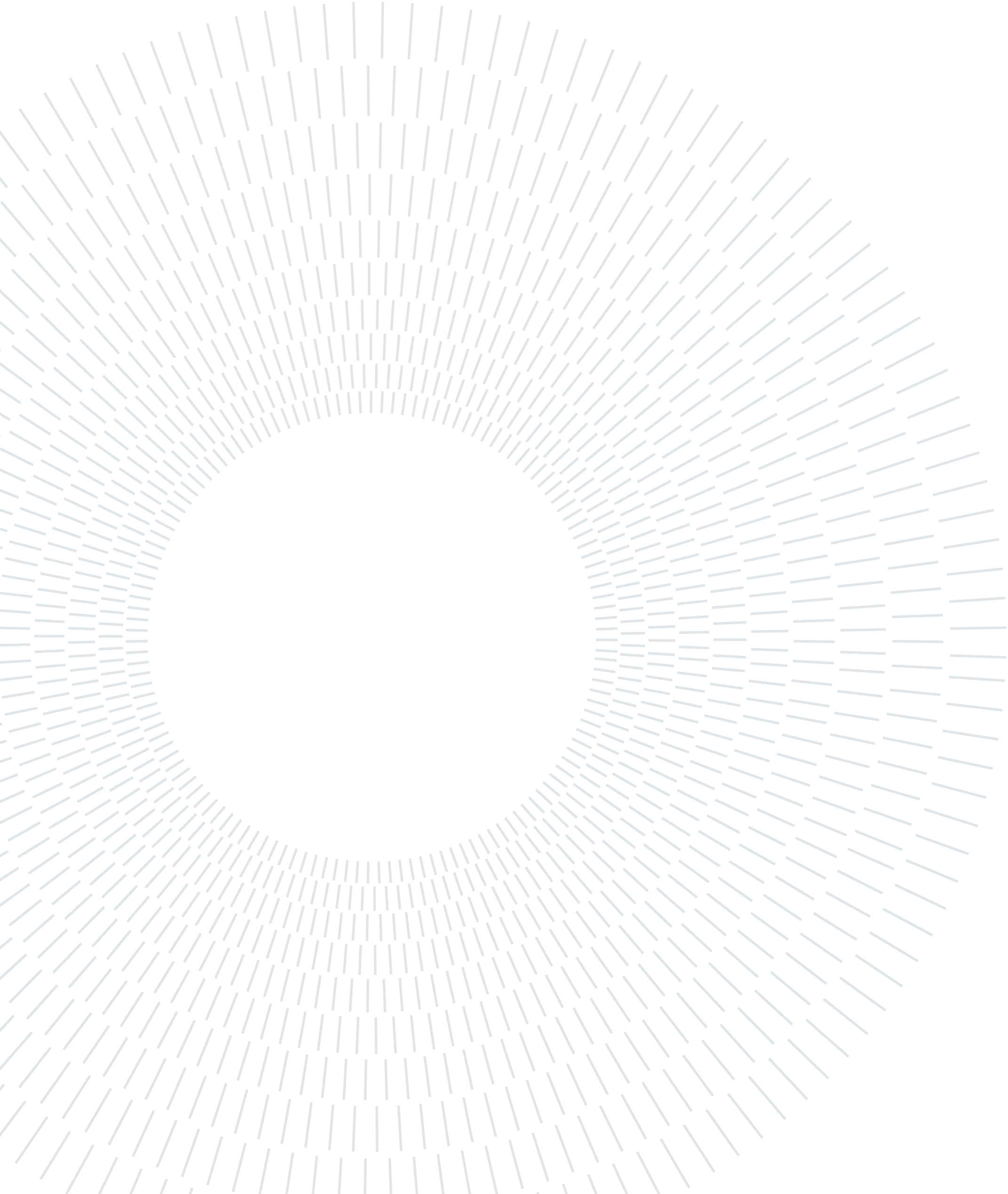A heartfelt thanks goes to my mother, Laura, my father, Mimmo, and my sister, Margherita, for their unwavering support during this long journey.